Transitional phenomena in oil mist filtration

zur Erlangung des akademischen Grades eines
DOKTORS DER INGENIEURWISSENSCHAFTEN
(Dr.-Ing.)

von der KIT-Fakultät für Chemieingenieurwesen und Verfahrenstechnik
des
Karlsruher Instituts für Technologie (KIT)
genehmigte

DISSERTATION

von
Eckhard Kolb
aus Worms

Erstgutachter:	Prof. Dr. Gerhard Kasper
Zweitgutachterin:	Prof. Dr.-Ing. Heike P. Karbstein
Tag der mündlichen Prüfung:	12. November 2021

Acknowledgements

In the course of this thesis project I have received kind support and helpful input from countless people who I happily remember and to whom I would like to express my greatest gratitude. It would be impossible to name all of them here which is why only a few are mentioned below.

First and foremost, I would like to thank my doctoral supervisor, Prof. Dr. Gerhard Kasper, for the company and guidance through the heighs and lows of my studies. Your gentle encouragement, scientific acumen and editorial skills have made a deep impression on my own abilities and ongoing endeavors to expand them further. Thank you.

Furthermore, I would like to thank Prof. Dr.-Ing. Heike P. Karbstein for reviewing this dissertation and serving as second examiner.

Thanks are also due to Dr.-Ing. Jörg Meyer for the many insightful discussions, his sharp-witted analyses and helpful advice.

I would like to thank my students and co-authors Ann-Kathrin Müller, Anne Watzek, Robert Schmitt and Victor Francesconi for our pleasant and fruitful collaborations and their hard work in the lab which contributed significantly to this thesis.

Gratitude is also owed to the staff of the mechanical and electrical workshops, the particle lab and all other technicians at the Institute of Mechanical Process Engineering and Mechanics (MVM) for providing the best possible technical support and the possibility for me to gain more hands-on experience.

The secretaries as well as the administration office at the MVM are thanked for their sympathetic ear and the smooth processing of the bureaucratic burden.

Isabelle de Wolf and her team from Atlas-Copco NV are also gratefully acknowledged for their financial and technical support, the friendly atmosphere during our meetings as well as their great interest in the progress of my research.

My office mates Stefan Wurster, Almuth Schwarz and all other former colleagues and members of the MVM not mentioned here are also thanked for the collaborative and friendly environment.

I would also like to thank Fiona Rudolph-Crowther for proofreading the thesis and improving linguistic subtleties that are beyond the language skills of a non-native speaker.

And finally, I would like to express my deepest thanks to my wife Kristina for maintaining her endless patience and great serenity during the rush hour of our lives.

Table of Contents

1

Abstract

The filtration of oil mists, or air-borne oil droplets, can be found in a variety of technical applications such as the crankcase ventilation of engines, metal cutting and compressed air conditioning. The loading behavior of mist filters differs significantly from more habitual types of filtration, such as solid-liquid separation and dust filtration, in that deposited droplets are moved by the air flow and capillary forces of the filter medium. Therefore, mist filters are a subcategory of coalescence filters which have generally received much less scientific attention than other well-known fields of filtration. And to make matters worse, the few publications in the narrow field of oil mist filtration often seem to contradict each other.

Unlike "classic" and static filters which have to be cleaned or replaced when fully loaded, the deposited droplets in mist filters coalesce with each other and are then moved by the air flow to the filter rear side where they drain in direction dictated by gravity. The on-set of drainage also marks the start of an equilibrium between the oil flow entering and exiting the filter. This so-called *steady state* results in constant values for the drainage rate from the filter, the liquid saturation (or hold-up) of the filter media, and the significantly increased level of pressure drop, Δp. The steady state performance – currently best described in the Film-and-Channel-Model by Kampa et al. (2014) – is therefore of utmost importance for filter evaluation and comparisons between different mist filters.

The *Film-and-Channel-Model* phenomenologically describes the presence of deposited liquid in form of thin films and channel patterns and quantifies their contributions to the steady-state Δp. The "internal" channel pressure drop, $\Delta p_{channel}$, is caused by the transportation and hold-up of oil within the filter medium. The "external" film pressure drop, Δp_{jump}, is, on the other hand, caused by a thin liquid film, either where the oil leaves a wettable or enters a non-wettable filter medium. The findings of Kampa not only revealed the physical mechanisms behind the loading curves of mist filters of different wettabilities but also allowed for the first time to reliably predict the steady-state Δp. As pioneering as the Film-and-Channel-Model might be, it is anything but complete and left open questions which serve as a starting point for the present thesis.

The main goal of this work is to extend the scope of the Film-and-Channel-Model to a broader range of operating conditions and filter media properties, and to incorporate the filter efficiency into the model framework. Therefore, investigations focus not only on findings to validate and enhance this model but also on its physical limits. The current limitations of the Film-and-Channel-Model might be significantly shifted by filter media properties and hitherto unidentified transitional phenomena of pressure drop and efficiency. Published data indicate that such phenomena occur prior to and beyond steady-state operation.

The thesis at hand comprises a critical literature review, a statement of its scope and objectives, followed by five main chapters, summarizing conclusions and an outlook. Four of the main chapters (Chapter 6, 8, 9, and 10) represent independent modules, published as separate units in the relevant literature. Chapter 7 is partially based on a publication but contains also unpublished material. The principal objectives of the main chapters are to investigate:

- the impact of the filter face velocity on $\Delta p_{channel}$ and Δp_{jump},
- the cause of Δp_{jump} and its correlation with the film morphology,
- an extension of the Film-and-Channel-Model towards the efficiency,
- the causes for an increase of Δp beyond the steady state,
- and the accuracy of measuring pore size distributions of mist filter media.

Investigations are mostly of an experimental nature and limited to commonly used glass microfiber filter media (wettable & non-wettable) loaded in stacks of flat sheet layers. The oil dispersed into sub-micron droplets is limited to a single type, representative for the use in oil-flooded screw compressors. Oil loading

rates were varied between 15 and 1100 mg/(m^{2}s); face velocities between 5 and 70 cm/s. The range of these two operating conditions covers the operation of most mist filter applications.

The first main chapter, **Chapter 6**, investigates the dependence of Δp_{jump}, $\Delta p_{channel}$, and the internal saturation on the face velocity and the oil loading rate for a representative wettable filter medium. Within the accuracy of the experiments, Δp_{jump} is found to be independent of either variable. The contribution of deposited liquid to $\Delta p_{channel}$ is evaluated on basis of $\Delta p_{channel} - \Delta p_0$ or the excess channel-Δp, i.e. the increase in Δp over the pressure drop of the dry filter, Δp_0. The excess channel-Δp increases with the oil loading rate but remains largely constant with the face velocity. In other words, a constant mass flow of liquid to be transported always results in the same excess channel-Δp and increases only if more liquid is to be transported. Hence, the excess channel-Δp can be interpreted as the energy required for the internal oil transport.

In order to maintain a constant excess channel-Δp for a given oil loading rate, the saturation in the channel region decreases with the face velocity. Image analyses reveal that the saturation adjusts itself by reducing the oil channel diameter and not via the number of channels per area. This observation is due to the coalescence cascade in the upstream region of the filter. The bulk of oil mist is deposited uniformly in this region, coalesces into larger drops and eventually forms a channel. Neither the capture area to feed a single channel nor possible coalescence among several channels seem to be influenced from variations of the two principal operating conditions.

Also, Chapter 6 introduces the phenomenon of a slow increase in Δp beyond the steady state. This so-called Δp-creep was found to become more pronounced with increasing oil loading rate and filter face velocity. This transitional phenomenon is investigated in detail in Chapter 9.

Chapter 7 demonstrates that Δp_{jump} of wettable filter media must be linked to capillary phenomena and not to the film thickness as recently stated by Chang et al. (2016, 2017). A good approximation for Δp_{jump} is the bubble point which corresponds to the largest pore size of the filter medium and can be derived from capillary flow porometry measurements. Experiments were conducted at variable face velocities between 5 and 70 cm/s with 4 different media grades having largest pore sizes between 28 and 47 µm. Despite considerable scatter in the data, Δp_{jump} remains approximately constant across this wide range of face velocities indicating that the number of largest pores is sufficiently high to cope with most air flows in industrial applications.

In the following **Chapter 8**, the Film-and-Channel-Model is successfully extended towards the filter efficiency. A new approach is presented to break down the overall efficiency of a mist filter into separate contributions of the film, the channel region as well as the coalescence region in the first layer of wettable filters.

All media investigated (2 grades each of non-wettable and wettable media) lose a significant part of their efficiency when saturated with oil. The first layer in a wettable filter has the highest saturation and thus the largest difference between wet and dry efficiencies. The subsequent channel layers within the filter depth have a lower and constant level of saturation and consequently also a higher efficiency. Moreover, the channel efficiency of non-wettable media is considerably higher than in wettable media of about the same grade. For both wettabilities, the film acts as an inertial separator with a 50% cut-off for droplets of about 250 nm. Hence, larger droplets are almost completely removed by the film while smaller droplets do pass without significant hindrance.

The enhanced Film-and-Channel-Model also predicts the fractional efficiency of mist filters with increasing layer numbers. For single-layer filters, the film efficiency governs the overall efficiency while for thicker filters, the film's contribution becomes less significant than the channel efficiency. The newly discovered contribution of the film to the improved efficiency of larger droplets puts the often-emphasized role of the interstitial velocity in perspective and helps to explain seemingly contradictory data in the literature.

Downstream measurements of the total number concentration further reveal that re-entrainment of bursting bubbles from the film gradually gains significance as the number of media layers increases and the filter becomes more efficient. This generation of droplets sets a limit not only to mist filter efficiencies but also to the application of the extended Film-and-Channel-Model in this work.

Chapter 9 critically reviews the concept of steady state(s) for mist filter operation and investigates the (very) slow but steady increase of Δp beyond the common definition of oil mist filter's "steady" state. This creep phenomenon can be found only in initially dry filters. Pre-saturated filters[1] on the other hand reach their steady operation typically relatively rapidly and then maintain a very constant and stable Δp during continued loading, although at a higher level than the initially dry filter.

The creep phenomenon is investigated by comparisons of initially dry (and well-defined) pre-saturated filter media of fine and coarse grades. Experiments

[1]The pre-saturation of mist filters prior to the start of an experiment, e.g. by dipping the filter in oil, is commonly used to accelerate the time-consuming loading with aerosol.

were accelerated by higher oil loading rates and exceed by far the time required to reach the on-set of steady operation. The inital working hypothesis that the creep approaches the higher Δp of pre-saturated filters was proven wrong: The asymptote (or the end point) of the creep always remains below the pre-saturated reference values and has to be considered as a separate steady state. The underlying cause for the creep is a gradual accumulation of very fine droplets of coalesced oil in the depth of the filter between the oil channels. As a result of this continued accumulation, both the saturation level and the interstitial air velocity increase and cause a significant and additional Δp – especially in finer media grades. The higher Δp of pre-saturated filters is, on the other hand, caused by an absence of oil channels and a homogeneous liquid distribution at the same saturation level than the initially dry filters. The difference between pre-saturated and initially dry filters and a very pronounced creep phenomenon in finer media grades help to reconcile apparent contradictions in the relevant literature.

Most oil mist filters in the industry are neither pre-saturated nor subject to a long-term creep during continuous filtration but are started dry and operated discontinuously throughout their complete life. The impact of a more realistic operation on saturation and Δp is therefore also addressed in discontinuous experiments and especially in on-off operation as the most common type of application.

Interruptions of the air flow lead to a capillary redistribution of oil from the channels and a slightly more homogeneous liquid pattern of the same saturation. Resuming operation at previous conditions causes therefore an increase of the steady-state Δp at a higher level. Δp increases only in the first few cycles, becomes eventually constant for continued on-off operation, and remains here below the value of pre-saturated filters.

However, the pre-saturated (and ultimate) state of a mist filter can be achieved in another type of discontinuous operation when the face velocity is temporarily reduced to a lower level. Low face velocities cause a highly saturated filter which when resuming operation at the previous higher velocity, irreversibly loses the oil channel patterns and ends at the same state as its pre-saturated counterpart.

The last of the main chapters, **Chapter 10**, evaluates the accuracy of capillary flow porometry as a key method to characterize pore size distributions of a glass microfiber medium. Low-volatility fluorocarbons, commonly used as a wetting liquid for this method, were found to evaporate quickly during a scan, leading to major distortions of the pore size distribution derived from such a measurement. This behavior becomes visible in an abrupt and characteristic cut-off in the

middle of the pores size distribution. The location of the cut-off is determined by the kinetics of the evaporation and thus totally arbitrary. Obviously, this makes comparisons between different laboratories almost impossible.

A reliable evaluation of pores below the cut-off can be done with less volatile silicone oils. Measurements with this wetting liquid reveal that about 20% of the pore size distribution in the reference medium is smaller than 2 µm corresponding to about 400 mbar in differential pressure. Liquid in these fine pores could not be removed in capillary flow porometry experiments and remains also trapped during filtration experiments. Furthermore, experiments with variable kinematic viscosities (5–100 mm^2/s) of silicone oils did not show a dependence of capillary flow porometry on the viscosity of the wetting liquid as assumed in the literature.

In **summary**, this work validates the Film-and-Channel-Model for variable operating conditions and expands it to include the filter efficiency. Therefore, the current Film-and-Channel-Model allows for the design of mist filters with predetermined values of Δp and efficiency at their corresponding steady state. In the light of this enhanced model, the present thesis re-evaluates well-established yet sometimes contradicting findings of older literature and closes these gaps by revealing unidentified transitional phenomena during mist filter loading.

2

German abstract - Zusammenfassung

Ölnebel, also gasgetragene Öltröpfchen, finden sich in einer Vielzahl von automobilen und industriellen Anwendungen wie zum Beispiel der Entlüftung von Kurbelwellengehäusen, zerspanenden Bearbeitungszentren oder der Druckluftaufbereitung. Die Filtration von Ölnebel unterscheidet sich grundlegend von weit bekannteren Filtrationsarten wie beispielsweise der Staubfiltration oder der Fest-Flüssig-Trennung. Ölnebelfilter zählen daher zu einer Unterkategorie der Koaleszenzfilter, deren Wirkungsweise im Allgemeinen weit weniger von der Fachliteratur beleuchtet wird, als dies bei den populäreren Filtrationsarten der Fall ist.

Im Wesentlichen unterscheiden sich Ölnebelfilter von den klassischen Filtrationsarten darin, dass abgeschiedene Öltröpfchen nicht am Ort der Abscheidung verbleiben, sondern miteinander koaleszieren, durch Luftströmung und Kapillarkräfte im Filter verteilt werden und letztendlich den Filter als Drainage auf der Rückseite verlassen. Bei kontinuierlicher und konstanter Filtration wird das Einsetzen der Drainage auch als der Beginn des stationären Zustandes bezeichnet. Werden Filter darüberhinaus weiterbetrieben, bleiben Betriebsparameter wie die Drainagerate, die Ölsättigung des Filters, der Druckverlust sowie die Effizienz konstant. Dementsprechend spielt der stationäre Zustand eine herausragende Rolle für die Bewertung des Betriebsverhaltens von Ölnebelfiltern. Ein bedeutender und richtungsweisender Beitrag zum besseren Verständnis der

physikalischen Vorgänge in stationär betriebenen Ölnebelfiltern ist das Kanal-Film-Modell von Kampa (2015). Dieses Modell stellt auch den Ausgangspunkt der vorliegenden Arbeit dar.

Das *Kanal-Film-Modell* beschreibt die Auswirkung des abgeschiedenen Öls auf den Filterdruckverlust, Δp, im stationären Betriebszustand. Dieser setzt sich dabei aus einem Kanaldruckverlust, $\Delta p_{channel}$, und Filmdruckverlust, Δp_{jump}, zusammen. $\Delta p_{channel}$ hat seinen Ursprung im Filterinneren und lässt sich kanalartigen Ölstrukturen zuordnen, welche von der Luftströmung durch den Filter geleitet werden. Δp_{jump} kommt dadurch zustande, dass die zu filternde Luft einen dünnen Ölfilm durch kleinste Poren im Filtermedium passieren muss. Der Ort der Filmbildung hängt von der Benetzbarkeit der verwendeten Medien mit Öl ab: bei Benetzbaren auf der Filterrückseite und bei Nichtbenetzbaren auf der Vorderseite. Die Erkenntnisse von Kampa zeigten erstmals die grundlegenden Mechanismen hinter den lange bekannten Beladungskurven von Ölnebelfiltern unterschiedlicher Benetzbarkeit auf. Darüberhinaus kann das Kanal-Film-Modell auch zur Vorhersage des stationären Δp verwendet werden.

Das Hauptziel dieser Arbeit besteht darin, den universellen Anspruch des Kanal-Film-Modells zu untersuchen und seine Anwendbarkeit um wichtige Kenngrößen zu erweitern. Die Untersuchungen zielen dabei nicht nur auf mögliche Modellerweiterungen ab, sondern auch auf bisher im Verborgenen liegende Grenzen des Modells. Direkte und indirekte Hinweise auf solche Grenzen finden sich in der Literatur zumeist in Form von unbekannten Phänomenen beim Übergang eines Ölnebelfilters in den stationären Zustand und darüber hinaus.

Die vorliegende Arbeit umfasst eine kritische Prüfung der einschlägigen Literatur, eine Eingrenzung des thematischen Rahmens sowie des gesteckten Ziels dieser Arbeit, fünf Hauptkapitel mit neuen Ergebnissen, ein zusammenfassendes Fazit sowie einen Ausblick. Vier der Hauptkapitel (Kapitel 6, 8, 9 und 10) sind unabhängig voneinander weil in ihrer Form bereits veröffentlicht. Kapitel 7 basiert teilweise auf einer Publikation, enthält aber auch unveröffentlichten Inhalt. Die Hauptkapitel widmen sich folgenden Untersuchungen:

- Der Einfluss der Anströmgeschwindigkeit auf $\Delta p_{channel}$ und Δp_{jump}.
- Die Ursache von Δp_{jump} und sein Zusammenhang mit der Filmstruktur.
- Eine Erweitung des Kanal-Film-Modells um die Effizienz.
- Der Anstieg von Δp über den stationären Zustand hinaus.
- Die Genauigkeit von Porengrößenverteilungen in Ölnebel-Filtermedien.

Die Untersuchungen sind überwiegend experimenteller Natur und beschränken sich auf weitverbreitete Glasfaserpapiere (benetzbar und nicht-benetzbar), welche zu mehrlagigen ebenen Filtern konfektioniert werden. Für die Generierung von sub-mikronem Ölnebel wird ein repräsentatives Öl für Schraubenkompressoren verwendet. Ölanlieferraten wurden zwischen 5 und 1100 mg/(m^{2}s) variiert; Anströmgeschwindigkeiten zwischen 5 und 70 cm/s. Die Bereiche dieser beiden prominenten Betriebsparameter decken nahezu alle Anwendungen der Ölnebelfiltration ab.

Im ersten Hauptkapitel, **Kapitel 6**, wird anhand eines repräsentativen benetzbaren Filtermediums untersucht, inwiefern Δp_{jump}, $\Delta p_{channel}$ und die Sättigung im Kanalbereich von der Anströmgeschwindigkeit und der Ölanlieferrate abhängen. (Der Einfluss der Anströmgeschwindigkeit fand keine Berücksichtigung bei Kampa.) Im Rahmen der Messgenauigkeiten ist Δp_{jump} unabhängig von diesen beiden Betriebsparametern. Der Einfluss von abgeschiedenem Öl auf $\Delta p_{channel}$ wird anhand des Exzess-Δp, $\Delta p_{channel}$-Δp_0, untersucht. Das Exzess-Δp nimmt mit der Ölanlieferrate zu, bleibt aber weitgehend konstant mit der Anströmgeschwindigkeit. Mit anderen Worten: Gleiche Ölmassenströme resultieren auch in einem gleichen Wert für den exzess Kanaldruckverlust und größere Ölmassenströme benötigen mehr exzess Kanaldruckverlust. Daher lässt sich das Exzess-Δp auch als die für den Öltransport benötigte Energie interpretieren.

Ein konstantes Exzess-Δp bei gleicher Ölanlieferrate aber unterschiedlicher Anströmgeschwindigkeit wird dadurch erreicht, dass bei höheren Anströmgeschwindigkeiten sich die Sättigung im Kanalbereich reduziert. Aus Bildanalysen des Kanalbereichs geht hervor, dass sich die Sättigung dabei über den Kanaldurchmesser und nicht über die Anzahl der Kanäle anpasst. Diese Beobachtung lässt sich auf die Koaleszenzkaskade im vordersten Bereich der Ölnebelfilter zurückführen. Hier wird der Großteil der feinen Öltröpfchen abgeschieden und koalesziert in größere Tropfen, welche letztendlich in einen Ölkanal münden. Weder das Einzugsgebiet für einen Kanal noch die Koaleszenz von verschiedenen Kanälen untereinander scheinen dabei von den beiden untersuchten Betriebsparametern abzuhängen.

In Kapitel 6 wird des Weiteren das Phänomen eines (sehr) langsamen Anstiegs von Δp über den stationären Zustand hinaus vorgestellt. Dieses Phänomen des sogenannten Kriechens des Druckverlustes nimmt mit der Ölanlieferrate und der Anströmgeschwindigkeit zu und wird in Kapitel 9 detailliert behandelt.

In **Kapitel 7** wird aufgezeigt, dass Δp_{jump} sich aus der Kapillarität von benetzbaren Filtermedien ergibt und nicht aus der Filmdicke, wie es die Veröffentlichungen von Chang et al. (2016, 2017) nahelegen. Eine gute Näherung für

Δp_{jump} ist der sogennante Bubble Point, der dem kapillaren Austrittsdruck der größten Poren im Filtermedium entspricht und sich mittels Kapillarflussporometrie bestimmen lässt. Experimente wurden mit 4 verschiedenen Medien mit größten Porenklassen zwischen 28 und 47 µm und Anströmgeschwindigkeiten zwischen 5 und 70 cm/s durchgeführt. Abgesehen von einer erheblichen Streuung der Messwerte bleibt Δp_{jump} dabei annähernd konstant. Daraus lässt sich schlussfolgern, dass die Anzahl der Poren in der größten Klasse für die meisten Volumenströme in industriellen Anwendungen ausreicht.

Im darauffolgenden **Kapitel 8** wird das Kanal-Film-Modell erfolgreich auf die Effizienz von Ölnebelfiltern übertragen. Es wird ein neuer Ansatz vorgestellt, mit dessen Hilfe sich der Gesamtwirkungsgrad mehrlagiger Filter in die jeweiligen Beiträge des Films, der Kanäle sowie den Koaleszenzbereich in der ersten Lage von benetzbaren Filtern zerlegen lässt.

Alle untersuchten Medienlagen (je zwei Arten von nicht benetzbaren und benetzbaren Medien) verlieren einen wesentlichen Teil ihrer Effizienz durch die Beladung mit Öl. Die erste Lage weist die höchste Sättigung und damit den größten Unterschied zwischen Nass- und Trockeneffizienz von kleineren Tröpfchen (<100 nm) auf. Größere Tropfen (>500 nm) hingegen werden besser abgeschieden – vermutlich aufgrund der höheren Geschwindigkeit im Inneren der ersten Lage. Eine typische Kanallage verliert an Effizienz in allen Größenklassen, wobei die nicht benetzbaren Medien effizienter bei der Abscheidung von größeren Tropfen sind. Für alle Medien verhält sich der Film wie ein Trägheitsabscheider mit einer 50%-igen Abscheidung für etwa 250 nm große Tröpfchen. Größere Tropfen werden daher durch den Film fast vollständig getrennt, während kleinere Tröpfchen diesen ohne signifikante Abscheidung passieren.

Die Weiterentwicklung des Kanal-Film-Modells ermöglicht es, den Fraktionsabscheidegrad von Ölnebelfiltern mit zunehmender Lagenzahl vorherzusagen. Bei einlagigen Filtern bestimmt die Abscheidung des Films den Gesamtwirkungsgrad. Mit zunehmender Lagenzahl verliert die Filmeffizienz an Bedeutung und die Abscheidung im Kanalbereich dominiert. Die Erkenntnis über eine signifikante Abscheidung von größeren Tröpfchen durch den Film relativiert die oft betonte Rolle der Geschwindigkeitserhöhung im Filterinneren und erklärt scheinbar widersprüchliche Daten in der einschlägigen Literatur.

Anhand von Messungen der Gesamtzahlkonzentration wird außerdem gezeigt, dass die Erzeugung von Nebel durch platzende Blasen im Film mit zunehmender Effizienz oder Anzahl an Filterlagen an Bedeutung gewinnt. Dieses Sekundäraerosol stellt nicht nur für die Emission von Ölnebelfiltern eine Untergrenze dar, sondern auch für die Anwendung des weiterentwickelten Kanal-Film-Modells in dieser Arbeit.

In **Kapitel 9** wird der stationäre Zustand für den kontinuierlichen sowie diskontinuierlichen Betrieb von Ölnebelfiltern eingehend betrachtet. Der Einfluss der Filtermedienstruktur auf das Phänomen des Kriechens wird anhand von vier benetzbaren Medien (von offen- bis feinporig) untersucht. Filtrationsversuche werden sowohl mit anfänglich trockenen als auch mit vorgesättigten Filtern durchgeführt.

Vorgesättigte Filter weisen generell höhere Werte für Druckverlust und Sättigung auf, was sich auf die beobachtete Abwesenheit von Ölkanälen und eine homogenere Verteilung des abgeschiedenen Öls zurückführen lässt. Bei offenporigen Filtermedien sind die Unterschiede im Druckverlust des stationären Zustands zwischen vorgesättigten und anfänglich trockenen Filtern kaum wahrnehmbar; nehmen aber mit zunehmender Feinheit deutlich zu. Während sich die Sättigung S von anfänglich trockenen Filtern umgekehrt proportional ($S \sim v^{-1}$) zur Anströmgeschwindigkeit v verhält, schwächt sich diese Abhängigkeit bei vorgesättigten Filtern deutlich ab ($S \sim v^{-0.23}$).

Im *kontinuierlichen* Betrieb erreichen vorgesättigte Filter relativ rasch einen stationären Zustand mit einem konstanten und zeitlich stabilen Druckverlust. Bei anfänglich trockenen Filtern beobachtet man dagegen einen langsamen Anstieg von Sättigung und Δp über den stationären Zustand hinaus. Letzterer ist bei anfänglich trockenen Filtern durch ein zeitliches Abflachen des Druckverlustes und den Beginn der Drainage gekennzeichnet. Das Kriechen von Sättigung und Δp wird durch Ölanlieferraten von 1100 mg/(m^2s) beschleunigt und in zeitlich begrenzten Experimenten (100 Stunden) untersucht. Bei offenporigen Filtermedien ist das Kriechen nach weniger als 20 Stunden Beladung beendet. Diese Filter nähern sich der Sättigung ihrer vorgesättigten Vergleichsexperimente aber ohne einer Konvergenz des Druckverlustes, da die Ölkanäle erhalten bleiben. Feinporige Filtermedien zeigen zwar ein ähnliches Verhalten, erreichen allerdings nie einen echten stationären Zustand innerhalb einer praktikablen Beladungszeit. Die Ursache für das Phänomen des Kriechens ist offenbar die Abscheidung und Ansammlung von feinsten Öltröpfchen in der Tiefe des Filters zwischen den Ölkanälen.

In Kapitel 9 wird auch untersucht, inwiefern sich der *diskontinuierliche* Betrieb auf die Sättigung und den Druckverlust auswirkt. Bei einer Unterbrechung der Filtration kommt es in anfänglich trockenen Filtern zu einer kapillaren Umverteilung der Flüssigkeit und zu einer homogeneren Verteilung des Öls. Das Fortsetzen der Filtration führt daher zu einem sprunghaften Anstieg von Δp auf ein höheres stationäres Niveau. Der Anstieg des Druckverlusts begrenzt sich allerdings auf wenige Ein-Aus-Zyklen und bleibt dabei weit unter dem deutlich höheren stationären Δp von vorgesättigten Filtern. Der vorgesättigte

Zustand kann allerdings auch für anfänglich trockene Filtermedien erreicht werden: Eine Reduzierung der Anströmgeschwindigkeit führt entsprechend der o.g. Korrelation, $S \sim v^{-1}$, zu einer deutlich höheren Sättigung. Wird nach einer solchen Vorsättigung im Betrieb die Anströmgeschwindigkeit wieder auf ihren ursprünglichen Wert erhöht, geht die Struktur der Ölkanäle unwiederruflich verloren, und der Filter befindet sich im gleichen Zustand wie sein vorgesättigtes Äquivalent.

Das letzte Hauptkapitel, **Kapitel 10**, untersucht die Genauigkeit der Kapillarflussporometrie als eine Schlüsselmethode zur Charakterisierung von Porengrößenverteilungen von Filtermedien aus Mikroglasfasern. Fluorkohlenwasserstoffe, die häufig bei dieser Methode als Benetzungsflüssigkeit zum Einsatz kommen, verdunsten während einer Messung mit trockener Druckluft. Die Verdunstung beschleunigt sich insbesondere, wenn die Probenoberfläche von einem nassen in einen feuchten Zustand übergeht. Dieses Phänomen wird durch eine abrupte und charakteristische Trennung in der Mitte der Porengrößenverteilung sichtbar und führt dazu, dass ein Großteil der kleineren Porenklassen sich nicht in den Messergebnissen widerspiegelt. Die Lage der Porengrößenverteilung wird daher durch die Kinetik der Verdunstung bestimmt und ist damit für unterschiedliche Labore und Messgeräte kaum kontrollierbar.

Eine zuverlässigere Messung von Porengrößenverteilungen lässt sich unter Verwendung von schwerflüchtigen Silikonölen durchführen. Messungen mit dieser Benetzungsflüssigkeit zeigen, dass etwa 20% der Porengrößenverteilung in dem untersuchten Medium kleiner als 2 µm sind, was in etwa 400 mbar Differenzdruck entspricht. Aufgrund des hohen Kapillardrucks in diesen Porengrößen kann die hier eingeschlossene Flüssigkeit nicht mittels Kapillarflussporometrie, und darüber hinaus auch nicht in Filtrationsvorgängen durch Luft verdrängt werden. Des Weiteren kann ein Einfluss der Viskosität des Benetzungsmittels, wie in der Literatur vermutet, nicht nachgewiesen werden.

Zusammenfassend lässt sich sagen, dass in der vorliegenden Arbeit das Kanal-Film-Modell für variable Betriebsbedingungen validiert und um den Fraktionsabscheidegrad erweitert wird. Die Erweiterung des Kanal-Film-Modells ermöglicht daher die Auslegung von Ölnebelfiltern bei vorgegebenen Grenzwerten für Druckverlust und Effizienz in stationärem Zustand. Im Kontext des erweiterten Modells werden auch etablierte, manchmal jedoch widersprüchliche Erkenntnisse aus der einschlägigen Literatur neu bewertet. Dabei bilden die in dieser Arbeit aufgedeckten, bisher noch unbekannten Phänomene bei der Beladung von Ölnebelfiltern ein Schlüsselelement, um diese scheinbar konträren Positionen zu vereinen.

3

Introduction

Air-borne oil droplets (so-called mist) can be found in a variety of technical applications such as the crankcase ventilation of engines, metal cutting, natural gas production and the operation of oil-flooded screw compressors. Possible mechanisms for the generation of mist range from dispersion and atomization of liquid to condensation and nucleation of oil vapor. The resulting droplet size distributions may comprise multiple modes spanning several orders of magnitude. While larger droplets typically do not leave the apparatus, due to their tendency for gravimetrical settlement or inertial deposition, sub-micron droplets can easily follow the air stream and thereby get released. This leads not only to an increased oil consumption but may also result in harm to products, the environment or even humans.

In order to remove such fine mist, multi-layered filters of highly efficient glass microfiber papers are often used. Mechanisms of oil mist capture have much in common with classical areas of filtration such as solid-liquid separation and dust filtration. Nevertheless, oil mist filters represent their own (but less well understood) class of coalescence filters because of the mobility of deposited oil. These filters stand out due to a complex multi-phase flow and other particularities which distinguish them from filters which are “just” retaining particles. Unlike filters which have to be replaced when fully loaded, the deposited liquid drains at the filter rear-side in direction of gravity. This results in an equilibrium between the oil flow entering and exiting the filter. Pressure drop and fractional efficiency are observed to be steady at this equilibrium.

The steady-state performance of a mist filter is worse than in the dry filter in that the efficiency is significantly lower while the pressure drop typically more than doubles. The steady state is therefore of utmost importance for comparisons between different mist filters. The transition of the pressure drop into steady state can be attributed to the formation of liquid channels and films (Kampa et al., 2014). However, there are also transitional phenomena beyond the steady state which have received much less attention. Flow interruptions are known to shift the pressure drop irreversibly to a higher level (Frising et al., 2005; Bredin and Mullins, 2012) and continuous loading curves in the relevant literature show a slow but steady increase of pressure drop during their "steady" state (Contal et al., 2004; Frising et al., 2005; Mead-Hunter et al., 2013). Obviously, the universality of this state is limited in many aspects, implies additional and yet unidentified phenomena and in any case deserves an in-depth investigation.

To date, transitional phenomena during the evolution of the pressure drop are best characterized by the *Film-and-Channel-Model* by Kampa et al. (2014). This model describes phenomenologically the transport of deposited and coalesced oil in channel patterns within the filter medium and across a thin liquid film at the interface between the filter medium and air (wettable filters: rear side; non-wettable filters: front side). The formation of oil channels and films is reflected in the evolution of a filter's pressure drop, Δp, which can therefore be divided into contributions by each of the two structures. Kampa et al. (2015) describe the pressure drop responsible for the transport in oil channels, $\Delta p_{channel}$, as a parameter governed mainly by the properties of the liquid flow. This influence has been quantified for various filter media, oil viscosities and oil loading rates (Kampa et al., 2015; Chang et al., 2018a). Less common ground in the literature can be found for the underlying reason of the air flow's pressure drop to overcome the liquid film. Kampa et al. attribute the film's pressure drop to capillary properties of the filter media. On the other hand, Chang et al. (2016, 2017) consider the film thickness as the major contributor to this pressure loss.

The existence of oil channels and films can explain most transitional phenomena observed in mist filter loading curves but leaves open how these structures affect the fractional efficiency. In fact, contradicting findings for the efficiency can be found in the relevant literature. Experimental investigations are complicated by the so-called re-entrainment which is a generation of droplets due to bursting bubbles on the rear side of a filter (Wurster et al., 2015). This secondary aerosol is hard to separate from truly penetrating droplets on the downstream side of the filter.

The aim of this thesis is to investigate to what extent the phenomenological Film-and-Channel-Model can be extended and generalized. This work focuses on investigations on the influence of the filter face velocity on the pressure drop, filter media properties, and methods for evaluating the fractional efficiency. Besides pressure drop, the prediction of efficiency plays an outstanding role for the design of oil mist filters in their steady state. However, most important for the application of such filters is the reliability of steady-state values. Any changes due to unidentified transitional phenomena – even the slow ones – may question the validity of this state as a common reference point.

4

Critical review of the state of knowledge

4.1 Characterization of glass fiber filter media

Characterization with regard to structure

The structure of glass microfiber media is determined in a wet-lay manufacturing process in which an aqueous suspension of glass fibers and additives is filtered and dewatered upon a wire mesh. The resulting thin and highly porous glass papers are the outcome of a complex combination of machine settings, a mix of various fiber distributions, a binder (e.g. acrylic or latex), and optional surface coatings. It is nearly impossible to obtain useful information about input parameters of commercially available glass papers because they are treated as highly confidential by their respective manufacturer. Scanning electron microscopy (SEM) images, such as in Fig. 4.1a illustrate the complex arrangement in which an organic binder freezes finer fibers in a matrix of coarser fibers.

The resulting overall distribution of fiber sizes may be obtained through image analyses (Hotaling et al., 2015). These analyses are, however, prone to systematic errors such as the zoom level of the SEM images and the pronounced inhomogeneity of wet-laid glass papers (Hotaling, 2015). Some of these errors were eliminated in Fig. 4.1b by analyzing the circular cross sections of more

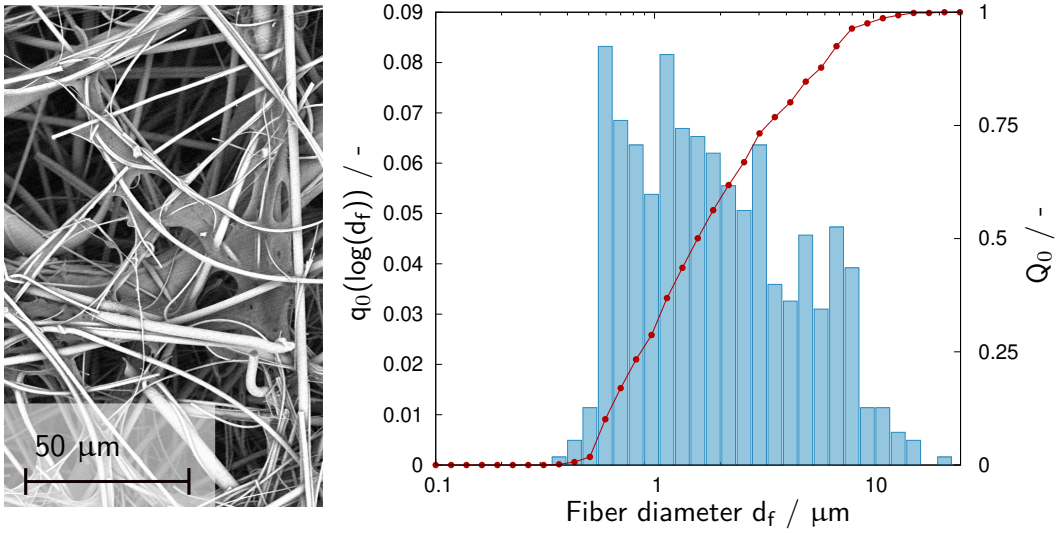

Figure 4.1: SEM image (a) of glass microfiber filter medium of "coarse" grade. Fiber diameter distribution (b) of the same medium measured by image analysis. Davies diameter of the medium was calculated to be 3.9 µm.

than 1000 fibers at different locations and at different magnifications. Width and modal values of the distribution in Fig. 4.1b lead one to suspect a filter medium composed of several fiber batches with numerous possibilities to achieve them in a bottom-up process. Aside from purposes of quality control or reverse engineering, knowledge of the fiber "recipe" prior to the manufacturing is of limited help to predict filter performance because it does not consider the cured binder between fibers. Own observations have shown that organic binder is unevenly distributed within a filter because it tends to migrate into regions of higher capillary forces (typically regions with predominantly fine fibers) during the drying process. Therefore, fiber sizes are also subject to a selective change during the wet-lay process, and this poses another systematic error of unknown extent for determining the relevant fiber distribution of filter media.

A very common approach is to substitute the actual fiber size distribution with a single, effective mean diameter (Davies, 1973). This so-called Davies diameter is based on a semi-empirical equation for the filter pressure drop, applicable to most filter media, and thus takes into account all kinds of inhomogeneity of the filter media. The calculation of this well-established diameter, d_f, according to Eq. 4.1 is based on easily accessible input, such as the air viscosity μ_{air} and measurements of Δp at a fixed face velocity v_0:

$$\Delta p = 64\,\alpha^{1.5}\,(1 + 56\,\alpha^3)\frac{\mu_{air}\,v_0\,L}{d_f^2} \tag{4.1}$$

Macroscopic properties such as the mass per unit area, solidity α, thickness L are equally straightforward to establish and often provided by manufacturers. Due to the nature of the wet-lay process, thickness and porosity (1-α) of commercial glass papers vary little between media. Thicknesses are typically between 0.4 and 0.8 mm and the porosity ranges from 94 to 95%. More significant differences can be found in the Davies diameter which may vary between about 1 µm for fine and 4 µm for coarse grades of glass fiber filter media. Variations in content of finer fibers have little effect on the mass-weighted average of the fibers distribution, but contribute significantly to Δp and filter efficiency.

Characterization with regard to wettability

The wetting behavior of a liquid on a solid surface is quantified by the angle θ between the flat solid surface and the tangent at the contact line of the two phases (Young, 1805). A more fundamental differentiation (which is an important feature for mist filtration) is done by dividing into *wettable* ($0°<\theta<90°$) and *non-wettable* ($90°<\theta<180°$) combinations of liquid and solid. On solid samples, contact angles θ are commonly analyzed by depositing a droplet of known surface tension onto a horizontal surface, and visually determining the slope of the tangent at the contact point of the droplets contour. This so-called sessile drop method is well-established (Marmur, 2006), and various models allow for additional consideration of e.g. dynamic effects or rough surfaces (Wenzel, 1937; Cassie and Baxter, 1944; Dettre and Johnson, 1969).

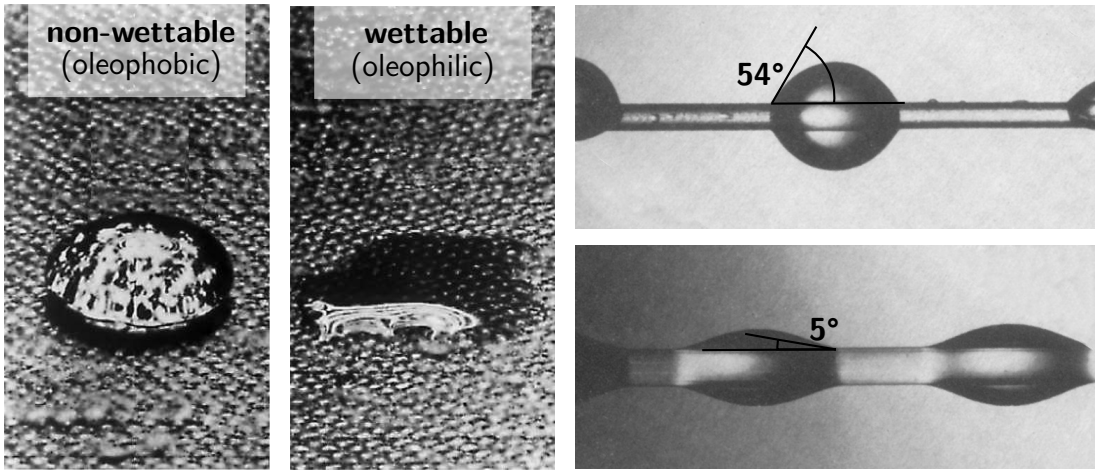

Figure 4.2: Sessile drop of alkane on non-wettable fibrous surface (a). Partially imbibed drop of alkane on the same non-wettable medium (b). Contact angle measurement of barrel-shaped droplets on individual fibers (c). Figs. 4.2a and 4.2b are taken from ISO 14419 and Fig. 4.2c is adopted from Carroll (1976) .

Contact angle measurements according to the sessile drop method are not feasible for wettable filter media because they imbibe the wetting liquid instantly. Non-wettable media preserve the shape of droplets and thus allow further analyses as described e.g. by an international standard (ISO 14491) for the resistance of textiles against hydrocarbons. In this test, drops of 8 linear alkanes with decreasing chain lengths (and hence surface tensions) are consecutively placed on the fibrous surface of a filter medium. The specific alkane which marks the transition from imbibed to repelled drops is an indicator for the oil repellency or the "non-wettability" of the fibrous medium (cf. Fig. 4.2). This test is commonly used also to specify the wettability of commercial fibrous filter media. It divides non-wettable media into classes from 0 to 8, 8 being the most repellent for oil, while 0 means total wettability. The fibrous media surface, however, substantially affects the shape of the droplets by its "roughness", and hence this test somewhat accounts for the structure of non-wettable filter media.

On a macroscopic scale, contact angle measurements are largely independent of the drop size. This does not apply to the micro-scale, e.g. isolated fibers in the depth of the filter, because of their increasingly curved surface. Wetting of curved surfaces affects the Laplace excess pressure within the droplets by their principal radii (de Gennes et al., 2004). This is the driving force of the Plateau Rayleigh instability of most films on fibers, because equivalent states of the Laplace excess pressure exist for various combinations of the two principal radii of curvature (Plateau, 1873; Lord Rayleigh, 1880). Even perfectly wetting combinations of fibers and liquids may break up into chains of equally spaced drops along the fiber due to the instability. Phenomenologically, the drops can occur either barrel-shaped (axis-symmetric) or in the shape of a clamshell (not centered on the axis of the fiber).

Contact angle measurements of individual drops, as illustrated on the right hand side of Fig. 4.2, are possible in a similar fashion as for the sessile drop method (Carroll, 1976). These contact angles do not only depend on liquid and solid bulk-properties but also on many other parameters, notably the fiber diameter and the droplet volume. Instead of a single contact angle the microscopic scale of fibrous filters is thus characterized by a broad range of contact angles. Mead-Hunter et al. (2014) summarize the relevant literature on the wettability of single fibers and point out that barrel-shaped droplets ($0°<\theta<90°$) are predominant in filter media of wettable macroscopic behavior, while clamshells ($60°<\theta<180°$) occur more often in non-wettable media. It is important to note, however, that both shapes coexist in a given type of media. Although methods for the characterization of individual droplets and their movement on single fibers by numerical calculations have been established

(McHale et al., 2001; Mead-Hunter et al., 2012), the consequences for the meso- and macro-scale, which are key for the behavior of a filter, remain largely unknown.

Combined characterization of structure and wettability by means of capillary concepts

Although the concept of capillarity has often been applied to flow and Δp in porous media (Carman and Kozeny, 1956; Clarenburg and Piekaar, 1968), in the field of gas filtration it has never prevailed over the concept of expressing Δp by the combined drag force of a filter's structural elements, i.e. fibers or particles (Pich, 1966; Endo et al., 1998). This is due to the low solidity of air filters. The average distance between fibers is many times larger than the mean fiber diameter and therefore does not fit well into the phenomenological picture of a continuous channel structure for the air flow. In the field of liquid filtration, on the other hand, pore sizes are a well-established characteristic of capillary systems (Ripperger et al., 2012; Luckert, 2004) because they correlate well with solid particle sizes to be retained (Gong et al., 2018).

During the filtration of mist, both air and liquid are present within a filter, causing a cocurrent flow of the two phases driven solely by the air flow. Due to their extraordinarily fine fibers, microfibrous media exert also high capillary forces on the liquid phase. The separate flows of liquid and air are therefore expected to compete for pore space. In order to take capillary forces into account and model the oil transport (which no longer occurs on the scale of a single fiber after coalescence) as the flow through a capillary, one has to include not only the fibrous structure but also wettability or contact angles.

There are numerous approaches to derive a structural parameter related to pore size. For instance, one may use the hydraulic diameter, d_h, which is popular in engineering and does not require a contact angle. In porous media d_h is given by

$$d_h = \frac{4\,\varepsilon}{S_V(1-\varepsilon)} \tag{4.2}$$

wherein ε is the porosity and S_V the specific surface area (Stieß, 2008). The latter is too low for most glass microfiber media to be measured by common adsorption methods.

Some authors (Marmur and Cohen, 1997; Mullins et al., 2007) analyze both structure and wettability in porous media by modeling the kinetics of capillary rise height. In analogy to the advancing meniscus in a vertical tube or capillary, this method requires measurements of the liquid rise height, x(t), or of the

imbibed mass, m(t), as a function of time t. Average pore diameters, d_{pore} , and contact angles between liquid and walls are subsequently derived by fitting the data to theoretical models for capillary rise. A popular model is that of Lucas and Washburn (Lucas, 1918; Washburn, 1921). Other, lesser-known models are similar to (Green and Ampt, 1911; Barry et al., 2009), or are based on the Lucas-Washburn model (Lockington and Parlange, 2004).

Reed and Wilson (1993) and Mullins et al. (2007) applied the Lucas-Washburn model to implicitly describe the evolution of rise height x(t) in a vertical capillary:

$$t = \frac{32\,\mu}{g\,\rho\,d_{pore}^2}\left((x_\infty + x_0)\,ln\left(\frac{x_\infty}{x_\infty - x(t)}\right) - x(t)\right) \tag{4.3}$$

wherein μ and ρ (density) are properties of the liquid, g is the gravitational acceleration, and x_∞ is the capillary rise height at equilibrium of the participating forces. The latter is given by the classical expression

$$x_\infty = \frac{4\,\gamma\cos(\Theta)}{g\,\rho\,d_{pore}} \tag{4.4}$$

and contains surface tension γ and contact angle. It is important to note that for a media characterization based on the combination of Eqs. 4.3 and 4.4 the contact angle in Eq. 4.4 is not static as in equilibrium but dynamic because it is averaged during the rise of the liquid column.

Solutions proposed by other models, such as the model of Lockington and Parlange, are more complex and may require experimental parameters which are only accessible for low porosity systems such as soil, bricks and stones but not for high porosity fibrous media. A comparison by Mullins et al. (2007) showed that the Lucas-Washburn model is more suited for fibrous media than the one of Lockington and Parlange. However, neither model was able to fit the complete range of capillary rise experiments for glass fiber filter media. In the long-term range Mullins et al. reported irregularities in the evolution of x(t) which are difficult for any model to resolve. These irregularities are likely due to erratic pinning of dry regions being engulfed rapidly by oil. A fit of data and model in the short-term range (< 600 s) did however result in a better fit, but also in significantly larger pore sizes than for the entire dataset. As a result of their method, Mullins et al. established empirical relations between fiber diameter and pore diameter which range from about 10 to 90 µm in glass fiber media. Their fits of Eqs. 4.3 and 4.4 also resulted in dynamic contact angles of 73° for the initial dataset and 83° for the whole dataset. These results are in qualitative agreement with own experiments as shown in Fig. 4.3.

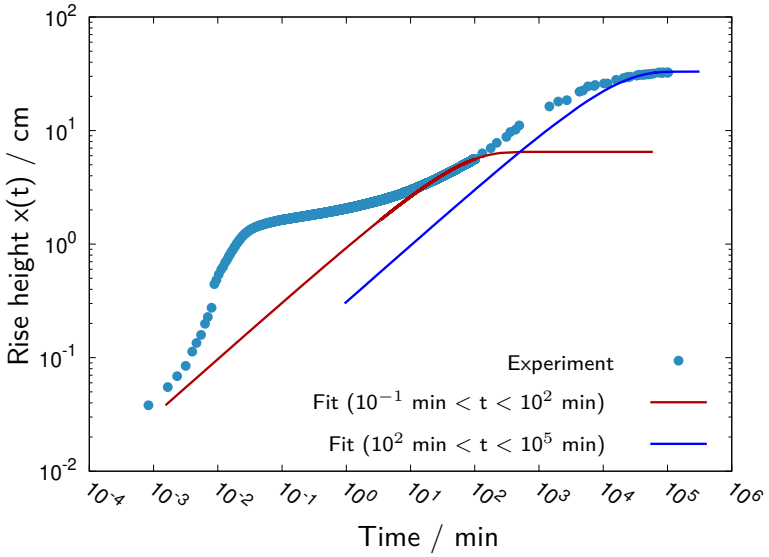

Figure 4.3: Measured evolution of capillary rise height x(t) in a strip of fine glass fiber medium in comparison with fits of the Lucas-Washburn model. The fits resulted in pore diameters of 75 and 11 µm and contact angles of 69°and 75°for the short- and the long-term range respectively.

Despite numerous applications, the classic Lucas-Washburn equation as given in Eq. 4.3, has often been questioned regarding its general validity (Rideal, 1922; Martic et al., 2002). It is known from experiments with circular glass capillaries that the advancing contact angle of a perfectly wetting liquid starts around 90° and approaches 0° at the equilibrium height of Eq. 4.4 (Sobolev et al., 2000; Siebold et al., 2000). These observations draw into question not only the higher contact angle derived for the long-term evolution in Fig. 4.3, but also cast doubt on methods in general which apply the kinetics of capillary rise height with a constant contact angle.

Another objection is the blurring of the wetting front, which is a fundamental requirement for the application of Eq. 4.3 (Dullien, 1992). Blurring of the wetting front has been observed for instance in masonry by Gummerson et al. (1979), but also applies to long-term experiments with glass fiber media and in particular to those with fine grades. This saturation gradient becomes especially pronounced in finer media. (Saturation is the ratio of oil volume to void space. It may take values between 0, for dry media, and 1, for media completely filled with liquid.) Segregation of the wetting front in the experiment of Fig. 4.3 becomes visible after about two hours. The saturation profile at the end of the experiment is given in Fig. 4.4. There actually seem to be two wetting fronts in vertical rise experiments: the lower front marks the end of completely filled pores, whereas the upper front marks the maximum height to which the liquid is able to rise.

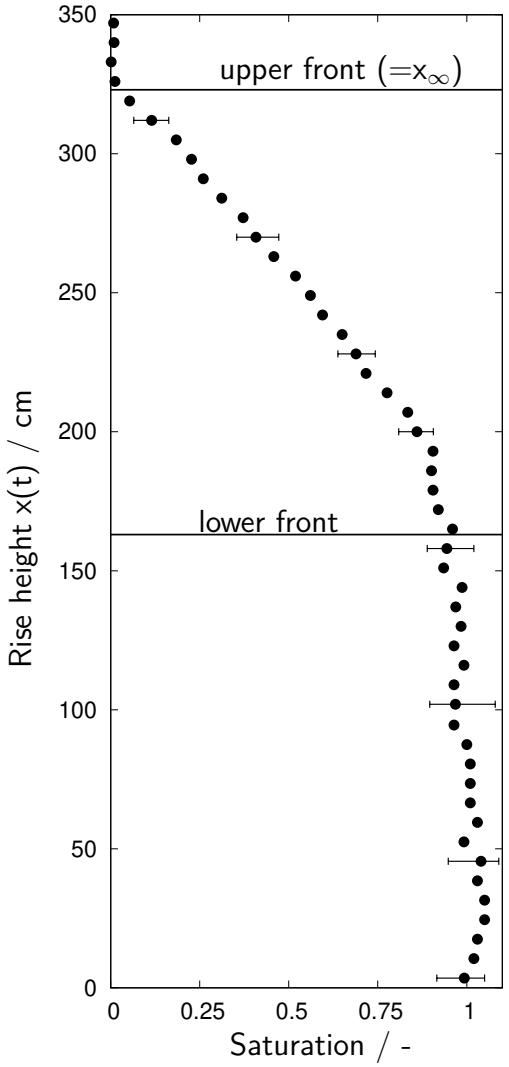

Figure 4.4: Vertical saturation profile measured gravitationally in a long strip of glass microfiber media after 80 hours of capillary rise. Saturation values are the mean of four experiments with error bars indicating the deviations.

It is important to note that capillary rise experiments result in pore sizes *perpendicular* to the actual flow during filtration. This is due to the fact that experiments have to be done in long vertical strips of thin glass paper where fibers are randomly distributed within the plane of a strip. In this set-up the liquid is drawn along the fibers by surface tension. During mist filtration, on the other hand, the coalesced liquid follows the air flow and hence is moving across the fibers. As a consequence, one may expect different pore sizes for liquid movement within the plane of a paper and perpendicular to it. This fact is borne out by work of Mullins et al. (2007) who compared their pore sizes calculated from rise experiments with values obtained by capillary flow porometry (across paper). According to their results, pore sizes obtained by capillary flow porometry are always significantly lower than those of capillary rise experiments.

Capillary flow porometry

The operating principle of capillary flow porometry is based on saturating samples of flat media with a wetting liquid, and then gradually "discharging" them with another fluid. This technique was firstly introduced by Erbe (1933), and is currently well-established with many variations for the discharging and wetting of samples with a broad variety of fluids (Dullien and Dhawan, 1974; Morison, 2008; Krantz et al., 2013). This thesis focuses on gas-liquid

displacement porometry which typically uses compressed air as the displacing fluid for measuring the pore size distributions between 1 to 50 µm in porous media. Not only is this technique applied commonly in commercial apparatus, but more importantly it is closest to the operating principle of mist filters, because it entails cocurrent flows of air and liquid.

Gas-liquid displacement porometry uses compressed air to gradually built up differential pressure Δp across a fully saturated sample with (almost) perfect wettability ($\cos(\theta) \approx 1$). Bubbles become visible once the capillary exit pressure of the largest pore is reached. Therefore, this point is also referred to as the bubble point, and by assuming pores of circular cross-section one may obtain the pore size corresponding to that pressure from classical capillary theory:

$$d_{pore} = 4\frac{\gamma \cos(\Theta)}{\Delta p} \tag{4.5}$$

As the air flow is increased, smaller pores are emptied when the respective capillary pressure is exceeded. Eventually, when all the pores have been discharged, the previously wet sample is completely dry. Surface tension γ and contact angle θ are assumed to be constant for all pores. The relative number of activated pores for a certain size (or Δp) can then be calculated from the ratio of the respective flow rates through the wet and the dry sample. Hence, the cumulative number distribution Q of these pores can be measured as follows:

$$Q(\Delta p) = 1 - \frac{\dot{V}_{wet}}{\dot{V}_{dry}} \tag{4.6}$$

The bubble point is of particular interest, not only because it is relatively easy to establish, but also because it offers more than just structural information. If the largest pore size is available from a previous experiment, e.g. conducted with a liquid of (almost) perfect wettability, the bubble point together with Eq. 4.5 may be used in a second experiment to determine the contact angle between the same type of medium and another wetting liquid. Furthermore, the bubble point may be used to characterize media for mist filtration, because Kampa et al. (2014) revealed a correlation between the bubble point and Δp_{jump} – a significant component of a mist filter's overall Δp.

Most publications apply capillary flow porometry to characterize membranes or fibrous filter media (Li et al., 2006; Aggarwal et al., 2012; Venugopal et al., 1999; Calvo et al., 1996). Some authors suggest corrections for the morphology of the pores (Yu et al., 2010), others introduce alternative calculations of the pore size distributions in order to extend the lower limit of detectable pore

sizes (Hernández et al., 1996). Due to its apparently good reproducibility, the fundamental reliability of this wide-spread method is often not questioned. However, Dixon (1998) reports significant deviations of the resulting pore size distributions for a wide range of commonly used wetting liquids on the same type of media. Yunoki et al. (2004) report similar observations – also caused by different durations of a measurement – and point to deviations in viscosity and kinetic effects as possible causes. In fact, volatility seems to be a crucial yet unexplored parameter because some wetting liquids, e.g. ethanol, as recommended by the underlying standard (ASTM F316-3) are highly volatile. Other more common liquids such as fluorocarbons and mineral oils may be considered low-volatile, but it remains unknown to what extent gas-liquid displacement porometry is subject to systematic errors due to the evaporation of the wetting liquid in fibrous media.

4.2 The effect of oil loading on pressure drop $\triangle$p and saturation of an oil mist filter

Single-phase flow through porous media has been addressed in science and engineering for decades with a vast number of models available for various technical applications. Even for the air flow and Δp through fibrous filters, there is a long list of potential models. A common approach, inherent to many of those models, describes the flow field around cylindrical fibers by a bottom-up method. Even with corrections for taking into account randomly distributed fibers and influences of neighboring fibers on the flow field (Kuwabara, 1959; Spielman and Goren, 1968), it is difficult to obtain realistic values of Δp for a wide range of filter media with these models (Shaw, 1978). Real filter structures comprise additional effects which are often intricate to measure, such as the change of fiber morphology due to the manufacturing process, and a visible inhomogeneity on the millimeter scale (sometimes referred to as “cloudiness”). This inhomogeneity is taken into account by Davies’ (semi-)empirical Eq. 4.1 which requires little input and no advanced mathematical methods, yet turns out to be in excellent agreement with many experimental results.

For mist filters, analytical models are far from being developed because they have to account for a cocurrent flow of air and deposited liquid. The flow field of the air, as the driving force for the oil flow, is therefore not only subject to a more complex structure of very fine fibers surrounded by deposited liquid but also to the moving boundaries of the latter. Unlike air, the source of liquid flow is not a uniform mass flow starting at the upstream face of the filter. Rather the source of the liquid flow is determined by aerosol deposition, and therefore, by

the air flow. Deposited liquid affects the air flow and thus subsequent deposition. Logical reasoning of this iterative process suggests the existance of a steady state in which the spatial distribution of deposited liquid and the Δp with regard to the air flow remain steady.

In such a steady state, the oil mass entering the filter as an aerosol equals the oil mass leaving the filter as drainage, penetration, and/or re-entrainment of droplets. Hence, the accumulated liquid mass (or saturation) and the Δp of mist filters are expected to remain constant. Steady-state operation can easily be deduced from a horizontal evolution of Δp, as shown in Fig. 4.5 for the case of a wettable and a non-wettable filter. Another indicator for steady state is the onset of drainage, which roughly coincides with the time when Δp levels off. Furthermore, the slope of the cumulative drainage in Fig. 4.5 seems to be constant and may be used to calculate the drainage rate. Mist filters consisting of a few layers of glass microfiber media are efficient enough to neglect penetration and re-entrainment in the outlet mass flow of liquid. The drainage rate may thus be used to estimate the inlet mass flow of oil or its loading rate.

Empirical models for Δp and saturation of oil loaded mist filters

The distinctive shape of typical loading curves as seen in Fig. 4.5 is difficult to handle for most models. Raynor and Leith (2000) therefore use purely empirical functions to calculate steady-state values for Δp and saturation. Another approach is to use force balances based dimensional analyses, which relate shear forces for driving the liquid through the filter to the surface tension force for retaining the liquid in the filter (Liew and Conder, 1985). Normal forces on

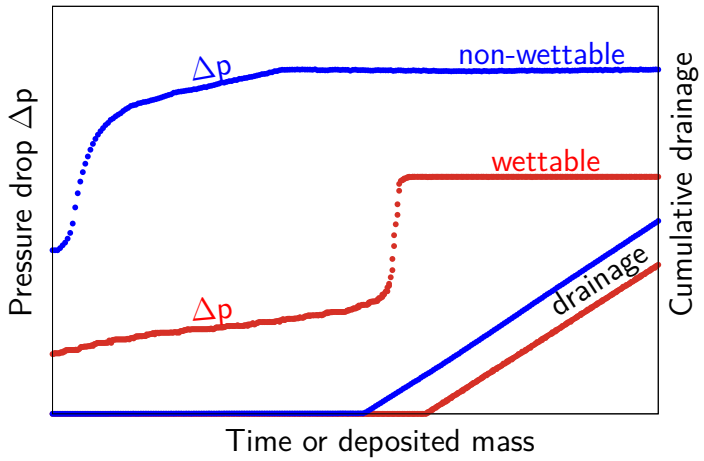

Figure 4.5: Evolution of Δp and drained mass of deposited oil for non-wettable and wettable filter media.

the liquid, which are thought to cause most of the liquid transport (Schubert, 1982), are however neglected. These models can give satisfactory results for a broad range of filter media and operating conditions but only for filters of similar thickness, because they use a constant value for global saturation.

A model by Gac (2015) reflects the loading behavior of wettable media well, but requires four parameters which have to be obtained by fitting the model to experimental data measured beforehand. It is not clear to what extent this model can be used for inter- and extrapolation of operating conditions or media properties. The model by Gac further assumes a uniform film covering the surface of the fibers. Such an assumption is also made by other authors (e.g. Agranovski et al., 2001; Frising et al., 2005) but has proven to be inappropriate in several aspects (Mullins and Kasper, 2006).

Phenomenological models for mist filter loading

The shape of loading curves such as in Fig. 4.5 invites for sectionwise linearization in search for the underlying physical mechanisms. Indeed, phenomenological observations proved to be useful in serving this purpose. A first approach by Contal et al. (2004) divides filter loading of wettable filter media into four stages, as shown in Fig. 4.6: During a first phase of static filtration deposited oil remains on the fibers; in a second stage the liquid coalesces and "fills" up some of the pore volume (linear increase of Δp); in a third stage the liquid rearranges itself and causes the steep increase in Δp; and eventually in the fourth stage of steady-state operation. The existence of the four loading stages, as described by Contal et al., was validated by others (Frising et al., 2005; Charvet et al., 2008; Kampa et al., 2014), and is widely accepted. Their interpretation with regard to oil transport, however, was questioned by Kampa et al. (2014) and lead to the development of an alternative phenomenological model.

The Film-and-Channel-Model by Kampa et al. (2014) does not fundamentally differ from the earlier model in terms of phases, except that these authors merge the first two stages of Contal et al. (2004) into a single stage. The overall wet Δp now consists of two separate contributions. The first, called $\Delta p_{channel}$, comprises the coalescence process of the liquid in the front-most layers and its subsequent transport within distinct "channels". The continuously advancing channel during loading is reflected in the evolution of the first linear section of Δp of the lower curve of Fig. 4.6. Once the channels reach the last layer of wettable media, the oil spreads laterally, thereby forming a thin film through which the air flow has to break. Film formation occurs quickly and can be seen as an (almost) vertical slope in Δp. Kampa et al. therefore named the second contribution of the film to the overall Δp as Δp_{jump}.

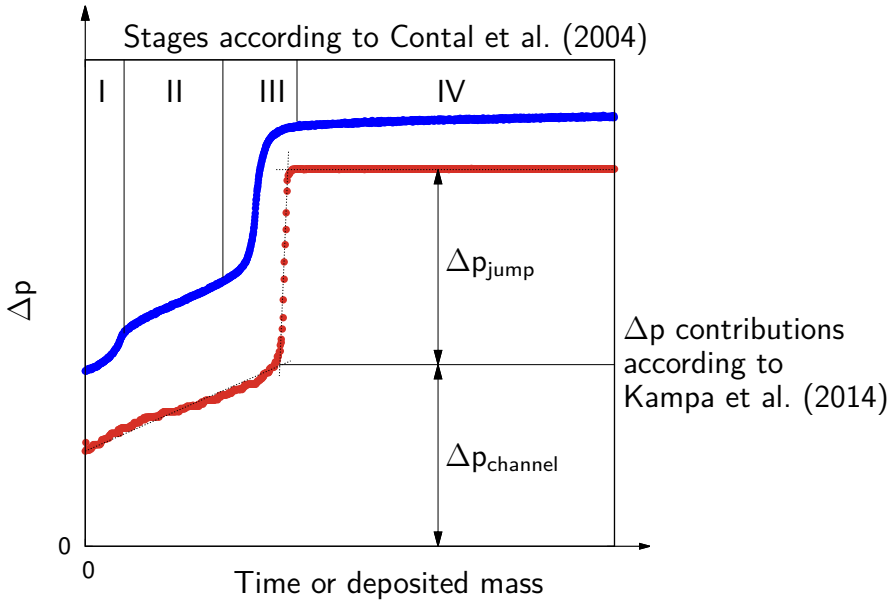

Figure 4.6: Evolution of Δp for two wettable media and classification of filter loading according to Contal et al. (2004) and Kampa et al. (2014).

The first stage in the Contal et al. model – not explicitly accounted for by the Film-and-Channel-Model – is neither necessary nor entirely superfluous. Moreover, this phase can be rather indistinct in the Δp curve of wettable filter media with only a slight "kink" or "wiggle" to mark its end. There is some evidence for this stage to become more pronounced in measurements with coarser media (Walsh et al., 1996). Kampa et al. (2014) acknowledge its existence – even though barely perceptible – also in finer media. All authors point to a transition from static to dynamic behavior of the liquid at that stage. Kampa et al. assume this transition to occur not on a microscopic scale as the onset of coalescence on single fibers but on a macroscopic scale as the starting point for the oil channels. They argue that coalescence occurs mainly in the first layer of multi-layered filters during the initial phase. As the oil accumulates to a transportable saturation it coalesces into channels and enters the next layer.

According to Kampa et al. (2015), $\Delta p_{channel}$ is influenced by both operating conditions and oil viscosity, the latter being the main parameter for the drag force on liquid traversing a filter. This behavior has been validated by several sources, in that increasing oil loading rates and oil viscosities lead to a higher saturation and thus a higher $\Delta p_{channel}$ (Kampa et al., 2015; Chang et al., 2018b; Penner et al., 2019). However, the literature is far from united regarding the underlying mechanisms of Δp_{jump}. Kampa et al. (2015) describe Δp_{jump} as a solely capillary phenomenon. The air flow passes the film – at a minimal cost of energy – by breaking through the largest pores. It is thus independent of any filter operating condition and can be estimated by means of Eq. 4.5 or simple

bubble-point experiments. Chang et al. (2016, 2017) on the other hand, observe an increase in Δp_{jump} with film thickness. They therefore ascribe Δp_{jump} to frictional losses of the air flow through the pores of the film.

The Film-and-Channel-Model applies also to non-wettable filters and combinations of both media types. In case of wettable media the film is formed on the front-most layer, thus inverting the sequence of $\Delta p_{channel}$ and Δp_{jump} (cf. Fig. 4.5). The effects of operating conditions on $\Delta p_{channel}$ can also be seen in non-wettable media: Kolb et al. (2015) and Chang et al. (2018a) report an increase in $\Delta p_{channel}$ with face velocity and oil loading rate. In addition, both authors present evidence that Δp_{jump} does depend to some extent on operating conditions and is thus also a dynamic phenomenon. Even though the influence of operating conditions and media properties on Δp is still not fully understood in all details, the Film-and-Channel-Model is capable of explaining the underlying physical processes in oil mist filters phenomenologically, and supports them with sufficient experimental evidence to demonstrate their broad applicability not only for wettable but also for non-wettable filter media.

Interrelationship between Δp and saturation

In a filter, saturation and Δp are closely related and respond jointly to changes in filter operation and media properties. This relationship should be discussed by means of the internal pressure drop, $\Delta p_{channel}$, because the "external" pressure drop, Δp_{jump}, does not depend on the film saturation ($S_{film} \approx 1$).

According to Mead-Hunter et al. (2013), in wettable media, an increase in Δp (either by means of a higher face velocity or a finer medium) leads to a decrease in saturation. Frising et al. (2005) obtained similar results for a variable face velocity in wettable media. Chen et al. (2018) validate these results for variable media grades and both types of wettability. This behavior is counterintuitive.

Unlike in the filtration of solids, the higher Δp is not due to more void space being occupied by liquid. Rather the higher Δp drives out more liquid and thus reduces saturation. Similarly, higher capillary forces and finer media grades (wettable) should lead to an enlarged capability to imbibe oil. This behavior of mist filters is thus unexpected and not in accordance with common knowledge of porous media.

Kampa et al. (2015) demonstrate that saturation and $\Delta p_{channel}$ shift towards higher values with increasing oil loading rate for both wettable and non-wettable media. However, this dependency is rather weak, because increasing the oil mass to be pumped through the filter by a factor of at least 40 resulted in a less than 20% increase of $\Delta p_{channel}$. The dependence on the viscosity is somewhat more pronounced in non-wettable media: an 8-fold increase of dynamic viscosity

resulted in about 40% increase of $\Delta p_{channel}$ and a 50% increase of saturation. Interestingly, the viscosity had no effect on the saturation or $\Delta p_{channel}$ in wettable media. Instead, with increasing viscosity the liquid distribution transitioned from small channels with fuzzy boundaries into larger and well defined channels (Kampa et al., 2015).

Saturation and Δp apparently "collaborate" with each other: when an external parameter acts on one of the two variables, the other counteracts to compensate the effect. This results in generally weak dependencies on operational parameters and viscosity. More pronounced are the effects of face velocity and media properties on Δp, entailing an even greater counter-action. All this contributes to the fundamental differences between mist and solid filtration.

Saturation in multi-layered filters

The saturation within a filter layer can be determined easily by weighing the liquid mass contained in it and relating its volume, V_{oil}, to the filters void space, V_{void}:

$$S = \frac{V_{oil}}{V_{void}} = \frac{V_{oil}}{\varepsilon V_{filter}} \tag{4.7}$$

Substituting with the volume of the entire filter, V_{filter}, results in a mean value for the global saturation. Filters composed of multiple layers allow measurements of S down to the thickness of a single paper layer. One may therefore determine saturation profiles across the depth of multi-layered filters. Such profiles are illustrated in Fig. 4.7 for a wettable and a non-wettable filter. Evidently, some layers contain significantly higher values of saturation than others. Comparing the global saturation of filters of variable thickness may therefore be a potential source for systematic errors of interpretation.

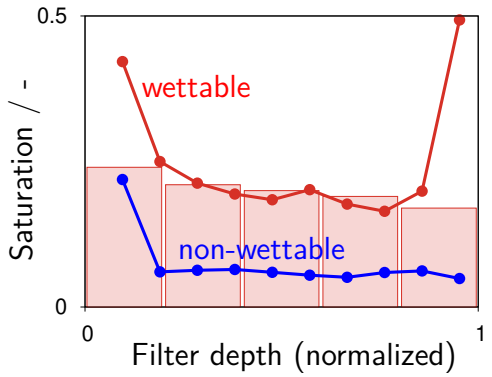

Figure 4.7: Saturation profiles in a wettable and a non-wettable filter (10 layers). Flat saturation profile of a wettable filter (5 layers) taken from Contal et al. (2004).

The shape of the saturation profiles in Fig. 4.7 is best explained by means of the Film-and-Channel-Model (Kampa et al., 2014). The U-shaped profile of the wettable filter starts with an increased value of the first layer, because

this layer serves as the coalescence stage. In it, oil requires more residence time to coalesce resulting in a lower transport velocity for the oil mass flow. Throughout the remaining layers, the saturation is roughly constant because the oil is transported in contiguous channels. At the downstream side of wettable filters the saturation increases again, because this is where the oil film is located. The absolute saturation of the rear-most layer is to be interpreted with caution, because it comprises both an almost fully saturated film and some channels at a significant lower saturation. In non-wettable media on the other hand, the film already occurs within the first layer and (mainly) takes over the role of the coalescence stage. Hence, the saturation of the first layer is increased while the subsequent channel layers are set at a lower and constant saturation level.

The published literature in this field largely agrees on the general shape of saturation profiles. Similar profiles for non-wettable media were observed by Kampa et al. (2015) and Chang et al. (2018a). The increased saturation levels at the front and rear of wettable media are reported by several authors (Bitten and Fochtman, 1971; Kampa et al., 2014; Chang et al., 2016). Other authors use a global saturation but indirectly their data acknowledge the U-shape with a dependence of saturation on the filter thickness (Raynor and Leith, 2000; Mead-Hunter et al., 2013). There seems to be evidence that a gradual decrease of saturation from front to rear is more pronounced for coarser media (Andan et al., 2008). This may be due to the lower efficiency of the first layer which shifts the coalescence zone deeper into the filter. It is important to note, however, that flat saturation profiles also have been measured in wettable media (cf. Contal et al., 2004 in Fig. 4.7). These observations were confirmed by Chang et al. (2016), who report a higher channel saturation at a constant saturation level throughout the complete filter. The measurements by Chang et al. seem however to be flawed by experimental issues (Kolb and Kasper, 2019b).

Up to now, the literature review has focused on filters, where the loading process starts with the dry filter, i.e. S=0. Few experimental data have been published about the consequences of starting a filtration experiment with S≠0. Mist filters typically start from a dry state, and may require several weeks or more without interrupting the loading process in order to bring saturation and Δp to an equilibrium (Bredin and Mullins, 2012; Mead-Hunter et al., 2013). Therefore, Mead-Hunter et al. reduced the time to steady state by starting their experiments with fully saturated media. These experiments reportedly resulted in the same steady-state Δp as for initially dry filters. Another experimental method of speeding-up the loading process, proposed by Kampa et al. (2008), involves starting from a high and switching to a lower loading rate once steady state is reached in non-wettable filters. These authors report significant differences between the steady-state Δp of initially fully

saturated vs. initially dry filters. The literature is not clear what causes the discrepancy between the observations by Mead-Hunter et al. and Kampa et al., but the differences bring up more fundamental questions: Are both filters (dry & pre-saturated) filled with the same amount of liquid once they are in steady state? Are liquid distributions in steady state identical or does the air flow prevent certain regions of the filter to be filled with deposited aerosol? Desaturation of initially fully saturated porous media by means of a second fluid always means that some of the original liquid is retained at fiber intersections and areas of higher capillarity (Schubert, 1982). Complete drying would thus require evaporation, which can be eliminated from the list of possible causes because of the low vapor pressure of the oil. It is unknown to date to what extent any residual saturation, e.g. from pre-saturated filters, contributes to saturation and Δp of a new steady state.

Computational Fluid Dynamics (CFD)

More theoretical approaches to model mist filtration are simulations which couple the flow of both liquid and air in a realistic fibrous filter. First calculations by Rothman (1990) simulated multi-phase flow in coarse systems with a negligible capillarity by using Darcys approach of permeability for small cells. Presently, direct numerical simulations are successfully able to couple air-borne droplet motion, deposition of droplets on dry and oil-loaded fibers, coalescence of droplets, motion of liquid drops on fibers (Mead-Hunter et al., 2013). However, these simulations are costly in terms of CPU-time and, therefore, limited to certain starting and boundary conditions. In order to avoid the time-consuming loading of dry fibers with oil, simulations often start with pre-saturated fibrous media (Golkarfard et al., 2016). At the moment they are limited to fiber diameters between 10-20 μm and domain sizes of less than 5 mm (Abishek et al., 2018), which makes them perfectly suitable for coarse fibrous media in which well-defined liquid channels are probably absent (Chen et al., 2018). Finer media such as glass microfibers develop millimeter-sized liquid channels and are thus challenging for simulations because finer fibers require a denser mesh while oil channels on the other hand require a much larger domain size.

4.3 The effect of oil loading on the filter efficiency

Droplet removal in dry filters

The deposition mechanism of fine droplets on dry fibers is (almost) identical to that of solid particles. A commonly used approach to quantify the efficiency E of a filter for both aerosol types is the single fiber theory. Its fundamental premise is the scalability of the deposition on a single fiber, E_{SF}, to the efficiency of randomly oriented fibers throughout the thickness H of a filter:

$$E_{filter} = 1 - P_{filter} = 1 - \exp\left(\frac{-4(1-\varepsilon)\,E_{SF}\,H}{\pi\,\varepsilon\,d_f}\right) \tag{4.8}$$

E_{SF}, often called single-fiber efficiency, can be interpreted as a dimensionless factor to adjust the cross section of the fibers relevant for the capture of each droplet diameter. Since the flow around any given fiber is affected by neighboring fibers, the flow field is modified for each deposition mechanism. For a combination of independent deposition mechanisms, E_{SF} may be calculated by considering the relevant mechanisms:

$$E_{SF} = 1 - P_{SF} = 1 - \prod_{\substack{\text{relevant}\\ \text{mechanism}}} P_i \tag{4.9}$$

Formulae for each mechanism – and interactions between them – are abundant in the literature (e.g. in Stechkina and Fuchs, 1966; Suneja and Lee, 1974; Lee and Liu, 1982; Schweers and Löffler, 1994; Müller et al., 2014). In principle, the relevant mechanisms for filtration of oil mist in glass microfiber media can be reduced to diffusional, interceptional and inertial deposition, and their respective dimensionless numbers.

Diffusional deposition on fibers is a result of the well-researched Brownian motion, while droplets are transported by air flow along the streamlines. The ratio of the convective transport by air and the diffusional transport towards the fiber surface may be described by the Péclet number:

$$Pe = \frac{v_i d_f}{D_p} \tag{4.10}$$

When the air flow upstream of a fiber changes its direction, larger droplets are not able to follow the streamlines and impact on the fiber. The driving force behind this deposition mechanism is the droplets inertia, which is determined by the air velocity v and density ρ as well as the droplet diameter. The density of oil mist is lower than that of most other aerosols. However, air velocities

between 5 and 30 cm/s and in particularly thin glass microfibers of mist filters may lead to significant Stokes numbers which describe the inertial deposition:

$$\mathrm{St} = \frac{\rho\, d_p^2\, C(d_p)\, v_i}{18\, \mu\, d_f} \tag{4.11}$$

The trajectory of a droplet's center might be calculated to pass a fiber. As the droplet's size is not limited to its center of gravity it might nevertheless be deposited on the fiber surface. This so-called interception is described by a dimensionless parameter R:

$$\mathrm{R} = \frac{d_p}{d_f} \tag{4.12}$$

Interception is most relevant in the size range of the most-penetrating particle size (MPPS), when both diffusion and inertia equally contribute to the overall efficiency. This characteristic point may be seen as a minimum of the fractional efficiency and lies at about 100 nm for glass microfiber media.

Change in efficiency while loading of mist filters

The air flow pattern within fibrous filter media changes with the accumulation of oil. On average the interstitial air flow velocity within the wet filter is accelerated by a factor of

$$\frac{1}{\varepsilon_{\mathrm{wet}}} = \frac{1}{\varepsilon_0(1-\mathrm{S})} \tag{4.13}$$

According to the single-fiber theory, an increased interstitial velocity results in less diffusional and more inertial deposition. Most experimental data seem to support this interpretation as dry penetration curves are typically shifted towards smaller droplets in steady state (Raynor and Leith, 2000; Agranovski et al., 2001, 2002; Charvet et al., 2010). This shift entails a crossover between the fractional efficiencies of dry and wet filters, as seen from the blue curves in Fig. 4.8. However, the saturation of fibrous mist filters typically remains below 50%, which limits the relative increase of the interstitial velocity during loading to less than 100%. Mead-Hunter et al. (2014) report an equal decline in efficiency on both sides of the MPPS, similar to the red curves in Fig. 4.8. This effect could be due to an increase in fiber diameter due to the accumulated oil. Such an increase could compensate the effect of a higher interstitial velocity for the inertial deposition by decreasing the Stokes number. Furthermore, it leads to higher Péclet numbers and thus reduces the diffusional penetration.

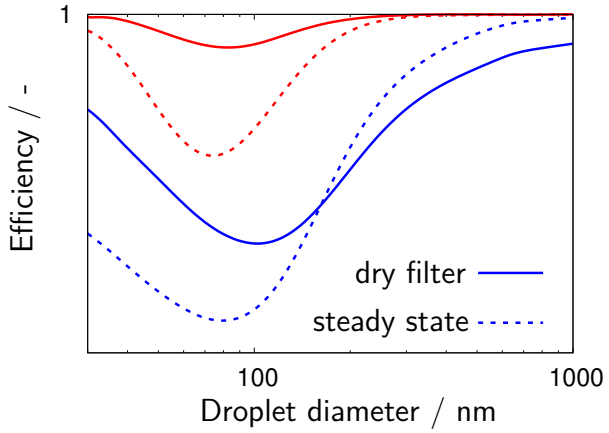

Figure 4.8: Fractional efficiency curves of a lower efficient filter (blue curves) and a higher efficient filter (red curves).

Liquid deposited on dry fibers may take various shapes and, therefore, does not only alter the deposition on oil coated fibers, but may also reduce existing or generate new collectors. Fine droplets coalesce into larger drops during filtration which may form barrel-shaped or clam-shell drops depending on a variety of parameters. Homogeneous liquid films on fibers are possible but subject to the Plateau-Rayleigh instability which causes a homogeneous liquid film to break up into a chain of equally spaced droplets. Theoretical considerations by Quéré (1999) suggest a film to be stable when the film thickness h is significantly smaller than the fiber diameter d_f:

$$\frac{h}{d_f} < \frac{1}{2}(\sqrt{2}-1) \tag{4.14}$$

According to observations by Mullins et al. (2006) the limit may be even lower. These authors also report a film of a few nanometers to connect equally spaced droplets. Newly arriving aerosol deposited on the thinly coated fibers can therefore be passed on and feed the larger droplets.

The literature does not provide much explanation how changes in air velocity and morphology of the highly efficient microfibers affect the overall efficiency of a filter. Some authors (Raynor and Leith, 2000; Conder and Liew, 1989) point out that large drops on fibers do not contribute significantly to filtration and thereby reduce the effective fiber length. Conder and Liew differentiate between active and non-active fibers in filters with void fractions below 96%. They distribute the liquid in such a manner that pools of oil take out large regions of fibers, while the remaining fibers uniformely increase their diameter by 10%. The apportionment of liquid was done by a least-squares fit to experimental data. These authors conclude that the negative effect of non-active fibers on the efficiency is more than compensated by an enhanced inertial and interceptional deposition due to changes in the flow field around the fibers, according to single fiber efficiency. Raynor and Leith come to the same conclusion but distribute the liquid as equally spaced droplets while retaining the dry fiber diameter.

Payet et al. (1992) distribute the deposited liquid within fully saturated regions of the same length as the filter thickness. Thus, the liquid partially blocks some of the filters volume. The resulting increase of the interstitial velocity and reduction in fiber length would explain an increasing penetration of droplets between 80 and 400 nm. However, the authors' model could not explain a very short but significant decrease of the penetration of 150 nm sized droplets during the loading of non-wettable filters. The efficiency models of both Payet et al. (1992) and Conder and Liew (1989) introduce empirical fits for porosity and solidity in the steady state such that $\varepsilon_{\mathrm{wet}} + \alpha_{\mathrm{wet}} > 1$. This assumption is questionable because the sum of both variables is widely accepted as unity.

The first model to abandon the concept of a global saturation and take into account the actual saturation profiles was developed by Frising et al. (2005). These authors distribute the liquid as a uniform film around the fibers and take into account the reduction of fiber length by the growth of the film at fiber intersections. The model was questioned by Mullins et al. (2006), as continuous and uniform films do not exist on fibers. Model and measurements by Frising et al. report an increased overall efficiency with face velocity – similar experimental results can be found elsewhere (Contal et al., 2004). Because Frising et al. base their discussion on total number efficiency, it remains unclear to what extent inertial and diffusional deposition impact the efficiency.

Aside from a broad variety of possibilities for distributing droplets and liquid films on individual fibers, the morphology of a liquid on the meso- and macro-scales within fibrous media offers even more possibilities for arranging liquid. Liquid bridges or droplets spanning a few fibers have been reported. Even larger structures such as completely filled oil channels (Kampa et al., 2014; Chang et al., 2018a), can span distances of several hundreds of parallel fibers. The formation of thick liquid films at the fiber intersections or between (almost) parallel fibers has also been reported (Mullins et al., 2006; Agranovski and Braddock, 1998). The physical dimensions of all these liquid structures remain quite small and certainly not more significant for the filter efficiency than the fibers. The liquid film on the other hand spans almost the entire filter surface. It is almost completely closed and contributes significantly not only to the overall Δp, but also to a change in total number concentration of the downstream aerosol (Kampa, 2015). Kampa shows the film to be responsible for a rapid decrease of the droplet concentration within the cleaned gas during its formation (also reported by Payet et al. (1992)) and points out the possibility that the film contributes to the enhanced deposition of larger droplets during steady state. Therefore, the improvement of inertial deposition reported by many authors is not only due to higher interstitial velocity but to an unknown extent also due to the film.

Re-entrainment of droplets

The issue of re-entrainment of liquid in sampling equipment, filters and separators has been known for decades (Ranz and Katz, 1959; Calvert et al., 1974; Liew and Conder, 1985). The phenomenon of entrainment of detached droplets (so-called blow-off) was first described by Souders and Brown (1934) for fractionating columns and also applies to low-efficiency filters with coarse fibers (El-Dessouky et al., 2000). Here, the increase of drag forces by the air flow might compensate for the increase of the required force for detachment (Wurster et al., 2015; Hotz et al., 2015). However, in high-efficient oil mist filters the air velocity is typically far below the range required for blow-off. In fact, the predominant cause for this phenomenon was first linked to bursting bubbles on the rear side of fibrous filters of finer grades (Joseph, 1984), and later investigated in detail by Wurster (2017).

Bursting bubbles are generated when the air flow exits from the rear side of a wet filter in steady state. In wettable media the liquid fills all pores on the rear-most side of the filter and becomes visible as a film. These pores are not constantly maintained open by the air flow, because the liquid drains within the film and may flow over the pore mouth. The air flow causes the film to form bubbles, whose cap ultimately bursts into numerous satellite drops. The spectrum of re-entrained drops may result in multi-modal distributions comprising droplet sizes from nanometers up to the millimeter range. After the onset of drainage, which may cause an initial peak of re-entrained droplets, the number concentration due to re-entrainment remains constant (Wurster et al., 2015).

In case of non-wettable media the liquid exits the channels on the rear-most side of the filter by forming large drops, which grow up to 5 mm in diameter because they are continuously fed by the channels. Eventually, the drops drain by gravity leaving behind liquid traces which form an (almost) closed film on the rear side of a non-wettable filter. Apparently, this film does not impact Δp but causes similar re-entrainment (in size and number) as does the film in wettable media (Wurster et al., 2015).

The erratic process of bubble bursting is one of the reasons why measurements of size and number of re-entrained droplets are subject to large errors. The generation of re-entrainment furthermore decreases with filter height and oil viscosity and increases with face velocity and loading rate (Wurster et al., 2017). The latter has a significantly higher impact on the re-entrained mass than the former. According to Wurster, this originates from a complex interaction between the perpendicular flows of oil and air.

4.4 Continuous vs. discontinuous filter operation

When filters are operated continuously under steady conditions, they are operated first and foremost at constant air flows and oil loading rates. As discussed in the previous chapters, continuous operation results sooner or later in a steady state at constant Δp and efficiency. Typical applications however often imply changes in operating conditions throughout a mist filter's lifetime. For instance a common and fundamental change is the interruption of filtration. In contrast to most dust filters, temporary interruption of a mist filter's steady state may lead to significant changes in Δp (Frising et al., 2005; Charvet et al., 2008; Bredin and Mullins, 2012).

Frising et al. (2005) and Charvet et al. (2008) conducted experiments with wettable filter media and intermittently interrupted filter loading. Neither group of authors observed any effect during the initial loading prior to steady state. However, when steady-state operation was stopped for about an hour and subsequently resumed at previous conditions, Δp increased by about 20%. Frising et al. (2005) point to the draining liquid as a possible cause. Liquid may be first imbibed from the rear side and subsequently distributed within the complete filter by capillary forces.

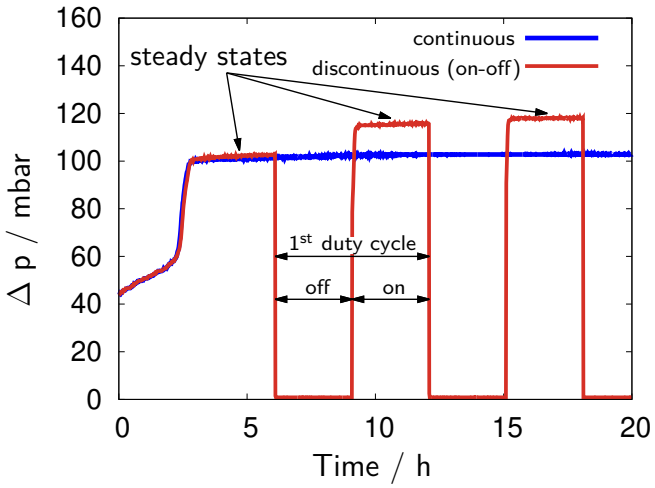

Figure 4.9: Continuous vs. on-off operation at a fixed duty cycle after the initial steady state.

This increase in Δp can be counteracted temporarily by purging filters with dry air. The ensuing Δp may even fall below the level of the first steady state, if the air flow within the purging phase exceeds the air flow during filtration (Frising et al., 2005). This regeneration in regard of Δp is due to the fact that liquid is driven out of the filter without replenishing it with new aerosol. It is not clear however, if such a process is reversible in terms of efficiency. In fact, data of Frising et al. contain evidence that Δp regeneration – in particular at higher air flows – causes a loss in efficiency.

A first systematical investigation of flow interruption was done by Bredin and Mullins (2012). Wettable filter media (stainless steel fibers) were first brought into steady state and subsequently operated in pre-set duty cycles. The results of Bredin and Mullins with wettable media are similar to own measurements with glass microfiber media shown in Fig. 4.9 (own investigations further showed that those authors' findings may be transferred to non-wettable media). Each subsequent steady state increased in Δp, efficiency and saturation for about 6 cycles and then remained constant throughout all following cycles. The rising tendency of the steady states resulted in a total increase of Δp of about 40% and occurred only when the filter was switched off for 2 hours at a time. When the pause was reduced to 30 seconds, while maintaining a 2h filtration phase, none of the measured parameters were affected.

According to Bredin and Mullins (2012) the oil creeps into regions during the "off-phase" where it has not been before. Recommencing the air flow induces shear forces on the liquid surface and partially pushes the oil back. Thus the retained oil contributes to saturation and Δp. After a couple of iterations the shear forces are eventually high enough to maintain the air region completely open. Bredin and Mullins further conclude that the "creeping" of oil is a slow process, and hence very short stops of the filtration process do not lead to sufficient rearrangement to take the filter out of the steady state.

5

Scope and objectives

The most important starting point of this work is the recent Film-and-Channel-Model by Kampa et al. (2014) because it has proven to be the only model in oil mist filtration without any fundamental flaws or inconsistencies with experimental observations. This model describes the structure and transport of liquid within multi-layer mist filters (channels and the film) and links them to the differential pressure drop, Δp. Moreover, it breaks down the overall Δp into contributions by the film (Δp_{jump}) and by the channels ($\Delta p_{channel}$) and makes predictions for filters with a variable number of media layers. The impact of certain parameters such as oil properties and oil loading rates on the individual Δp components has already been investigated in the context of this model. However, there are still numerous (fundamental) questions regarding the nature of these liquid structures and their complex interaction with the air flow.

For one, it remains unknown how films and channels change their structure with important filtration parameters such as media properties and face velocity, and how, in turn, these structural changes affect the respective values of Δp_{jump} and $\Delta p_{channel}$. In fact, the literature cites both the film thickness and its capillary exit pressure as two possible but fundamentally different root causes for Δp_{jump}. Hence, it is not clear to what extent those two parameters actually contribute to Δp_{jump}. Moreover, films and channels should not only contribute to a mist filter's Δp but also to its efficiency. At the outset of this thesis, there was no reliable model to predict the efficiency of mist filters. Both the incorporation of the face velocity and the efficiency was an important step

towards a fully validated Film-and-Channel-Model and its application for mist filter development.

A second, important issue concerns the continuous operation of mist filters in its steady state which is widely accepted as a filter benchmark and commonly believed to coincide with the simultaneous onset of drainage and pressure drop levelling off. Unfortunately, there is plenty of experimental evidence (discussed in Chapter 4) that this initial "steady state" is neither unique, nor actually steady. Steady-state Δp may vary for pre-saturated filters and is also not constant for discontinuous filter loading. Moreover, the evolution of steady-state Δp in numerous publications is not perfectly flat but shows a slight and systematic increase. Whatever causes this "Δp-creep", it draws into question the accuracy of "steady" states at the onset of drainage which may be significantly different from steady states achieved in longer experiments.

Finally, the previous chapter also identified open questions related to the characterization of filter media by capillary flow porometry. There are problems with the accuracy of this measuring technique as the resulting pore sizes seem to depend on the volatility and viscosity of commonly used wetting liquids, the modus operandi of the measurement, and the technical details of the respective instrument. Capillary flow porometry can therefore result in fundamentally different outcomes and is far from providing representative and reliable pore sizes distributions; something which is needed as a baseline to analyze how the air flow is distributed across the pores in the liquid film of mist filters.

The main goal of **Chapter 6** is to extend the validity of the Film-and-Channel-Model by investigating how face velocity and oil loading rate affect pressure drop and liquid hold-up in a wettable filter medium. More specifically, the objective is to show any dependencies between these operating conditions and the pressure contributions of Δp_{jump} and $\Delta p_{channel}$. The latter will be compared with a representative internal saturation which is the underlying cause of $\Delta p_{channel}$. Beside the total liquid volume (or saturation), it is also necessary to investigate how this liquid is distributed within the filter media.

Therefore, equivalent channel diameters and numbers will be derived from image analyses of oil-loaded media layers in order to discuss how the channel patterns react to changes of the air flow. The recognition of channels will apply the Film-and-Channel-Model's assumption of a perfectly heterogeneous liquid distribution, i.e. fully saturated oil channels in a dry filter media matrix. This simplified classification might serve the purpose of explaining the liquid transport but certainly does not apply to real mist filters. Therefore, the "heterogeneity" of the liquid pattern at a constant saturation will also be evaluated and discussed.

Chapter 7 investigates the dependence of Δp_{jump} on capillary and structural properties of the liquid film on the rear side of wettable mist filters. The first part of this chapter is procedural and addresses possible error sources during the derivation of Δp_{jump}, the exact location of the liquid film in the last layer, and a method to obtain a representative film thickness. It will also be shown how measurements of film thickness are affected by the presence of an additional "drainage layer", as often used on the downstream side of commercial mist filters. In a second part, a comprehensive set of film thicknesses and Δp_{jump} values will be obtained to derive a possible correlation between the two variables. In this context, it will be discussed whether frictional losses of the air flow in the pores of the film are responsible for Δp_{jump}. This clarifies questions arising from papers by Chang et al. (2016, 2017).

The last part of Chapter 7 addresses capillary properties as (another) possible cause for Δp_{jump}. It investigates how Δp_{jump} depends on the pore size distribution and most notably the capillary exit pressure of the largest pore, commonly referred to as the so-called bubble point. Dependencies and deviations of Δp_{jump} from the bubble point will be discussed by means of experiments with four media grades, ranging from coarse to fine and accounting for most industrial grades of glass microfiber media. In order to achieve multiple values of Δp_{jump} for different settings, experiments will be conducted with variable air flows. Therefore, Chapter 7 picks up the velocity dependence of Δp_{jump} in another context to validate the key findings of Chapter 6 for a wider range of wettable filter media and operating conditions.

The central objective of the following **Chapter 8** is to reveal the role played by channels and films in the efficiency of mist filters. Moreover, this chapter aims to provide a mesoscale model for the fractional efficiency (or penetration) of multi-layered filter media by modeling the sequential appearance of films, channels, and the first layer of wettable media as a series connection of independent penetrations.

At first, a method is to be developed to decompose the overall filter penetration of a filter sandwich into separate contributions of the respective structures. These individual penetrations through the liquid film, a representative channel layer and the first layer of wettable media are then compared against each other. For each sectional penetration, the relevance of classical filtration mechanisms (i.e. inertia, diffusion and interception) will be considered and discussed in detail.

Subsequently, the proposed model will be evaluated by a comparison of predicted and measured efficiencies of filters with a variable number of media layers. This validation will show the models technical capabilities to design mist filters

for a specific efficiency. Experiments with a variable layer number will also provide more insight into the efficiency of mist filters, for more layers increase the contribution of the channels, whereas the film efficiency remains constant.

Experiments will be conducted with various grades of both wettable and non-wettable filter media. The effect of re-entrainment will be minimized using relatively low-efficient filters. Here, the primary penetration is expected to outweigh the secondary generation of droplets by bursting bubbles. On basis of additional experiments with more efficient filter media, it will also be discussed to what extent re-entrainment is responsible for different results in published works and how it limits the proposed model and the overall efficiency of mist filters.

Chapter 9 aims to answer the fundamental question which arises from a very slow increase of Δp beyond the onset of drainage: How steady is the "steady state" of mist filters? At first, it will be investigated whether this slow Δp-creep during *continuous* operation can be accelerated by higher oil loading rates or filter face velocities. Long-term experiments will then be conducted at accelerated conditions with various grades of initially dry and wettable glass microfiber media. The endpoint of the creep will also be compared to the steady-state Δp of pre-saturated filters at the same operating conditions. Photographic images will be used to reveal common ground between liquid distribution patterns of the two apparently different starting conditions. Further analyses between the onset of drainage, commonly assumed as the steady state, and the endpoint of the Δp creep will show if the liquid distribution is subject to changes during the creep.

A completely different but more applied kind of unsteady operation is addressed by *discontinuous* experiments. Flow interruptions are not only the most common type of discontinuous operation in practive, but also known to cause a higher pressure drop when filtration resumes. Experiments with well-defined flow interruptions, such as a predetermined loading period and duty cycle, may show if this phenomenon can be linked to the same underlying mechanisms as during a continuous Δp-creep. Additional experiments with intermittently changing face velocities (as another type of discontinuous operation) will show if any excess liquid can be fully drained when returning to a previous point of operation. This will reveal if such discontinuously achieved steady states can be compared to their continuous counterparts. Chapter 9 will therefore help understanding if, or to what extent, the steady states of mist filters are subject to some kind of (ir-)reversibility.

Chapter 10 investigates the reliability and accuracy of capillary flow porometry for the characterization of structure and wettability of mist filter media. In

general, structure and wettability are closely interconnected and therefore pose a limitation to detailed (and independent) investigations, as it is not possible to vary one variable (e.g. structure) while maintaining the other (wettability) constant. Capillary flow porometry does not only account for both structural and surface properties, but is also routinely used to evaluate the bubble point. Despite its long record of history and a wide-spread use, capillary flow porometry is subject to considerable inaccuracies for commonly used wetting liquids and changes of the modus operandi. The objective of Chapter 10 is therefore not to apply capillary flow porometry for the characterization of a wide variety of glass microfiber media, but rather to characterize and possibly resolve major accuracy issues of this method.

Experiments in Chapter 10 will be limited to a representative type of glass microfiber media. In order to minimize deviations between samples, the filter medium will be taken from a single batch and chosen according to its repeatability. At first, volatility of wetting liquids will be investigated with a selection of commercially available fluorocarbons as the prevalent type of liquid as well as a silicone oil which is less commonly used. Evaporation rates of the different wetting liquids will be evaluated by means of the weight loss of initially saturated samples of filter medium. The samples will also be subject to a dry air flow streaming through them. This corresponds not only to the same operating principle as capillary flow porometry but might also accelerate the evaporation of the low volatile liquids. A subset of silicone oils with variable viscosities (but a more or less constant surface tension) will allow furthermore to investigate the speculations of Yunoki et al. (2004) on the role of viscosity.

In order to make experiments independent of technical details, such as the sample area, the flow direction, and proprietary software routines, it is necessary to realize an in-house porometer prototype with full access to control all operational parameters. In principle, capillary flow porometers are scanning either Δp while simultaneously controlling the air flow across a wet and a dry sample, or vice versa. By varying one variable while keeping the others constant it will be investigated to what extent changing parameter settings will affect the resulting pore size distributions. These investigations will cover simple adjustments such as the order of the wet and the dry scan, but also more fundamental changes like the controlled variable (i.e. Δp vs. air flow) of the porometer set-up. Extending the scan duration with the different wetting liquids might also lead to a premature evaporation and an impact on the experimental outcome. Apart from revealing parameters influencing the accuracy of capillary flow porometry, the objective of this chapter is also to provide recommendations for precise and feasible measurements of this technique.

6

Impact of face velocity and oil loading rate on $\triangle$p during continuous filtration[1]

Abstract

The dependence of the differential pressure drop Δp and the level of internal oil saturation S on the flow velocity of the air were investigated experimentally for a typical oil mist filter composed of oleophilic glass microfiber layers. Over a wide range of filter face velocities (v=5 to 70 cm/s) and liquid loading rates (R=15 to 125 mg/(m^{2}s)), and within the accuracy of the measurements, the "wet" pressure drop of the filter $\Delta p - \Delta p_0$ (i.e. the increase in Δp over the "dry" pressure drop Δp_0) was constant, and did not show a systematic dependence on v. When decomposing the wet pressure drop into its components Δp_{jump} and $\Delta p_{channel}$, the jump was also independent of the oil loading rate. The level of internal liquid saturation S was inversely proportional to v, with an empirical fit function $S=1/(1+v/v^*)$. The characteristic velocity v^* was found to depend on the oil loading rate, and presumably also depends on the media structure which was not varied here. This filter behavior is consistent with the

[1] This article was published as: Kolb, H. E., J. Meyer and G. Kasper (2017). *Flow velocity dependence of the pressure drop of oil mist filters*, Chemical Engineering Science 166, 107–114.

"Jump-and-Channel-Model" proposed recently by Kampa et al. (2014).

The experiments further showed that the "steady-state" pressure drop under constant filter operating conditions underwent a gradual increase with time (termed "Δp-creep") that depends on operating conditions. This Δp-creep diminishes gradually and was found to become stronger with increasing loading rate and filter face velocity. At the highest rate of increase (i.e. v=70 cm/s, R=125 mg/(m^{2}s), an experiment lasting for 1100 hours did not suffice to attain an asymptotic level for Δp. Creep was found to be associated with a gradual increase in saturation and must therefore be classified as an(other) instability phenomenon in oil mist filters.

Keywords: Filtration, coalescence filter, oil mist, pressure drop

6.1 Introduction

Aerosols consisting of submicron oil droplets ("oil mist") are an undesirable by-product of widely used industrial processes such as metal cutting, engine crankcase ventilation, or the operation of oil lubricated gas compressors. One commonly practiced way to capture and remove this oil mist is by filtration with glass microfiber or other high-efficiency media. The differential pressure of such filters increases very substantially prior to steady-state operation due to loading with coalesced oil. In order to achieve and sustain steady-state operation, this oil has to be moved by the airflow to the rear of the filter, where it can drain. Maintaining this flow of coalesced liquid requires an additional Δp above and beyond the initial Δp_0.

The basic mechanisms involved in transporting the liquid and their respective contributions to the overall Δp of a filter have recently been described by (Kampa et al., 2014, 2015) in the form of a "Jump-and-Channel-Model". According to this model, the overall Δp of an oleophilic oil mist filter is composed of two components, an internal contribution needed to "pump" liquid through the media – typically in distinct channel-like structures, hence denoted as "$\Delta p_{channel}$" – plus a final, rather steep "Δp_{jump}" required to overcome capillary retention forces in order to push the liquid out of the media and cause it to drain as a thin film along the outer surface. (We make the common assumption that the filter is installed vertically to facilitate drainage.)

According to the model, each of these two Δp components depends in a characteristic way on key filter operating parameters such as air velocity (suitably expressed in terms of filter face velocity v), liquid loading rate R, and

the level of internal saturation with liquid S: The $\Delta p_{channel}$ (strictly speaking the excess channel-Δp after subtracting Δp_0) should mainly be a function of loading rate. It should not depend on the air velocity v however, because the system reacts to changes in v by adjusting the liquid saturation level so as to maintain the constant excess channel-Δp needed to pump the liquid. Δp_{jump} should be independent of both liquid loading rate and air velocity, because it is determined primarily by capillary properties of the filter media in combination with the liquid, i.e. by pore structure and surface tension. As a practical consequence, the sum of Δp_{jump} and excess channel-Δp of an oil mist filter in steady operation at a constant loading rate should not depend on the volumetric flow of air, a behavior that is not intuitively obvious in the realm of flow through porous media.

The objective of the current paper is to provide experimental verification and validation for these relationships, and in particular for the flow rate (in-)dependence. The experiments were performed over a broad range of filtration velocities and aerosol loading rates, with a combination of oleophilic glass microfiber medium and oil typically used in air compressors. Filter differential pressures, saturation levels and internal oil distributions were measured and compared to the model predictions.

6.2 Experimental materials and methods

Aerosol generation: Oil mist was generated by a Collison-type nebulizer (May, 1973) in which dry compressed air disperses a typical compressor oil (surface tension 31 mN/m, dynamic viscosity 122 mPa s) at room temperature. SMPS measurements revealed droplet sizes of a log-normal distribution with a mean diameter of about 640 nm and a geometric standard deviation of 1.9. A schematic diagram of the experimental set-up is given in Fig. 6.1. The rate of oil mass generation was kept constant for a given experiment by maintaining a constant Δp across the nebulizer. Further downstream this aerosol was mixed with a dry make-up flow to adjust the velocity to a desired level. Temperature and absolute pressure upstream of the filter were monitored continuously in order to compensate the effect of increasing pressure on the face velocity by the mass flow controller. The actual oil loading rate of the filter was determined from the oil drainage rate which was measured continuously on line. Aerosol penetration and oil re-entrainment were neglected in this calculation because the filters had overall efficiencies above 99.99% and entrainment was insignificant compared to the loading rate (Wurster et al., 2015).

Filter materials: The filters used is this study were built as flat “sandwiches”

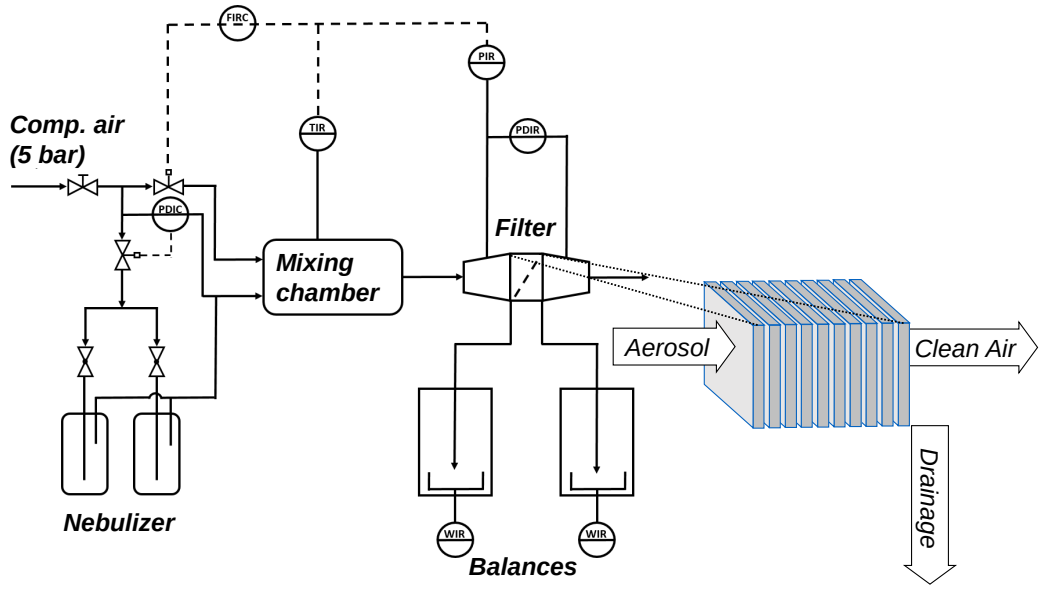

Figure 6.1: Schematic diagram of the experimental set-up consisting of Δp-controlled nebulizer, a temperature and absolute pressure corrected make-up flow by a mass flow controller, a holder for mounting the sandwiches of single layers, as well as two balances to record wall flow and drainage

consisting of 10 layers each of the same oleophilic glass microfiber media (thickness about 0.5 mm, porosity 95%, mean pore size 9.1 µm) with a metal grid as downstream support. The filter samples were cut from a roll of commercial filter material manufactured by Hollingsworth & Vose. The inhomogeneity of these media was significant across the roll, as evidenced by variations in dry pressure drop of up to 30% between coupons. This was compensated to some degree by selecting sandwiches with variations of less than 10% in Δp_0. The sandwich with an effective filtration area of 8 cm x 8 cm was clamped into a metal frame and installed vertically in the filter unit.

Experimental procedures: Each experiment started with a fresh, dry sandwich that was loaded under exactly constant conditions for several hours past reaching steady-state operation. (For oil mist filters, steady state is commonly defined as operation at a constant drainage rate and pressure drop. Note however, that some filter media under certain operating conditions exhibited a kind of "Δp-creep", which will be addressed later in this paper.) At the end of a run, the sandwich was immediately taken apart to photograph each layer for the purpose of image analysis of the oil channel distribution, and/or to measure the oil content gravimetrically. The mean saturation per layer was determined from the weight increase after removing about 5 mm around the edges where the media had been clamped in the filter mount. Photographs were converted to black and white images via a pre-determined threshold of gray

level, and evaluated by automated image analysis for the local oil distribution, especially the size and number of oil channels. The gray level threshold was determined in such a manner that the gravimetrically measured saturation matched the area-equivalent saturation of the image analysis. (This assumes implicitly, that a given region of the filter is either fully saturated or completely dry. Consequences are discussed later.)

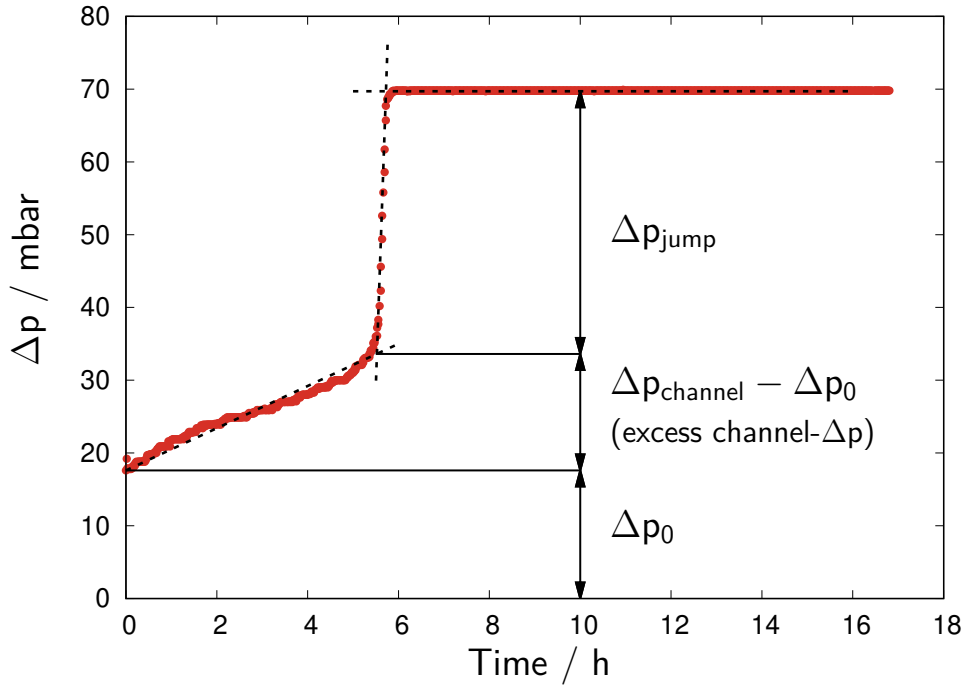

Figure 6.2: Graphical method to determine the characteristic pressure drop components channel-Δp and Δp-jump.

Data evaluation: The pressure drop components $\Delta p_{channel}$ and Δp_{jump} were obtained from the temporal evolution of the overall Δp during the start-up phase of a filter by a graphical method first suggested by Kampa et al. (2014), as illustrated in Fig. 6.2. For the case of an oleophilic filter, one divides the Δp-curve into three quasi-linear sections. The first section is due to the formation of oil channels. The slope of this $\Delta p_{channel}$ region is usually quite modest when compared to the following, steep increase (the jump) caused by the formation of an oil film on the rear face of the filter. This film, which is quasi-continuous and maintained on the surface by the gas flow, acts as the drainage flow. The last section of the Δp-curve is what we call steady state, i.e. with constant drainage, a constant internal oil distribution, and (in principle) with no further changes in Δp. The linearized slopes for $\Delta p_{channel}$ and Δp_{jump} are obtained from the intersections of the respective tangents as indicated in Fig. 6.2.

6.3 Results and discussion

6.3.1 Dependence of Δp on operating parameters

Experiments were carried out for face velocities of 5, 10, 25, 40 and 70 cm/s at nominal oil loading rates of 15, 60 and 125 mg/(m^{2}s), giving a set of 15 parameter combinations, not counting repeated runs. A representative set of data for a fixed velocity of 25 cm/s is shown in Fig. 6.3. The three curves in Fig. 6.3a (Δp vs. time) each show the respective channel sections of the Δp increase, followed by a steep Δp jump. As expected from the Jump-and-Channel-Model, the height of Δp_{jump} appears to remain constant, while the respective transition point between $\Delta p_{channel}$ and Δp_{jump} is reached more rapidly with increasing loading rate. When plotting the same curves against loading rate (rather than against time) as shown in Fig. 6.3b, one would expect them to "collapse" into a single curve. However, upon closer inspection one finds that this is not quite the case. The transition points between channel and film formation shift with oil loading rate, both toward higher Δp and toward higher mass loadings. In other words the section of $\Delta p_{channel}$ becomes steeper with oil loading rate, and the transition occurs later. In order to make the differences more visible, the respective section of Fig. 6.3b is enlarged in Fig. 6.3c, where the transition points between channel region and jump are marked by circles.

These effects can be explained readily with what we know from the Jump-and-Channel-Model: For one, higher oil loading rates mean that more oil has to be "pumped" through the filter per unit time, and this requires a higher $\Delta p_{channel}$, hence a steeper curve. Secondly, higher oil loading rates entail a higher mean saturation in the channel region, hence more "time" to reach that saturation level and consequently a shift toward higher mass loading. (Saturation will be discussed later in the paper in more detail.)

A comprehensive view of the entire data set is shown in Fig. 6.4 where the pressure drop components are plotted separately against air velocity v. Δp_{jump} is indeed very constant across all combinations of operating parameters. In particular no systematic dependence on loading rate or filtration velocity can be observed within the accuracy and reproducibility of our experiments. For the excess channel-Δp ($\Delta p_{channel} - \Delta p_0$) the influence of operating parameters is a little less obvious from Fig. 6.4, because these data are noisier due to reasons addressed below. However the regression lines of all oil loading rates exibit no systematic variation of excess channel-Δp with flow velocity. Within their error range the excess channel-Δp can be approximated as horizontal lines and increase only with oil loading rate as expected.

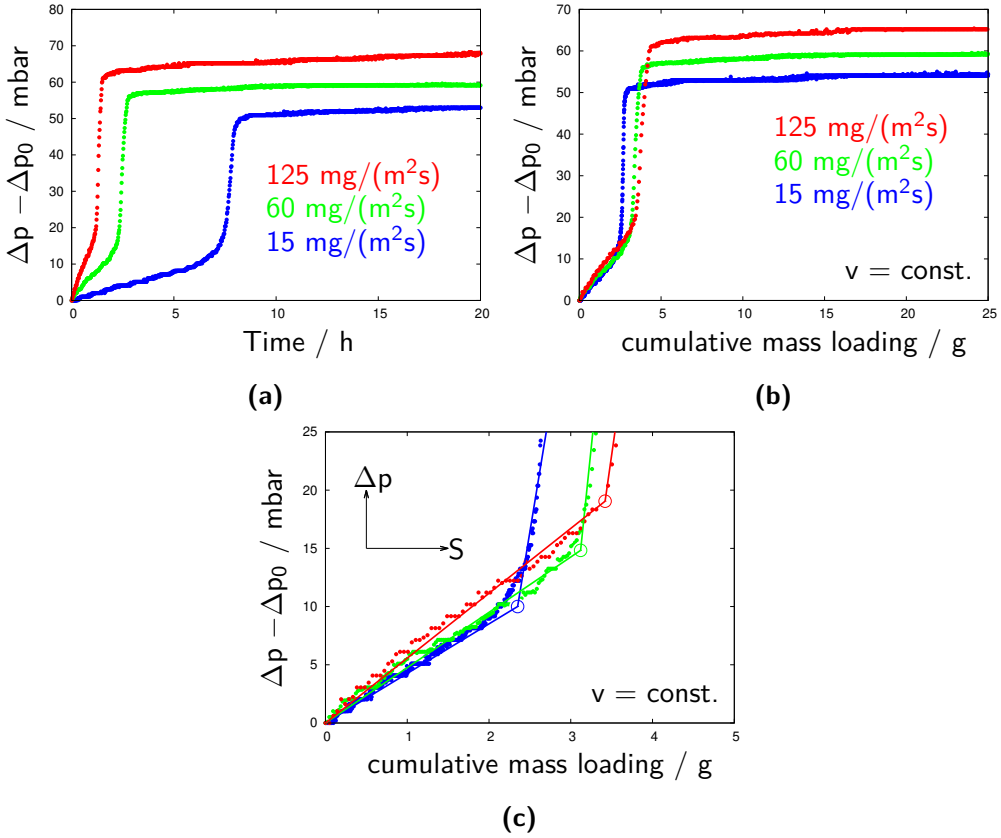

Figure 6.3: Δp vs. time (Fig. 6.3a) and vs. mass loading (Fig. 6.3b) for a fixed filter face velocity of 25 cm/s. Fig. 6.3c is an enlargement of the $\Delta p_{channel}$ region from Fig. 6.3b to explain why curves do not collapse. Circles indicate the approximate transition point from $\Delta p_{channel}$ to Δp_{jump}.

The absolute level of the $\Delta p_{channel}$ data is much lower than the level of the Δp jumps (about 10 mbar vs. 45 mbar) and therefore more susceptible to errors from various sources. These include the accuracy of the pressure transducer (±1 mbar) and the graphical evaluation method (±1 mbar). The actual oil loading rate could also differ from the nominal loading rate by about ±5 mg/(m²s). These errors amount to a total uncertainty of about 10 to 30% in excess channel-Δp. In addition, the inhomogeneity of the filter media (briefly discussed in Section 6.2) is a likely contributor to systematic variations in oil channel structure and $\Delta p_{channel}$ between sandwiches, which are difficult to gauge, however.

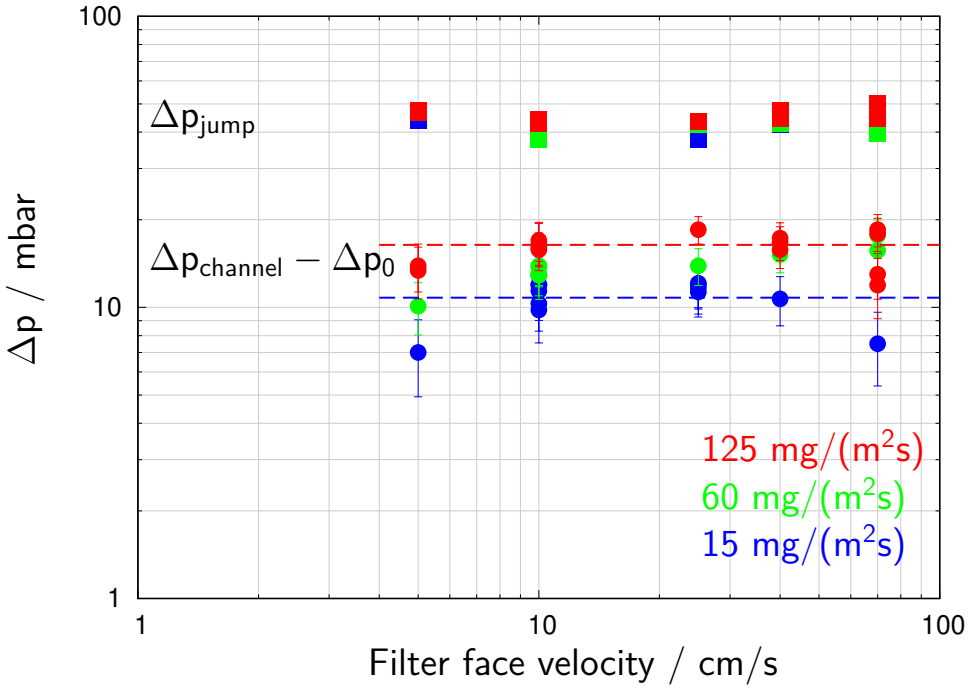

Figure 6.4: Δp_{jump} and excess channel-Δp vs. airflow velocity for different oil loading rates. The excess channel-Δp is always based on 10 filter layers.

6.3.2 Dependence of global saturation level and internal oil distribution on air velocity and other parameters

The dependence of $\Delta p_{channel}$ on air velocity v and oil loading rate R has immediate consequences for the liquid saturation level S as a function of these parameters. Specifically, one expects the saturation level to decrease with increasing filter face velocity v, if the excess channel-Δp is to remain constant. On the other hand, the saturation will of course depend on oil loading rate R. While the dependence of S on R was verified in earlier work (Kampa et al., 2015) the dependence on v has not been investigated systematically.

For mist filters, the saturation level S is often expressed as a global average for the entire sandwich (Liew and Conder, 1985; Frising et al., 2005; Mead-Hunter et al., 2013), based on a measurement of the weight of oil contained in the filter after the flow has been shut off. One has to keep in mind however, that the last layer of an oleophilic multi-layer filter sandwich needs to be excluded from the measurement because it contains additional oil due to the collapse of the drainage film when shutting off the flow (Kampa et al., 2015). We have therefore derived S from the weight gain of layers 1 to 9. Typical layer-by-layer saturation profiles can be found later on in Fig. 6.11.

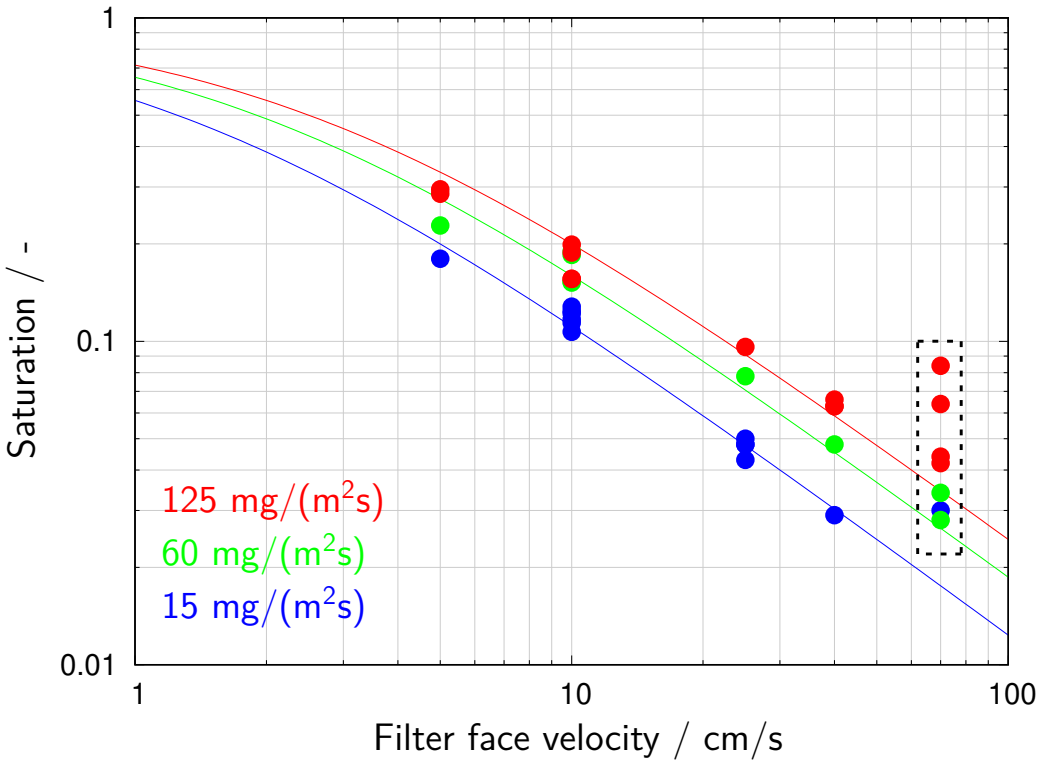

Figure 6.5: "Internal" saturation vs. airflow velocity for different oil loading rates. Curves are calculated using the model Eq. 6.1 and Tab. 6.1. Dotted frame shows data affected significantly by Δp-creep.

Fig. 6.5 shows these global saturation values as a function of operating parameters v and R. As expected, the saturation increases systematically with oil loading rate but generally decreases with air velocity. (The up-swing of the data points at 70 cm/s is due to another effect, namely Δp-creep, which will be addressed later.) Both the dependencies on R and v are logical consequences of the Jump-and-Channel-Model, and indicate that the excess channel-Δp (of a given medium and oil) depends only on the amount of oil to be pumped through the filter but not on the flow velocity. Higher oil loading rates thus require more pressure drop. This additional Δp must be generated inside the filter, either by increasing the saturation (in case of constant v), or by increasing v. In case of a constant loading rate, the saturation thus goes down as the flow velocity goes up.

In Fig. 6.5 the saturation level S appears to be inversely proportional to v, reminiscent of the relationship between capillary rise and pressure head in a system of liquid filled capillaries being "de-watered". (The analogy is helpful despite significant differences between these two types of systems, including the fact that oil channels are not continuously filled with liquid.) Such an

inverse relationship was already observed in earlier work (Mead-Hunter et al., 2013) based on measurements with glass microfiber media similar to ours. Unfortunately, a direct comparison of absolute saturation values was not possible due to differences in experimental procedure. However, one can test the functional form of the dependence.

A functional form S∼1/v fits quite well to the mid range of saturations in Fig. 6.5. It would not work for very low flow velocities however, because S must be bounded by 0 and 1 in the extremes. A more suitable functional behavior can be obtained with the empirical expression

$$S = \frac{1}{1 + \frac{v}{v^*}} \tag{6.1}$$

where v^* is a characteristic velocity that depends on the oil loading rate and presumably also on the media structure (which was not varied here). v^* was determined for each loading rate by fitting the above expression to our data (Tab. 6.1).

Oil loading rate mg/(m²s)	v^* cm/s
15	1.25
60	1.90
125	2.50

Table 6.1: Characteristic velocities according to Eq. 6.1 for different oil loading rates.

The global saturation does not take into account the internal oil distribution, neither in the direction of the air flow nor within the plane of the filter, and in particular not the existence of oil channels. Nevertheless it remains an indispensable parameter to describe the state of operation of mist filters, last but not least because it can be determined accurately and with relative ease. The oil channel geometry within the filter plane (which is of great interest because it determines the pressure drop) is quite difficult to determine experimentally in oleophilic media, because the channel boundaries are not very sharply defined. We have evaluated photographs of the individual filter layers by image analysis as described in Section 6.2, to obtain values for the mean channel diameter and the channel number density as a function of filter operating parameters (Fig. 6.7). This analysis assumes that oil channels are fully saturated in an otherwise dry filter. This premise is much better fulfilled for oleophobic than for oleophilic media. The visual appearance of our filter layers at the end of an experiment suggests in fact, that some regions within the filter are partially wetted, perhaps because oil transport within the channels occurs discontinuously, drop by drop. In order to determine the exact channels boundaries we have

therefore used the gravimetrically determined global saturation S as a reference in setting the contrast threshold for image analysis. An overlay of a photograph and the evaluated channel boundaries is given in Fig. 6.6.

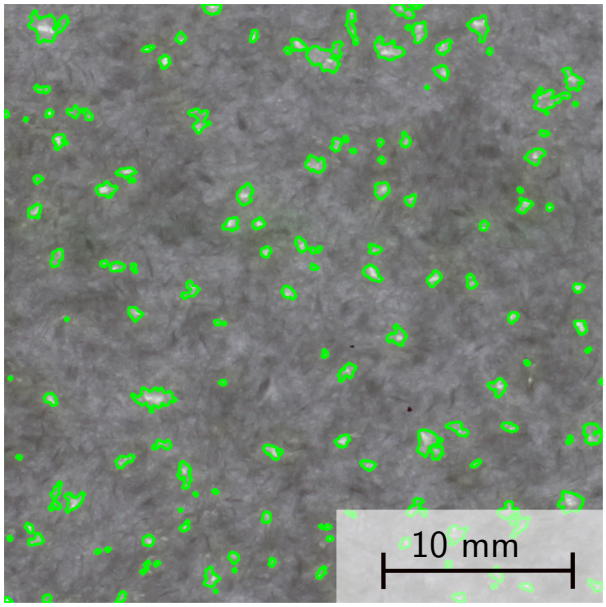

Figure 6.6: Photograph of Layer 8 with the channel boundaries (green) for a velocity of 40 cm/s and loading rate of 125 mg/(m^{2}s).

Despite considerable experimental noise and uncertainty in these data, the results are worth reporting because Fig. 6.7 gives an indication of how the oil distribution pattern reacts to changes in operating conditions. With increasing air velocity (at a fixed oil loading rate) the oil channels tend to decrease in size rather than number in order to achieve the S$\sim$1/v dependence in global saturation. On the other hand, the preferential system response to an increase in oil loading rate seems to be via the number of channels. The exact reasons for this behavior are still not fully understood. Nor are the current data reliable enough to draw further reaching conclusions.

6.3.3 Relationship between the oil distribution and Δp

There are two conceivable limiting cases for the oil distribution pattern in a filter layer. Oil can be distributed either in a perfectly random and microscopically homogenous pattern (with no oil channel structure at all), or as larger oily regions interspersed in an otherwise dry medium, with a direct impact on the dependence of Δp on S. If we assume that oil flows in fully saturated channels whereas the air flows in completely dry regions, then the wet Δp in the channel region is related to the dry Δp_0 simply via an increase in internal flow velocity:

$$\frac{\Delta p_{\text{channel}}}{\Delta p_0} = \frac{1}{(1 - S)} \tag{6.2}$$

In the other limit of a perfectly homogeneous and random oil distribution, liquid may be envisioned as being distributed on all the fibers as a uniform film. The rise in Δp with S would then be due to an increase in effective fiber diameter as well as a loss of open pore space. One can then model the increase in Δp by one of several well-known expressions for the pressure drop of porous media. A suitable expression was derived in the Appendix (at the end of this chapter), according to which

$$\frac{\Delta p_{channel}}{\Delta p_0} = \frac{1}{(1-S)^{4.55}} \tag{6.3}$$

Fig. 6.8 compares these two theoretical limiting cases with the experimental values of $\Delta p_{channel}/\Delta p_0$. The functional dependence S(v) required in Eqs. 6.2 and 6.3 was calculated using Eq. 6.1 and Tab. 6.1. As expected, the measurements lie between the two limiting cases, because the actual oil distribution inside the filters is neither perfectly homogenous nor "black and white". Nevertheless the model expressions provide an upper and a lower bound for the range of possible Δp. It also becomes clear from the figure that the formation of oil channels contributes significantly to the reduction of the overall Δp and is therefore more advantageous energetically.

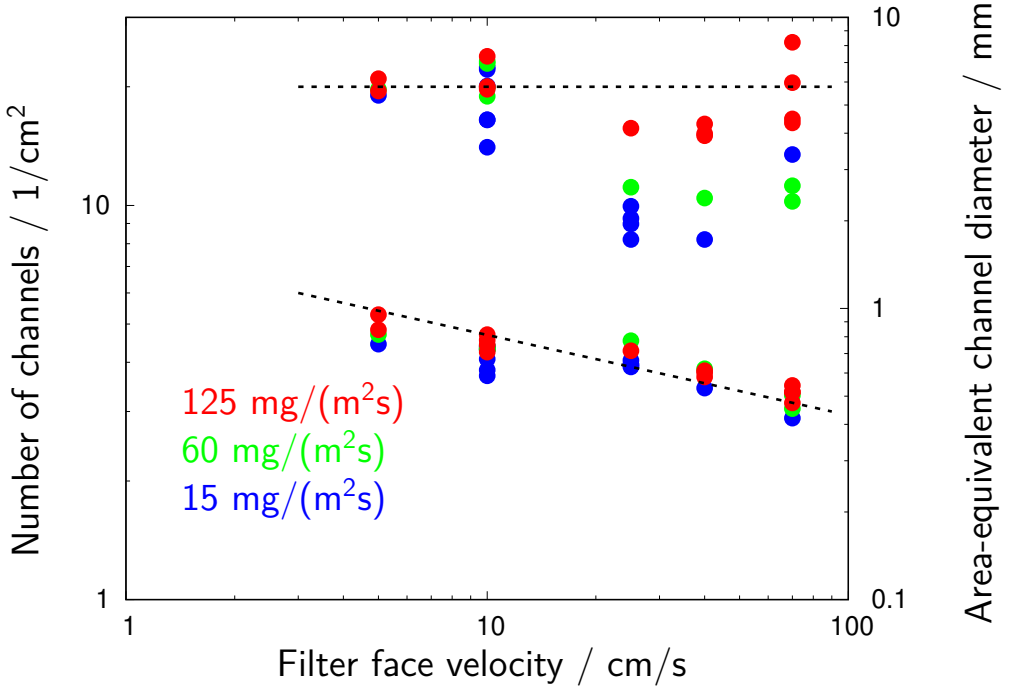

Figure 6.7: Channel number and diameter vs. airflow velocity for different oil loading rates. The dotted lines are merely a guide to the eye.

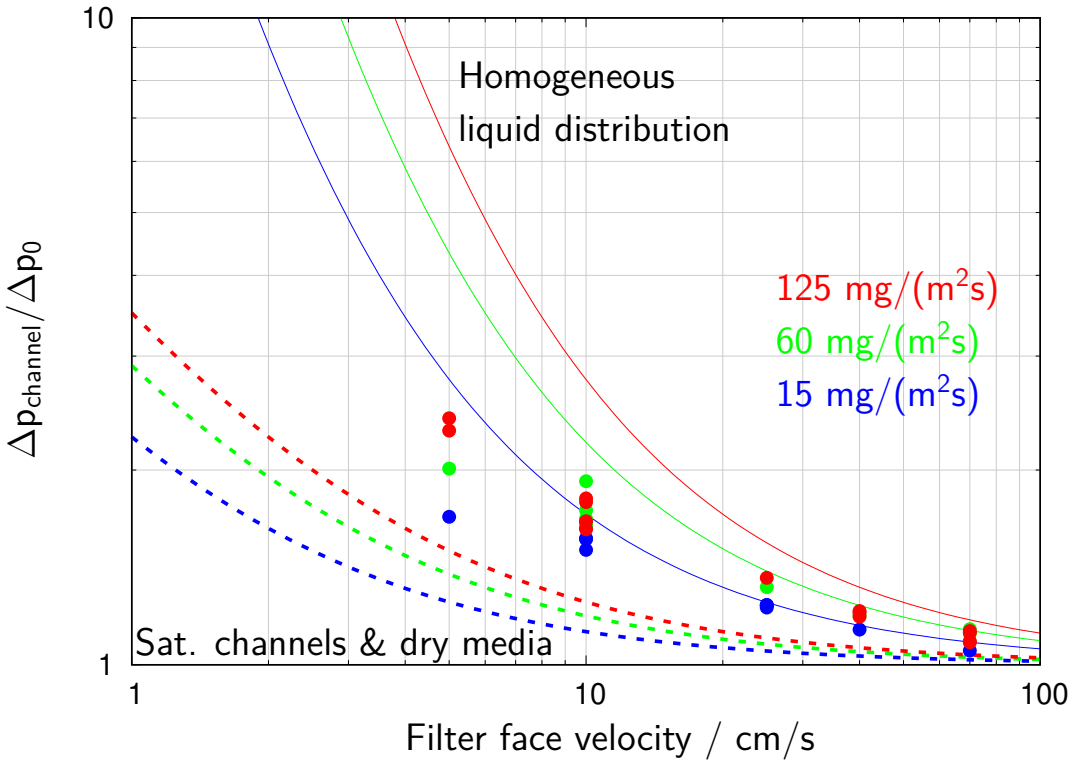

Figure 6.8: Relative increase of $\Delta p_{channel}$ with airflow velocity: Comparison of measurements with theoretical limiting cases of internal liquid distributions Eq. 6.2 and 6.3.

6.3.4 Steady state Δp and Δp-creep

It is generally assumed that once an oil mist filter reaches steady state with regard to oil loading and drainage, the differential pressure also becomes constant. This assumption is inherent in most work published to date on the subject (e.g. Frising et al., 2005; Gac, 2015; Mead-Hunter et al., 2013; Kampa et al., 2015) and implies a constant oil distribution within the filter and thus also a constant global saturation. Such an assumption usually appears justified when operating filters for short periods of time under perfectly constant conditions. In experimental reality however, we have found many cases where Δp is not flat, but tends to increase systematically with time, although often very slowly – hence the term "creep" – even though the operating conditions are kept meticulously constant throughout the run and the drainage equals the oil loading rate.

In this quasi-steady state, some of our data and media show a Δp increase of no more than 2% after the onset of drainage and within a total loading time of 20 hours (the duration of most experiments reported in this paper), while in other

experiments the increase is much more substantial. Fig. 6.9a illustrates this creeping behavior with a typical data set comprising measurements at different airflow velocities but fixed loading rate. Typically, experiments at higher airflow velocities appear to be more prone to Δp creep than at smaller velocities, where the change in Δp is almost imperceptible during 20 h of observation.

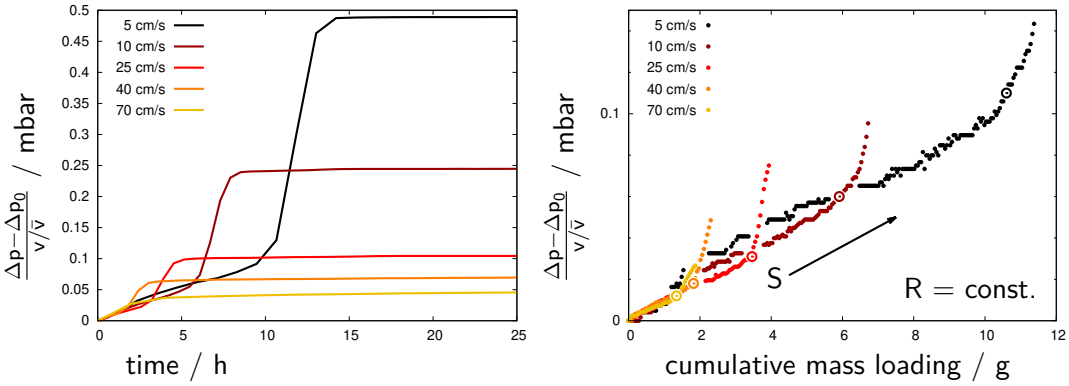

Figure 6.9: Δp at constant-loading-rate data (125 mg/(m²s)) and variable face velocity vs. time (Fig. 6.9a) and vs. cumulative deposited mass (Fig. 6.9b). Fig. 6.9b shows the enlarged channel region of Fig. 6.9a. The Δp-jump was truncated for better readability. Note that the transition points (circles) are all on the same slope, but shifted toward higher mass loadings at lower face velocities.

A second aspect concerning the flow rate dependence of the Δp of oil mist filters is discussed in Fig. 6.9b, where the Δp increase vs. time from Fig. 6.9a is now represented vs. cumulative mass load, and Δp is normalized by v to account for carrying flow rates. Fig. 6.9b shows only the channel region of the Δp curves, while the jump has been truncated for better readability. (Δp_{jump} is not a function of velocity as we have seen.) Since these curves were all obtained at the same oil loading rate, the individual slopes for $\Delta p_{channel}$ are practically the same, at least within the accuracy and reproducibility of these experiments. On the other hand, the transition points (circles) from channel region to Δp_{jump} are shifted systematically with v toward lower mass loading. The explanation follows from the Jump-and-Channel-Model, which predicts lower saturation levels at higher flow velocities. The transition is therefore reached more rapidly, i.e. at lower oil loads. Note further that Fig. 6.9b corroborates our earlier findings regarding the dependence of S on v (Fig. 6.5 and Eq. 6.1) from a different angle.

In order to investigate the long-term behavior of this creep phenomenon, an 1100-hour experiment (Fig. 6.10) was performed with comparable operating conditions as the highest velocity in Fig. 6.9. Note that the creep is not linear. Nor is an asymptotical value of Δp reached during roughly 45 days of operation,

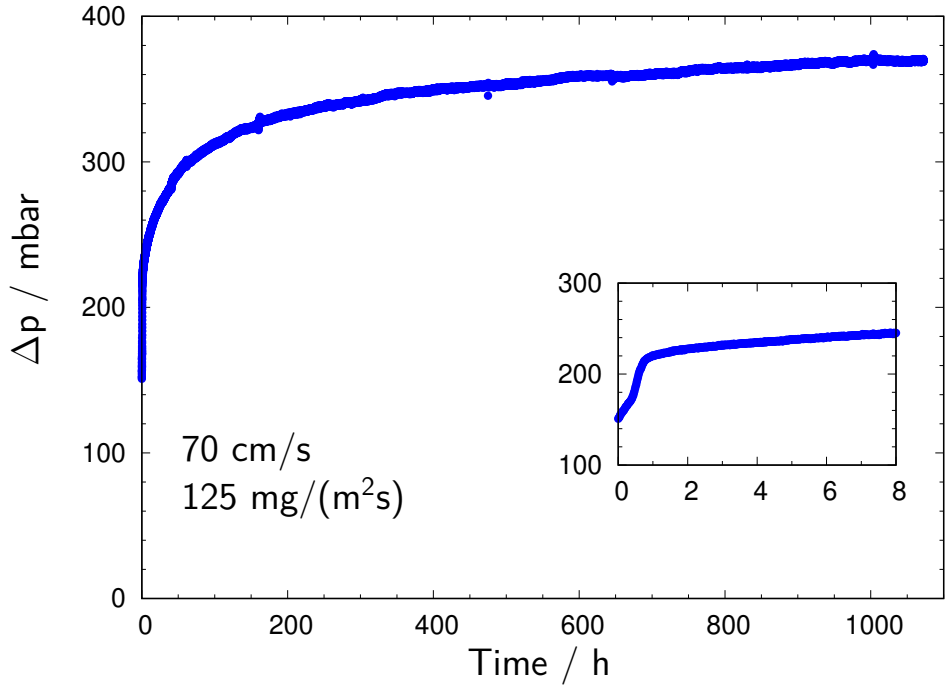

Figure 6.10: Long-term observation of Δp for a constant airflow velocity of 70 cm/s and constant oil loading rate of 125 mg/(m^{2}s). The inset magnifies the first 8 h of operation.

although such an asymptotic value must exist. One notices however, that the increments of Δp are becoming smaller with time. Creep may therefore follow a behavior of the type

$$\Delta \mathrm{p} = \Delta \mathrm{p}_{\infty}(1 - e^{-\frac{t}{\tau}}) \tag{6.4}$$

wherein τ is a characteristic time that will depend on operating conditions and media structure. Values for τ and $\Delta \mathrm{p}_{\infty}$ could be computed with regression analysis. For a validation of this approach, however, experimental data for τ as well as a specific value for $\Delta \mathrm{p}_{\infty}$ are needed.

Associated with the rise in Δp during the 1100-hour experiment was a gradual increase in saturation levels throughout the sandwich. This can be seen in Fig. 6.11 from a series of measurements of the oil distribution, starting a few minutes after the begin of filter loading, and then at intervals of 0.25 h, 0.4 h, 1 h, 4 h, 70 h, and finally after 1100 h. The black data points in this figure indicate the onset of drainage and the transition from $\Delta \mathrm{p}_{\mathrm{jump}}$ to what is normally considered "steady state". The contribution of experimental artifacts to the very slow accumulation of oil was excluded by additional experiments. Wall flow of oil and possible coarse secondary aerosol due to the blow-off in the tubing at higher filter face velocities were eliminated in a trap prior to the filter.

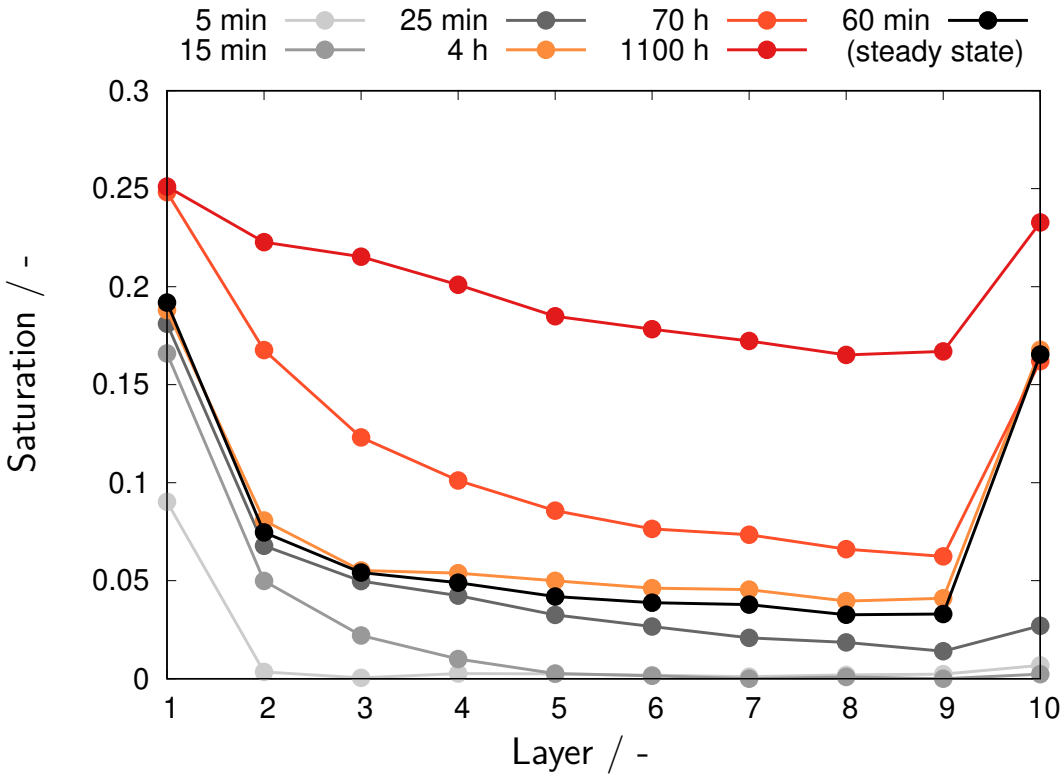

Figure 6.11: Temporal evolution of saturation for a constant airflow velocity of 70 cm/s and constant oil loading rate of 125 mg/(m^{2}s).

Indications for this Δp-creep can actually be found in the literature, including some of the papers cited earlier, but the phenomenon has never been acknowledged or discussed explicitly in the literature, so far. As a first consequence of our observations, the distinction between steady and non-steady state no longer seems adequate for this mode of filter operation. Instead, we suggest to describe this state as either metastable or non-stable, or perhaps as quasi-stable when the changes are very slow. This is supported also by the observation that the saturation is not stable over time.

As a final note, the creep phenomenon we describe is not to be confused with another type of metastability in oil mist filters called “pseudo-stationary state”. That term was first coined by Frising et al. (2005) to describe the apparent rearrangement of the internal oil distribution due to strong disturbances in filter operation such as an interruption or change of flow rate, which entails a new state at a higher Δp level after each disturbance (see also Mead-Hunter et al., 2013). In our case all operation parameters were constant throughout the entire experiment.

6.4 Summary and conclusions

The dependence of the differential pressure drop and the level of internal oil saturation S of an oil mist filter on the flow velocity of the air were investigated experimentally. The experiments were carried out with compressor oil on a typical oleophilic glass microfiber medium across a representative range of filter face velocities (v=5 to 70 cm/s) and liquid loading rates (R=15 to 125 mg/(m^{2}s)). The data were compared to a recent model by Kampa et al. (2014) which predicts that the Δp due to the filtration of oil (Δp-Δp_0, or in other words the sum of Δp_{jump} and excess channel-Δp) should be independent of v. Rather than leading to an increase of these pressure drop components, any increase in v is compensated by adjusting downward the level of internal saturation S.

Δp_{jump} and $\Delta p_{channel}$ were determined according to the model for 15 different combinations of these operating conditions and analyzed primarily for their dependence on v and R. Data for the global saturation level S as well as for the distribution of oil across individual filter layers were also collected for these conditions. Within the accuracy of the measurements, neither the excess channel-Δp nor Δp_{jump} were found to depend in a systematic way on the flow velocity; and thus also not the Δp due to the filtration of oil.

Based on the experimental data, an empirical model expression (Eq. 6.1) was developed for the dependence of S, the average level of the internal saturation of the filter with oil, on v:

$$S = \frac{1}{1 + \frac{v}{v^*}}$$

wherein v^* is a characteristic velocity that must be determined experimentally. v^* was found to depend on the oil loading rate, and presumably also depends on the media structure which was not varied here.

The experiments also showed that the so-called steady state mode of filter operation is often quasi-steady at best. Under certain constant operating conditions, Δp underwent a further, gradual increase with time at a rate that was much slower than during the start-up phase of the filter, but not negligible in the long run. This "Δp-creep" was found to become stronger with loading rate and filter face velocity. The observed increase ranged from about 2% to some 40% per day. At the highest rate of increase, an experiment lasting for 1100 h did not suffice to attain an asymptotic level for Δp. Creep was found to be associated with a gradual increase in saturation. It must therefore be

classified as an(other) instability phenomenon in oil mist filters, which may have a common cause with the pseudo-stationary state, a rearrangement of the internal oil distribution due to disturbances in filter operation (Frising et al., 2005). The role of media properties in these processes remains to be clarified and is currently under investigation.

Appendix: Derivation of Eq. 6.3

Eq. 6.3 is based on the empirical model by Molerus et al. (1971) for flow through porous systems, which was derived from experiments with packed beds of glass beads in a wide range of porosities between 0.3 and 0.75:

$$\Delta p = 22.4 \frac{1-\varepsilon}{\varepsilon^{4.55}} \left(\frac{1}{d_f}\right)^2 \mu v_0 H \tag{6.5}$$

with fluid properties μ and v_0, filter thickness H, porosity ε, and fiber diameter d_f. In the terminology of our paper, Δp, the "internal pressure drop" of the filter, it is in fact equal to $\Delta p_{channel}$. Although less known than other, similar expressions, the mathematical form of its void function term allows to express the relative change of internal pressure drop solely as a function of the global saturation. Moreover, it gives values that lie between those of Carman and Kozeny (1956) and Davies (1973) for the porosity range of interest to us.

For an oil mist filter in operation, the porosity ε and the fiber diameter d_f will change relative to the dry media, resulting in the following increase in Δp (i.e. $\Delta p_{channel}$):

$$\frac{\Delta p}{\Delta p_0} = \frac{1-\varepsilon_{wet}}{1-\varepsilon_0} \left(\frac{\varepsilon_0}{\varepsilon_{wet}}\right)^{4.55} \left(\frac{d_{f,0}}{d_{wet}}\right)^2 \tag{6.6}$$

The increase in fiber diameter, d_f/d_{wet} can be estimated if we calculate the total length L of all fibers in the filter from the total fiber volume in the filter, $(1-\varepsilon_0)V_{filter}$,

$$(1-\varepsilon_0)V_{filter} = \frac{\pi}{4}(d_{f,0})^2 L \tag{6.7}$$

and assume that the accumulated oil is distributed uniformly over the surface of all fibers

$$(1-\varepsilon_{wet})V_{filter} = \frac{\pi}{4}(d_{f,wet})^2 L \tag{6.8}$$

giving

$$\frac{1-\varepsilon_0}{1-\varepsilon_{\mathrm{wet}}} = \left(\frac{\mathrm{d_{f,0}}}{\mathrm{d_{wet}}}\right)^2 \tag{6.9}$$

Furthermore

$$\varepsilon_{\mathrm{wet}} = \varepsilon_0(1-\mathrm{S}) \tag{6.10}$$

Substituting Eqs. 6.9 to 6.10 into Eq. 6.6 finally leads to Eq. 6.3:

$$\frac{\Delta \mathrm{p_{channel}}}{\Delta \mathrm{p_0}} = \frac{1}{(1-\mathrm{S})^{4.55}}$$

7

Contributions of the liquid film to the differential pressure and the mechanisms behind it

According to the classical view of the Film-and-Channel-Model, the contribution of the liquid film to the overall differential pressure of a mist filter, Δp_{jump}, is a purely capillary driven phenomenon representing the pressure energy (of air) required to drive liquid out of the (wettable) porous filter matrix in order to maintain steady operation. Accordingly, this so-called capillary exit pressure should only depend on capillary parameters such as the pore sizes of the filter medium and properties of the liquid. The independence of Δp_{jump} on the face velocity and the oil loading rate was indeed confirmed in the previous Chapter 6.

However, recent publications by Chang et al. (2016, 2017) present new data suggesting that Δp_{jump} depends on the thickness of the liquid film. Along with the data, the authors offer an entirely different mechanistic explanation for their observations, according to which frictional pressure losses of the air flow *within* the open pores cause Δp_{jump}. Such an explanation appears reasonable, given that structural properties of the film, such as its thickness and pore size distribution, are responsible for the resistance to the air flow through the pores of the film, and thus for Δp_{jump}. Also, a linear dependence between pressure loss and the thickness of porous matrices is well-established for low-Re laminar flows dominant filters (e.g. Carman and Kozeny, 1956; Darcy, 1856).

This mechanism proposed by Chang et al. is in direct contradiction to the Film-and-Channel-Model of Kampa et al., whose work implies that frictional pressure losses are negligible compared to the necessary pressure to displace liquid from the largest pores in the film region. In particular, there should not be any dependence on the thickness of the liquid film.

Given that the observations and explanations of Chang et al. present a direct challenge to the Film-and-Channel-Model, an experimental investigation into the relationship between Δp_{jump} and film thickness was carried out. The experiments of these authors are reproduced and alternative explanations are offered for their observations.

7.1 Characterization of $\triangle p_{jump}$ and film thickness

A comparison between Δp_{jump} and the film morphology requires corresponding measurements of both parameters under the same filter operating conditions. Direct measurements of either quantity during filter operation have so far been impossible due to the mobile nature of the liquid film and the limitations of the available measuring techniques. Currently, the techniques used for either measurement are indirect and associated with certain pitfalls in interpretation which will be reviewed below, alongside the presentation of new data shown in Fig. 7.1.

Δp_{jump} is typically derived by a graphical analyis of the overall Δp curves during loading. Moreover, graphical analysis is based on segment-wise linearization of the loading curves such as those of Fig. 7.1, for the channel and film sections as well as steady-state operation. For this graphical analysis to be accurate, the transitions from one phase to another have to be clearly identifiable. In this regard, locating the transition point from channel to film formation is always more arbitrary, because it is more gradual than the subsequent transition from the film formation phase into steady state (black curve in Fig. 7.1).

When a drainage layer is added to the downstream side of the filter media sandwich, the transition from channel region to film formation always becomes even more rounded (blue curve in Fig. 7.1). (Drainage layers consist of a much coarser media and are commonly used to reduce re-entrainment without a noticeable impact on the pressure drop of the complete filter.) These extra layers begin to accumulate oil while the film has not been fully developed yet, thereby delaying the complete formation of the film and slowing down the corresponding formation of Δp_{jump}. This becomes important when trying to understand the experiments of Chang et al., who routinely included such

drainage layers in the construction of their filters and consequently observed drawn-out loading curves similar to the blue curve in Fig. 7.1. If one is not careful to wait for the steady state to be reached, these curves can be interpreted to suggest a lower value for Δp_{jump} (Kolb and Kasper, 2019b).

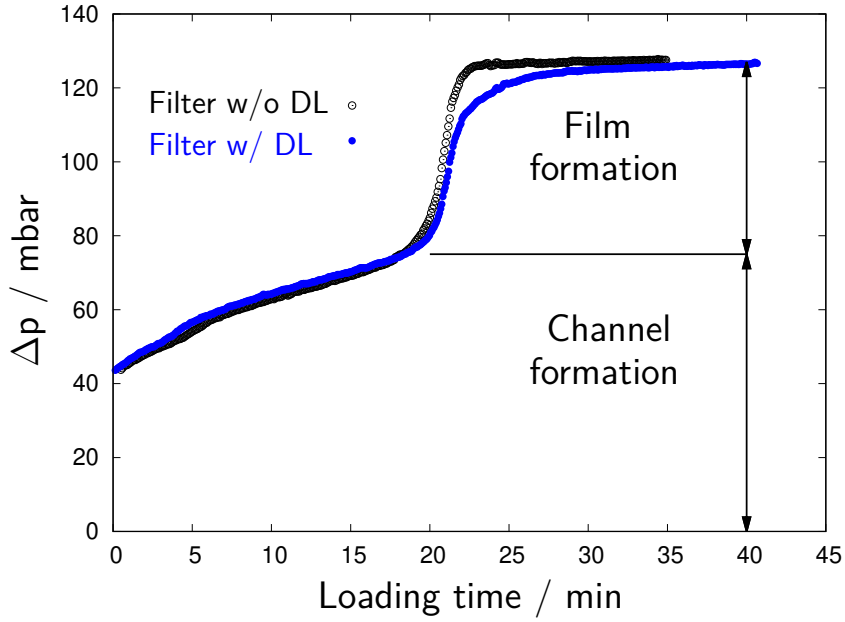

Figure 7.1: Channel and film formation prior to steady state in wettable mist filters at identical operating conditions. The only difference between the two curves is an additional drainage layer (DL) on the rear side of the blue curve's experiment.

The only direct measurement of a liquid film thickness reported so far are those of Kampa et al. (2014) who used a special UV polymerization technique to "freeze" the film during operation. Their SEM pictures indicate a smooth film of about 200 µm located on the downstream filter face but still *within* the filter media. The paper states that the film is formed "...on the rear face of a wettable filter medium..." – a statement that seems to have been adopted literally by Chang et al. who describe the film as a self-supporting structure attached to the *outer* surface of the last media layer. Accordingly, the authors have to assume that the pressure drop produced by the film $\Delta(p_{jump})$ is unrelated to the pore structure of the filter, and produced by the air flow through continuous pores in a film of variable thickness. How those open pores might form or how large they are, is not explained. It also remains unclear what keeps the pores open in the absence of a fibrous framework.

As discussed in earlier sections of this work, the liquid film collapses and becomes immediately absorbed by the last media layer when the air flow is shut off. This opens up an indirect method of estimating the film thickness: Liquid from the film contributes significantly to the saturation value of the

last layer, S_n, and entails a characteristic U-shape of the saturation profile in wettable filter media. Besides the film liquid, the oil channels also contribute to S_n; namely in a similar fashion as they contribute to the saturation of the second-to-last layer, S_{n-1}. A simple approach to model the liquid distribution in the last layer is to introduce a sharp boundary between channels and a completely closed film (the open pore volume within the film can be neglected). This model can be formulated as:

$$f = \frac{S_n - S_{n-1}}{1 - S_{n-1}} \tag{7.1}$$

wherein the non-dimensional film thickness $f=\delta/L$ relates the thicknesses of the liquid film, δ, with the thickness of a single layer, L, with $S_n \geq S_{n-1}$.

Closer examination of Eq. 7.1 shows that f increases linearly with S_n for a fixed value of S_{n-1} but decreases rapidly with S_{n-1} when S_n is kept constant; it goes to 0 as S_{n-1} approaches S_n and it becomes unity when S_n approaches 1. The latter directly illustrates a limitation of Eq. 7.1 and the underlying model as the film must not be thicker than a single layer.

7.2 Dependence of Δp_{jump} on the film thickness

The previous Chapter 6 presented extensive data which on the one hand show that Δp_{jump} remained constant across a wide range of operating conditions (Fig. 6.4), while on the other hand the channel saturation (i.e. S_{n-1}) was highly variable (Fig. 6.5). Aside from the absence of a correlation between the two parameters, the variability of S implies that the film may have indeed varied in thickness.

Therefore, film thicknesses for this data set were calculated according to Eq. 7.1 and are compared against Δp_{jump} in Fig. 7.2. Note that the lower x-axis uses the non-dimensional f while the upper x-axis is in terms of absolute film thickness. The resulting values span a range from 38 to 50 mbar for Δp_{jump} and 50 to 200 µm of film thickness. The range of thicknesses is similar to those observed in the SEM pictures of Kampa et al. (2014). Despite some scattering in the values of Δp_{jump} around a mean of 43 mbar, there is no apparent correlation with f. This clearly contradicts the phenomenological picture of Chang et al., according to which one would have expected a linear dependence between f and Δp_{jump}.

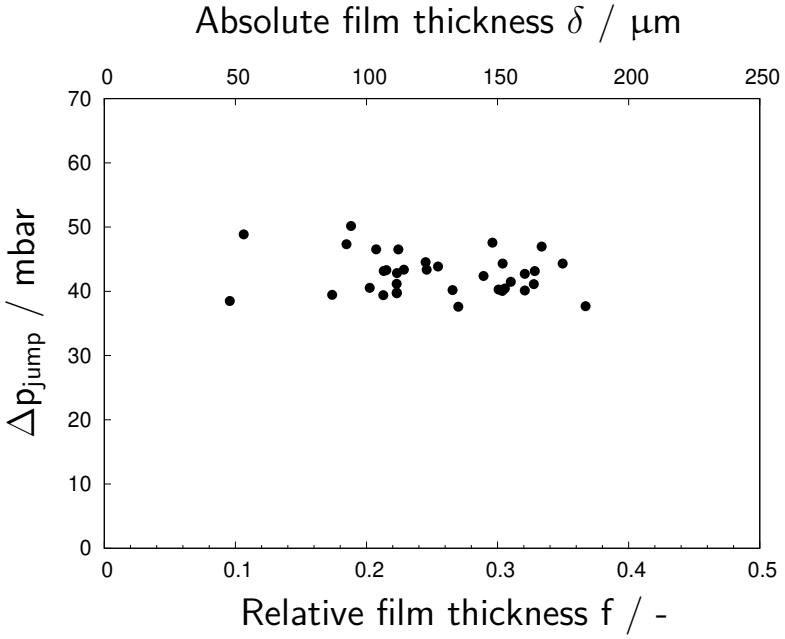

Figure 7.2: Distribution of Δp_{jump} and corresponding film thicknesses for a wide range of operating conditions. Film thicknesses are calculated from the saturation difference between Layers 9 and 10 and are based on the complete dataset of Chapter 6.

The main difference between the experiments of Chang at al. and those of Kampa at al. (as well as those reported in this work) in the use of an additional drainage layer on the rear side of the filter. In order to explain how Chang et al. arrived at their conclusion, the effect of such a drainage layer on the film thickness and Δp_{jump} was investigated with new experiments shown in Fig. 7.3. The figure shows saturation profiles for an 8-layer glass fiber (GF) filter with and without drainage layer (DL), as well as for a 6-layer GF filter including a DL. Note that the data in Fig. 7.3 are arranged so that the profiles overlap in Layer 8 (i.e. in the film layer).

All three data sets show a constant saturation value of about 0.45 for their front-most layers and for the respective last GF layers containing the film. The saturation of the drainage layer (Layer 9) is also constant but significantly lower. On the other hand, the channel saturation clearly increases in the presence of a DL layer. Arithmetically, the increased levels of S_{n-1} (or S_7 in Fig. 7.3) leads to thinner films on the basis of Eq. 7.1.

It is important to note, that this increased saturation of the rear layers is most likely due to capillary re-arrangement of liquid from the coarse drainage layer into finer glass microfiber medium. The reservoir for this liquid is a small but completely saturated strip of oil at the filter bottom of the drainage layer from which oil is drawn back into the lower parts of the preceding GF layers (Kolb and Kasper, 2019b). The apparent decrease of film thickness in the presence of drainage layers reported by Chang et al. is thus a misinterpretation of experimental observations.

Furthermore, was shown earlier in Fig. 7.1 that the presence of a drainage layer delays the formation of the film, thereby leading to a more "rounded" Δp curve during the jump, but does not impact its final value – provided one waits long enough to reach steady state. It thus seems likely that Chang et al. also misinterpreted their pressure drop curves with regard to Δp_{jump}.

The observation of a variable film thickness in the presence of a drainage layer is most likely the strongest argument against a correlation with Δp_{jump}. Moreover, the variable thickness can also be seen from experiments without a drainage layer: the film becomes thicker in direction of drainage as it is fed by uniformly distributed oil channels in the cross-section of the filter. Horizontal stripes of the last layer show a corresponding increase of saturation (Liu et al., 2016) which can result in a 4-fold increase of the film thickness across filters of 5 cm height (Wurster et al., 2017). It becomes clear that values obtained by Eq. 7.1 always represent an average across the complete filter height. This fact may help to understand different perceptions of the film's location as discussed at the beginning of this chapter: It seems plausible that part of the film drainage is gradually occurring outside the last media layer as the film becomes thicker. However, the variable film thickness renders discrepancies between Kampa et al. (2014) and Chang et al. (2016) of the film's exact location a moot point as it questions any effect on Δp_{jump}: If a thicker film were to cause more Δp_{jump}, then this would cause a major re-distribution of the air flow from the bottom to the top of the filter. These changes had to take place within a very short distance from the film which is questioned by the fundamentals of filtration (e.g. Brown, 1993).

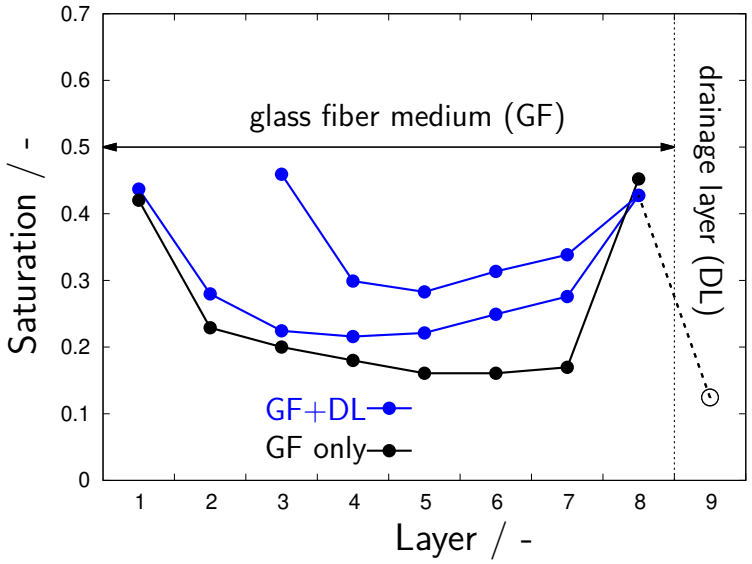

Figure 7.3: Saturation profiles in filters with and without a drainage layer. Increased saturation values in Layer 8 can be attributed to the film. The increased saturation in the mid-section of filters with a drainage layer is due to a higher saturation in the bottom part.

7.3 Dependence of $\triangle p_{jump}$ on the bubble point

So far it has been shown that the original argumentation of Chang et al., according to which Δp_{jump} is primarily caused by frictional losses of the air flow through pores of a "solid oil film", is clearly untenable[1]. Kampa et al. (2014, 2015) on the other hand describe film formation as a capillary phenomenon independent of film thickness, face velocity, and oil loading rate. Moreover, Kampa's point of view seems to be supported from data of this work. One could therefore adopt their capillary model without questioning. For the sake of completeness and fairness this model will nevertheless be examined critically in the same way as its "solid-film" alternative was in the previous chapter.

According to Kampa et al., the film (in wettable filter media) forms to build up the capillary pressure necessary for liquid to exit the media. If one thinks of the downstream face of the fibrous filter matrix as a system of parallel capillaries, then a certain Δp is indeed required to displace liquid from some of the pores in the film region and free them up for the passage of air. In fact, even the smallest air flow requires this pressure to be overcome, not only large air flows typical of mist filter applications. In logical consequence, Kampa et al. (2015) compare Δp_{jump} with the so-called bubble point, a commonly measure to characterize pore sizes in sheets of filter media (Calvo et al., 1996; Qin and Wang, 2006; Li et al., 2006). The bubble point represents the capillary exit Δp of the largest pore of an infinitesimal small air flow. It is reached when the first gas bubbles emerge from the fully saturated media.

A key argument used by Kampa et al. to support their capillary model for the film formation was the observation of a linear correlation between Δp_{jump} and the bubble point for a wide variety of filter media. Interestingly however, their measured bubble points were consistently higher by a factor of about 2 compared to Δp_{jump}. This implies pore sizes larger than the largest possible pores determined with the bubble-point technique and therefore poses a problem for the model. One possible explanation for this apparent discrepancy in the Kampa et al. data may be due to their rather special technique of using a combination of both wettable and non-wettable filter media in the same filter sandwich. This allowed them simultaneous measurements of the Δp_{jump} for two types of media in one experiment. (Whereby the Δp contributions of both film collapse into a single Δp_{jump} with slightly different slopes as a marker to differentiate them.) On the other hand, there seems to have been an interaction between the two media, causing deviations from the standard behavior.

[1] Chang (2019) recently acknowledged the correctness of the arguments presented in Section 7.2 and retracted the picture of a capillary system with frictional pressure losses along the pores.

Experiments in the current thesis were all performed with uniform (either completely wettable or non-wettable) media, thereby avoiding potential complications of an internal interference. One can therefore revisit these data to make comparisons between the bubble point and Δp_{jump}. Fig. 7.4 is a compilation of the respective Δp_{jump} and bubble point values for 4 different grades of wettable media, among them the data points of the fine medium from Fig. 6.5 which were used earlier to show that Δp_{jump} is independent of face velocity and oil loading rate. The data for the most open-pore medium (coarse 2) are of interest because they show that Δp_{jump} remains independent of flow velocity also for glass microfiber media of lower efficiency grades.

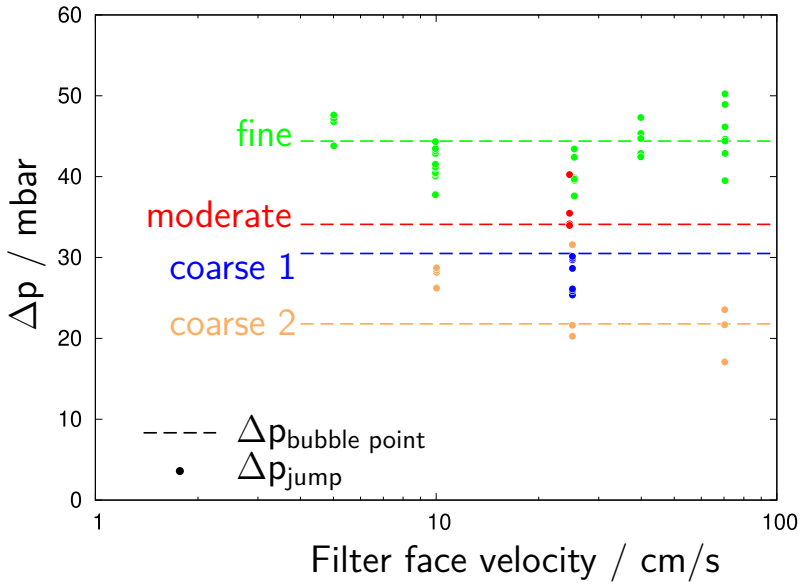

Figure 7.4: Values of Δp_{jump} (circles) for different grades of wettable filter media. Filters were loaded with variable face velocities (fine, coarse 2) or at 25 cm/s (moderate, coarse 1) at a constant oil loading rate of 125 mg/(m^{2}s). The dashed lines represent values of the bubble point (cf. Sec. 10.1) and are obtained with the same kind of mineral oil as the filtration experiments.

Despite significant scatter among the Δp_{jump} values in Fig. 6.5, the agreement between Δp_{jump} and $\Delta p_{bubble\ point}$ is generally good without systematic deviations. In fact, Δp_{jump} data seem to be distributed evenly around the respective bubble points. Moreover, for the most comprehensive data set of the fine medium, the average value of Δp_{jump} agrees within 1% with the bubble point.

There is clearly no factor of two between the bubble point and Δp_{jump} as reported by Kampa et al. (2015). Moreover, the good agreement between the dynamic Δp_{jump} required to overcome the film during filtration, and the static bubble-point Δp to overcome the capillary pressure of the largest pores lends further support to the notion that Δp_{jump} is a predominantly capillary phenomenon governed by the pore sizes of the filter medium. Of course, this

lends further support to the Film-and-Channel-Model and relegates the ideas of Chang et al. to the realm of speculation.

The observation that Δp_{jump} does not only correlate but equals the bubble point for a wide range of filter media and face velocities leads to several conclusions: Firstly, the air flow always prefers the largest pores because of their lower capillary restriction. The necessity to overcome this capillary and constant contribution therefore sets Δp_{jump} as a lower limit to the overall Δp of a mist filter in steady-state operation. Furthermore, the largest pore sizes are apparently available in sufficient number to cope with a wide range of air flows. This is surprising because these pores do not significantly contribute to the complete pore size distribution. Finally, there is no evidence for any significant additional contribution to Δp_{jump} besides the bubble-point pressure – especially not by frictional losses within the pores; the film thickness has no effect on Δp_{jump}.

These conclusions are helpful to understand the physics behind Δp_{jump} but they cannot explain the scatter of measurements around the bubble point observed in Fig. 7.4. A simple explanation for higher Δp_{jump} values than the bubble point would be the need to activate additional smaller pores when there are not enough largest pores to cope with the air flow. This may theoretically explain higher values of Δp_{jump} but is not supported by the fact that Δp_{jump} is independent of the face velocity. One can thus conclude that the number of the largest pore size is sufficient for all filter face velocites of technical interest.

Another, perhaps better reason for values of Δp_{jump} above the bubble point is the compression of the downstream filter media on its support grid (Hussain, 2009). This compression may lead to a shrinkage of the largest pores during operation and lead to higher pressure for the capillary exit of oil. A significant effect of compression beyond the deviations of Fig. 7.4 seems not likely because the glass microfibers are embedded in a rigid matrix of acrylic or epoxy binder.

Values for Δp_{jump} below the bubble point imply the existence of pore sizes larger than the largest pores of the media. This seeming contradiction may be resolved only if the Δp_{jump} measurements make use of a different pore size distribution than the bubble point measurements. In fact, the latter always depart from a completely saturated media layer ($f \approx 1$; in other words, they make use of the entire thickness of the sample. The film however forms only in a narrow region near the downstream media surface ($f \approx$ 0.1-0.4). Therefore, the bubble point experiments are based on longer pores, which are known to shift the pore size distribution towards smaller pore sizes (Li et al., 2006). This can be attributed to more "bottlenecks" as caused for instance when a pore is tapered by through-going fibers.

8

Contributions to the filtration efficiency by liquid films and channels[1]

Abstract

Building on work by Kampa et al. (2014) about the liquid distribution in multi-layer oil mist filters, a mesoscale empirical model is proposed for their efficiency. It decomposes the total penetration into a product of independent "building blocks" that are aligned with the mesoscale liquid distribution in steady state, essentially in the form of an oil film and a channel region. The film (typically one very thin region per sandwich) is associated with a film penetration P_{film} and the channel region (consisting typically of multiple layers) with a channel penetration $P_{channel}$. The first layer of wettable media also represents a separate contribution $P_{1st\ layer}$.

A method is described to derive these unit penetrations from a set of measurements. Experiments are then carried out with filters composed of conventional glass microfiber media, both wettable and non-wettable to compressor oil,

[1]This article was published as: Kolb, H. E., A. K. Watzek, V. Zaghini Francesconi, J. Meyer, A. Dittler and G. Kasper (2018). *A mesoscale model for the relationship between efficiency and internal liquid distribution of droplet mist filters*, Journal of Aerosol Science 123, 219–230.

in which the fractional penetration of the entire sandwich was measured by SMPS between about 30 and 700 nm. It is shown that the film penetration is substantially reduced for particles above about 100 nm in comparison to that of the dry media due to enhanced inertial deposition, while the channel penetration is generally higher across the board, probably because of a loss of active fiber in the partially saturated media. The last part of the paper is dedicated to practical consequences of this efficiency model.

It is shown that the fractional efficiency for an arbitrary number of (identical) layers can be predicted quite accurately from the unit penetrations. Additional measurements of the total downstream concentration as a function of time are used to discuss and explain changes from start-up until steady state.

Keywords: filtration efficiency, oil mist, coalescence filter, film-and-channel model

8.1 Introduction

Glass fiber media have proven themselves successfully for the removal of very fine droplet aerosols such as oil mist generated by oil lubricated compressors or combustion engines. Although the efficiency of fibrous mist filters follows well-established mechanisms such as diffusion, inertial impaction and interception, the changes in filter behavior due to the *accumulation* of such liquid aerosols in the filter matrix (often called coalescence) has little in common with that for solid particles. Deposited mist droplets coalesce with time into much larger regions of liquid that move along the direction of the air flow until the liquid begins to drain from the rear side of the filter. With the onset of drainage, the filter reaches a steady state. As with every "particle" loaded filter, the accumulation of liquid leads to substantial changes in pressure drop and filter efficiency, which have been the subject of scientific investigations for some time.

The classical treatment of filter efficiency in a fibrous matrix always departs from single fiber theory, a well-established model that, among other things, requires certain structural information about the fiber geometry. Moreover, the ensuing changes in filter efficiency will depend on how this structure changes with particle accumulation on fibers and in pores. In the case of dust filtration, one can usually assume that particles remain in the location where they were first deposited. The resulting dendritic accumulation structures around fibers (Kanaoka et al., 1980) usually lead to a significant increase in single fiber efficiency (Kasper et al., 2009). Liquid droplet aerosols deposited on an individual, isolated filter fiber will not coalesce into a homogeneous film

but form a chain of drops (see Müller et al., 2014). For a wetting liquid these drops are barrel shaped and envelope the fiber (Fairs, 1958; Briscoe et al., 1991; Mullins et al., 2006) while on non-wettable fibers they take the shape of a "clamshell" (Mullins et al., 2005). As opposed to dry particle deposits, this liquid generally causes a reduction in filter efficiency. In order to apply single fiber theory to this type of structures, Payet et al. (1992) distributed liquid between fibers in such a way that some fibers were removed from the filtration process entirely while others remained clean. Along the same lines, Raynor and Leith (2000) made assumptions about the spacing between drop covered and bare regions on a fiber. Other authors (Conder and Liew, 1989; Agranovski and Braddock, 1998; Frising et al., 2005) distributed the liquid phase as a film that surrounds the fibers.

Unfortunately, coalescing liquid does not stay in place, but keeps moving and rearranging itself due to the forces of capillarity and the air flow until the filter eventually reaches a steady state. In this macroscopic steady state, the internal liquid distribution nevertheless assumes a reasonably stable and defined "structure", first described for glass fiber media by Kampa et al. (2014) with a semi-empirical meso-scale model that has become known as the "Film-and-Channel-Model". According to their observations, coalesced liquid *inside* the media is transported in distinct parallel channels that persist through multiple (identical) filter layers and effectively block a part of their cross-section while leaving other regions dry. On the other hand, coalesced liquid trying to exit (or enter) the media *at an interface to air* or other media builds up a quasi-continuous film.

The Film-and-Channel-Model has successfully explained the evolution of the filter differential pressure as a function of liquid loading and other parameters such as air velocity, liquid viscosity or wettability (Kampa et al., 2015; Kolb et al., 2017). However, it has not yet been applied to the filter efficiency. Since the channel region and the film represent spatially distinct regions of a coalescence filter, one would think that they also make separate and definable contributions to the overall efficiency. In the following we will outline an experimental technique for quantifying these contributions and assigning to each region a specific (and independent) penetration, $P_{channel}$ or P_{film}. We then study the dependence of these unit penetrations on factors such as particle size and total number concentration, but also on properties such as media thickness, wettability and fiber diameter. The technique is illustrated by experiments conducted with standard glass fiber media and standard compressor oil.

8.2 Experimental materials and methods

Experimental set-up

A schematic diagram of the experimental set-up is given in Fig. 8.1. The aerosol is generated by a Collison nebulizer and a typical compressor oil (surface tension 31 mN/m, dynamic viscosity 122 mPa s). Number concentration and size range of the generated droplets were kept constant throughout an experiment by maintaining a constant Δp across the nebulizer. The aerosol was mixed with dry compressed air in a chamber in order to keep the flow rate upstream of the filter constant. For this purpose, temperature as well as absolute pressure before the filter were monitored continuously and used to compensate for the increase of filter differential pressure during loading. Subsequently, the aerosol was introduced to a filter holder which contained a variable number of layers of flat sheet glass fiber media. A tight seal was guaranteed. A balance below the filter chamber collected the draining oil from the rear side of the filter.

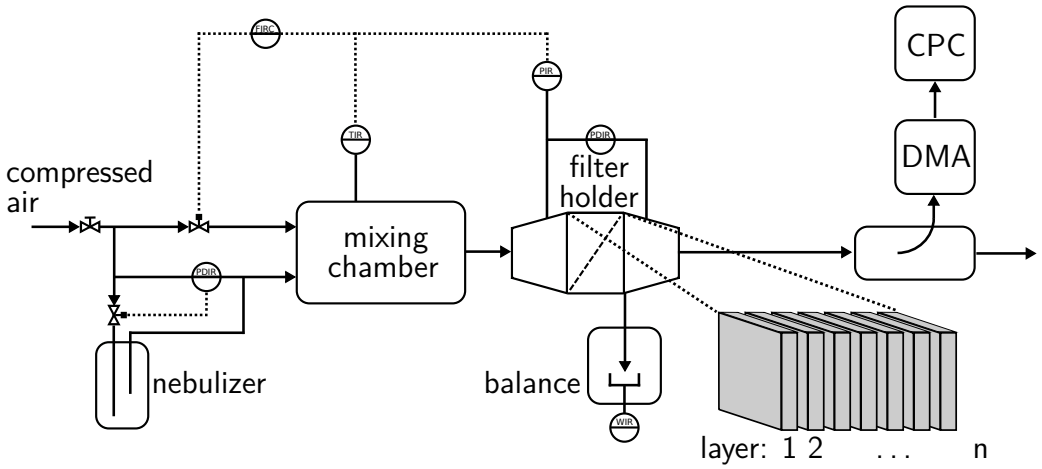

Figure 8.1: Schematic diagram of the experimental set-up for the loading of glass micro-fiber media with oil aerosol and measuring the penetration of stacks of flat layers.

The aerosol penetrating the filter was sampled iso-kinetically with a 90° probe. A small portion (1 L/min) of this stream was directed to an electrical mobility aerosol classifier (^{85}Kr neutralizer, DMA model Hauke Vienna Long combined with CPC model TSI 3010), a standard tool for aerosol characterization, to determine the downstream droplet size distribution and concentration. The upstream droplet size distribution and concentration were measured by removing the filter.

Experimental procedure

Before and after each experiment the droplet size distribution upstream of the filter was measured by mounting the empty filter holder without any filter media and taking the average of three successive SMPS scans each. The inlet distributions were approximately log-normal, with marginal variations between before and after as illustrated in Fig. 8.2. (The diameter designation as "mobility equivalent" will be dropped from here on because these particles were ideally spherical droplets.) The upstream concentration was therefore considered constant within the time spans of an experiment and the mean of "before" and "after" was used as reference concentration when calculating the penetration.

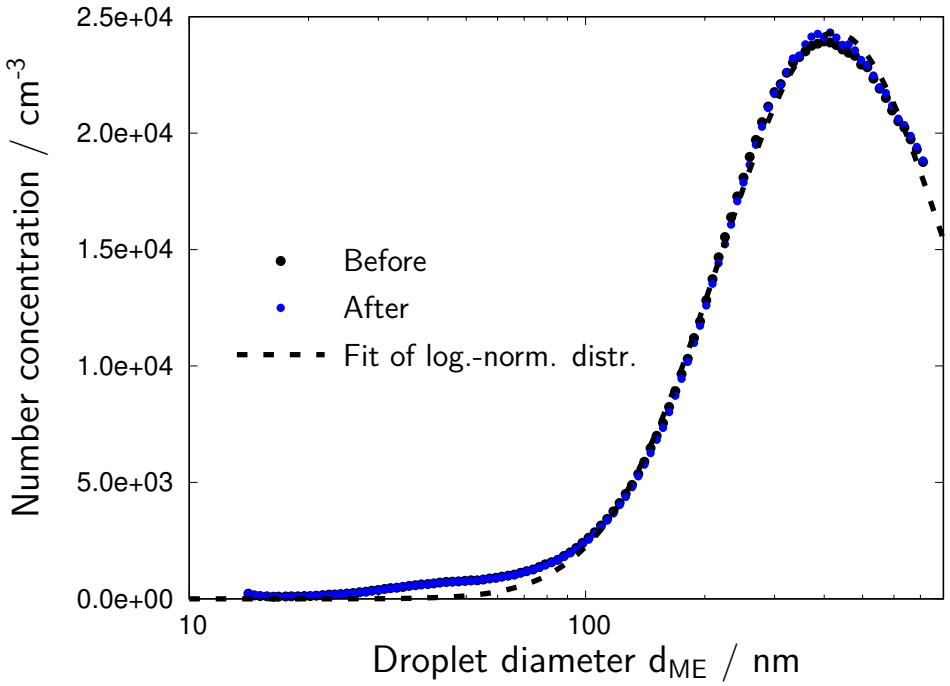

Figure 8.2: Droplet size distribution upstream of the filter before (t=0) and after 3 hours of loading.

Each experiment started with a dry filter that was loaded with oil mist until steady state was reached as indicated by the Δp signal. Measurements of the penetrating aerosol were done at specific times during the loading process (as discussed later on in detail) and also in steady state. All operational parameters were recorded continually during a run. Pressure drop across nebulizers and face velocity were held constant at 1 bar and 25 cm/s respectively for all experiments. The saturation of each layer was measured gravimetrically at the end of an experiment.

Filter media

Modern glass microfiber media are often too efficient to be useful for the type of efficiency measurements we describe below, because the downstream concentrations are too low for statistically reliable concentrations. We therefore chose to experiment with relatively "coarse" and "medium" efficiency grades of wettable and non-wettable media. A fine grade filter was also included, but only in order to highlight the issue of re-entrainment.

Media were obtained in part from BinNova GmbH and also from Hollingsworth & Vose. An overview of the media properties is given in Tab. 8.1. Inter-comparisons between wettable and non-wettable media are not possible because the fiber mix and hence the penetration for a given grade differ. Note however, that the objective of this paper was not to decide between more or less performing, wettable or non-wettable media, but rather to measure the effect of channels and liquid films on the penetration of droplets for a range of glass microfiber media. In this regard, wettability decides whether the liquid film is formed at the front or the rear face of a filter, as discussed in the following section.

Grade	Fiber diameter / µm	Porosity/ -	Thickness/ mm	Largest pore/ µm	Mean pore/ µm
wettable					
Coarse	4.0	0.939	0.64	37.2	13.4
Medium	2.9	0.934	0.51	32.9	8.5
Fine	1.4	0.931	0.42	18.2	2.7
non-wettable					
Coarse	2.6	0.943	0.48	41.8	5.7
Medium	2.1	0.937	0.45	34.0	3.8

Table 8.1: Properties of filter media used in our experiments.

The thickness per layer was measured with a caliper on media stacks of 10 layers, which were compressed by a weight corresponding to approx. 100 mbar of Δp. The porosity was calculated from the weight of the sample and the corresponding thickness, assuming the media to consist only of glass. Values of the pore size distribution were obtained with capillary flow porometry using a non-volatile silicone oil as wetting liquid (Kolb et al., 2018). Glass fiber media typically consist of a broad range of fibers. The equivalent fiber diameters in Tab. 8.1 were calculated by fitting the Δp-model by Davies (1973) to experimental Δp data. Evidently, the Δp of the dry media increases toward finer grades as seen by the decreasing fiber diameter. Note however, that fiber diameters (as well as values for the penetration in Section 8.4.2) of non-wettable media are generally lower than their wettable counterparts of the same grade. With regard to other parameters listed in Tab. 8.1, wet-laid glass fiber media typically fall into a very

narrow range, even though their filtration performance differ greatly from each other. Least pronounced are differences in porosity and thickness (i.e. purely geometrical properties), most pronounced are flow relevant properties such as fiber diameter and mean flow pore size (which seem to correlate). The largest pores are an indicator for the height of the "Δp-jump" (Kampa et al., 2014) and do follow the trend of the fiber grades.

8.3 Film-and-Channel-Model

The phenomenological Film-and-Channel-Model by Kampa et al. (2014) describes how oil is transported through glass fiber media in channels or liquid films, as well as the implications of this transport for the filter pressure drop. In the following, we use data obtained with media from the current study to discuss key aspects of the Film-and-Channel-Model as they pertain to filter efficiency.

8.3.1 Evolution of Δp and saturation

The temporal evolution of the loading curves, i.e. the differential pressure drop Δp vs. time (Fig. 8.3) reveals the relevant mechanisms involved in the filtration of mist by fibrous media. The figure shows the loading curve for one non-wettable (in our case, oleophobic) medium, as well as the loading curves for a wettable (oleophilic) medium consisting of 1 and 4 layers, respectively.

Stating at t=0, the **non-wettable medium** (blue curve) briefly shows a gentle increase in Δp due to the deposition and accumulation of the very first oil, followed by a steep jump due to the formation of an (almost) closed film of coalesced liquid. Since the air flow continues to pass through (mainly) the largest pores of the medium, these pores have to be kept open during operation by a steep increase in Δp, which has been coined "Δp-jump" by Kampa et al. (2014). Subsequently, the coalesced oil traverses the filter in channels. Maintaining this flow also requires a certain amount of additional Δp per layer, on top of the Δp_0 need to pump the air through the dry filter. Once the transported oil reaches the rear side of the oleophobic filter, it drains as big drops without an additional second film. The onset of drainage marks the so called steady state during which the rate of drainage equals the rate of aerosol deposition.

For **wettable media**, the oil transport and corresponding evolution of Δp basically proceed in the reverse order, in that liquid enters the media freely on the upstream side of the filter, while the film and attendant Δp-jump form on

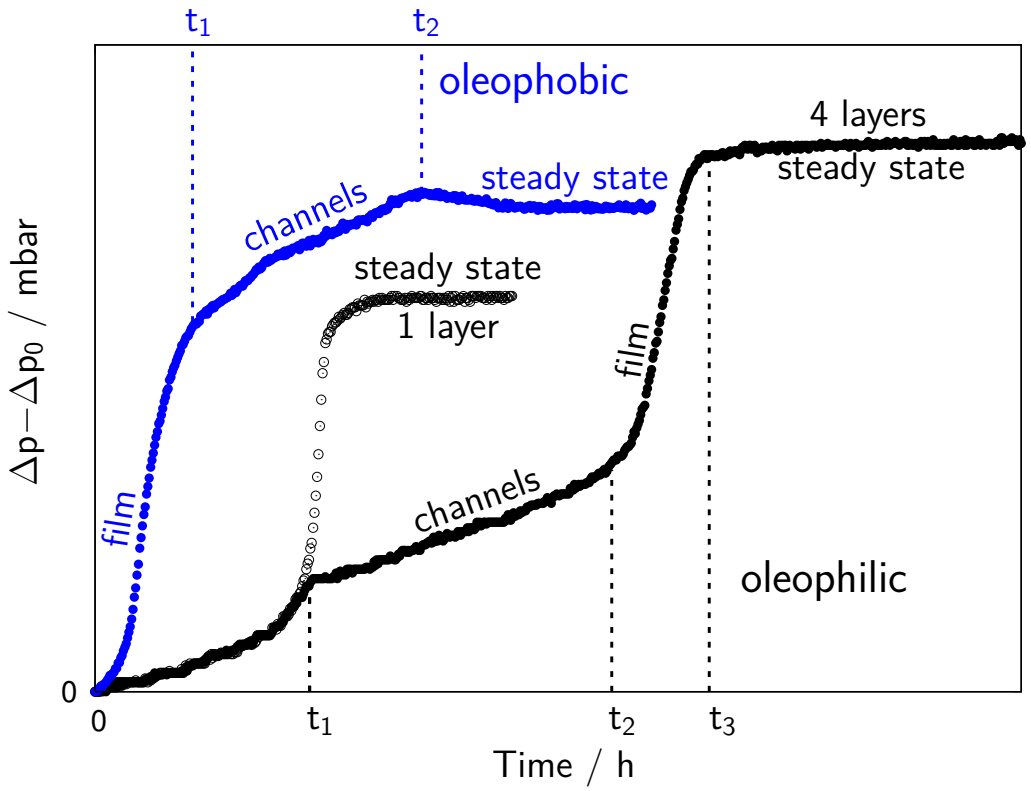

Figure 8.3: Temporal evolution of Δp increase for multi-layered wettable and non-wettable filter media sandwiches. Characteristic times mark the completed formation of channels (t_2), liquid film (t_1, non-wettable and t_3, wettable) and 1st layer (t_1, only in wettable media).

its rear face. One additional, subtle but important difference to non-wettable media is the role of the first layer which, in terms of aerosol mass, collects the bulk of the oil mist and thus serves the purpose of a coalescing and feeder stage for the oil channels. This typically entails a higher saturation and thus a higher Δp-channel than the following layers (Fig. 8.4). There is also a slight discontinuity in Δp as oil begins to cross into the second layer (at time t_1 in Fig. 8.3) and organize itself into channels. Over all, loading curves of Δp vs. time, such as those depicted in Fig. 8.3, give a good correlation between the temporal and spatial evolution of the oil front traversing a filter. Characteristic times marked in Fig. 8.3 are indicators for the instance when channels proceed into the second layer (in wettable media), or when film and channels are completely developed as the filter enters into its steady state.

Corresponding steady-state saturation profiles for coarse and medium grade sandwiches with variable number of layers can be seen in Fig. 8.4. Obviously, the unit of resolution of these profiles is the thickness of a single layer because the average saturation for each layer was determined gravimetrically, after the experiment had been shut off. The first layer of the wettable media (the

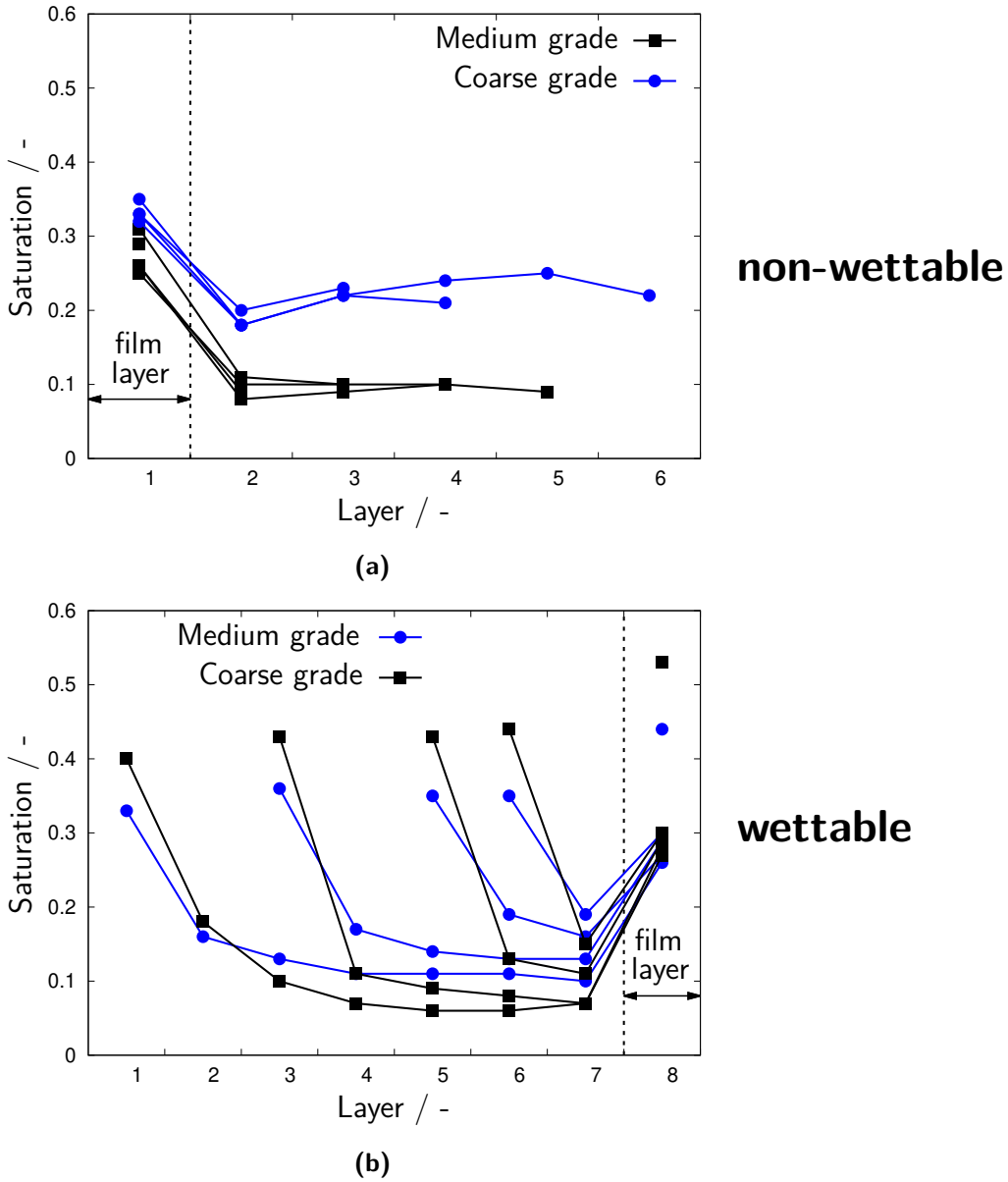

Figure 8.4: Steady-state saturation profiles as a function of layer number for multi-layer sandwiches of non-wettable (a) and wettable media (b) operated at v=25 cm/s and R=110 mg/(m^{2}s). Note that the layer containing the film is either Layer 1 or Layer 8.

coalescence and feeder layer) as well as the layers containing the film (Layer 1 for the non-wettable medium, Layer 8 for the wettable medium) have high levels of saturation. By comparison, the saturation of typical channel layers is low and the profile is sufficiently flat to treat it as constant for the entire channel region. Note also that for both grades of wettable media, the saturation of the first layer is constant (approx. 42% for the coarse and 35% for medium grade) and independent of the subsequent number of layers.

These saturation level patterns are important for subsequent discussions because layers with equal or very similar saturation will be considered as having similar underlying particle collection mechanisms and similar filter efficiencies.

8.3.2 Penetration of particles

In the following we shall describe a method for extracting the contributions by specific regions of a mist filter to the fractional penetration of the entire sandwich in steady state. The method is based on filter penetration rather than efficiency, because its assumes that successive "regions" – such as layers with fully developed liquid channels or the liquid film – each represent an independent fractional penetration P_i by droplets of a given size. The total fractional penetration can then be represented as the product of the individual penetrations, with n identical layers of equal thickness and function giving a total penetration $P=P^n$.

The subdivision of the filter into specific "regions" basically follows the saturation profile in flow direction, as represented for example by Fig. 8.4. Individual filter layers are typically modeled as each contributing one distinct P_i which depends largely on their level of saturation. For example, the channel region consists of a number of layers with approximately equal saturation that are each assumed to make the same contribution $P_{channel}$; and in case of wettable media, the 1st layer also represents a region with distinctly different saturation from the channel region, hence the contribution $P_{1st\ layer}$. The only exception is the layer with the film, which is modeled as consisting of two regions: a small fraction of that layer (with $S\approx1$) contributes P_{film}, while the remainder of that layer (considered as having the same saturation as the adjacent channel layers) contributes a corresponding fraction of $P_{channel}$.

For a *filter consisting of n structurally identical non-wettable layers*, the overall steady-state penetration P is thus given by the contribution of the film, P_{film} (which occupies a fraction $f<1$ of Layer 1), and the identical contributions $P_{channel}$ by each of the channel layers

$$P = P_{film}\ P_{channel}^{n-f} \tag{8.1}$$

In this expression, the exponent n-f takes into account that part of the front-most layer is occupied by the film and hence does not contribute to the separation of droplets within the channel section.

For a *filter consisting of structurally identical wettable layers*, the 1st layer constitutes a distinctly different saturation level from the channel layers (Fig. 8.4) and must be accounted for separately. We thus obtain

$$\mathrm{P} = \mathrm{P}_{\text{1st layer}}\ \mathrm{P}_{\text{channel}}^{\mathrm{n}-1-f}\ \mathrm{P}_{\text{film}} \tag{8.2}$$

Eq. 8.1 has two unknowns (or participating penetrations), Eq. 8.2 three. One therefore needs the corresponding number of equations in order to solve these linear systems of equations. These equations must be obtained by independent measurements of P.

This can be done in numerous ways. The simplest approach would be a single experiment, during which one repeatedly measures the penetration, e.g. for the dry filter plus several measurements at the characteristic times in Fig. 8.3, corresponding to exactly known numbers of layers. However, it can be difficult for some media to identify the correct transitions times from one layer to the next. Also, the film formation happens very quickly and affects the penetration so strongly, that SMPS scans can become too slow for accurate measurements at characteristic points in time t_1 (non-wettable) and t_2 (wettable). Another option is to vary the number of layers in the sandwich. In case of non-wettable media this requires 2 measurements, $\mathrm{P_n}$ and $\mathrm{P_m}$, for sandwiches with n and m layers respectively; wettable media would require 3 such measurements.

We have chosen a combination of these options for the purposes of this study: The average *penetration per channel layer (non-wettable or wettable)* is obtained from $\mathrm{P_n}$ and $\mathrm{P_m}$, measured for sandwiches with n and m layers respectively:

$$\mathrm{P}_{\text{channel}} = \left(\frac{\mathrm{P_m}}{\mathrm{P_n}}\right)^{\frac{1}{\mathrm{m\text{-}n}}} \tag{8.3}$$

Since the film occupies the same thickness regardless of layer number, the calculated channel penetration per layer does not depend on f. For non-wettable media the film penetration is given by

$$\mathrm{P}_{\text{film}} = \frac{\mathrm{P_n}}{\left(\frac{\mathrm{P_m}}{\mathrm{P_n}}\right)^{\frac{\mathrm{n}-f}{\mathrm{m\text{-}n}}}} \tag{8.4}$$

where P_{film} now depends on f. For wettable media, the film penetration is

$$\mathrm{P}_{\text{film}} = \frac{\mathrm{P_n}}{\mathrm{P}_{\text{1st layer}}\left(\frac{\mathrm{P_m}}{\mathrm{P_n}}\right)^{\frac{\mathrm{n}-1-f}{\mathrm{m\text{-}n}}}} \tag{8.5}$$

Penetration values of the first layer were realized by the measurements at t_1 (cf. Fig. 8.3). These are easier to make than for non-wettable media because the change of penetration is much smaller.

Direct measurements of the film thickness f are technically very challenging because the film collapses immediately when the air flow is shut off. Kampa et al. (2015) obtained film thickness data by experimenting with a monomer that had fluid properties similar to oil and photo-polymerizes very rapidly in UV-light. We therefore used a simpler approach to estimate the film thickness. It divides the filter layer with the film into a fraction f containing the oil film with a saturation $S_{film} \approx 1$, and a fraction 1-f that has the same saturation $S_{channel}$ as the neighboring channel layers. Since both the average saturation $S_{film\ layer}$ and $S_{channel}$ are measured and known, one can calculate f according to

$$S_{film\ layer} = f + (1 - f)S_{channel} \tag{8.6}$$

Values calculated for the media used in this study range from 18 to 23% of layer thickness, corresponding to a film thickness between 115 and 150 µm. The estimates by Kampa et al. are close to this range.

8.4 Results and discussion

8.4.1 Calculated penetration values for channel section and film

Figs. 8.5 and 8.6 show the respective penetration curves through the oil film and per channel layer, calculated as described in the previous section. Each data point is an average of several experiments with sandwiches having between 1 to 8 layers, with errors bars representing the respective standard deviations. Standard deviations in penetration increase toward smaller particles, because these are fewer in number at the edges of the inlet size distribution.

Fig. 8.5 shows clearly that inertial deposition is the pre-dominant capture mechanism for air-borne droplets trying to pass through the liquid film. Droplets smaller than about 100 nm penetrate the film almost unhindered whereas droplets larger than about 500 nm are almost completely removed from the aerosol. The 50% cut-off values range from 125 to about 220 nm, which is surprisingly low compared to typical inertial separators.

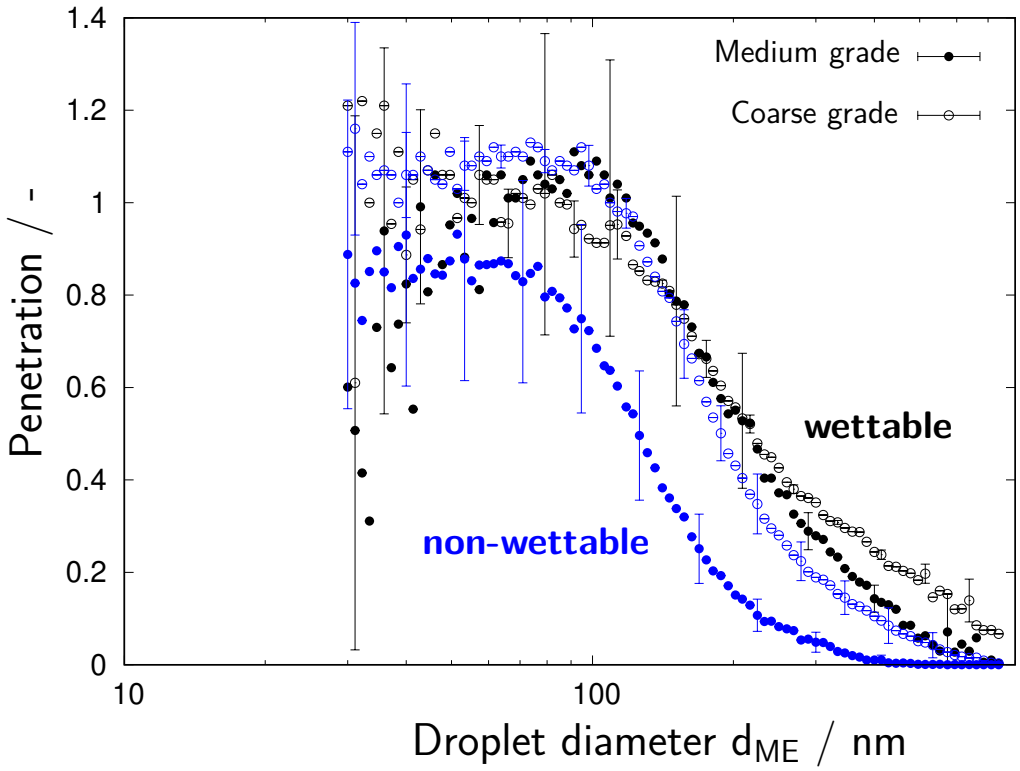

Figure 8.5: Penetration through the oil film as a function of particle size for the media investigated in this study. Open symbols (○) represent coarse media, filled symbols (●) represent medium grade media. Error bars represent standard deviations from experiments with 1 to 8 filter layers.

The simplest physical model for particle deposition on/in the film is the passage of an aerosol through an orifice plate, where impaction occurs around the upstream rim of the opening while the flow is accelerated into it. Such basic configurations have been studied in the past for various applications (e.g. Pich, 1964; Wang and Kasper, 1990; Bach and Schmidt, 2007). In the case of an oil film, these passages through the film are relatively few, according to the findings of Kampa et al. (2014), and probably formed close to the largest pore openings of the filter media, which offer the least resistance to the air flow. The exact geometry of these openings is not known however, and one probably has to account also for filter fibers in the vicinity of the pores, which could also play an important role in the deposition process. Fig. 8.5 shows that a film on the upstream side of the filter (i.e. for non-wettable media) leads to a higher deposition efficiency than on the downstream side, because the free-flowing aerosol is "injected" into the fibrous media with a multiple of its face velocity, compared to the more "gentle" deflection inside wettable media as the air is trying to leave the filter. Impaction-type separators using the deceleration of an aerosol jet on the surface of fibrous media are already widely used in industrial devices (e.g. Holm, 2001; Janakiraman et al., 2011).

Fig. 8.6 summarizes the results for channel layers, with the two coarse grade media shown in the upper figure, and the two medium grade media below. Since the data were derived from sandwiches with different numbers of layers, the values for multiple channel layers are averaged for each medium and shown as penetration for one layer. The underlying assumption is, of course, that this averaging is permitted because the saturation levels in the channel region are very uniform (compare Fig. 8.4). Each figure thus shows the penetration for an average channel layer in steady state and the corresponding penetration P_0 of the dry sandwich, plus the 1st layer penetration for the wettable media.

These curves are not as straightforward to interpret as those of Fig. 8.5 for the film penetration. One common feature is the location of the most penetrating particle size (MPPS) in the vicinity of 100 nm for all media, which changes little between dry and wet state (see also Section 8.4.3). Effects to the left of the MPPS can therefore be interpreted as being due mostly to changes in diffusion deposition, whereas deposition to the right will be affected by changes in inertial deposition.

The second feature to note is that non-wettable media show little or no change in layer efficiency when channels have formed. The efficiency loss is on the order of 10% or less. Interestingly, the loss in efficiency is a bit more pronounced for the medium grade filter than for the coarse filter, although its channel saturation (Fig. 8.4) is lower.

By comparison, wettable media are much more strongly affected by oil accumulation, especially the first layer which has a substantially higher saturation than the channel region (on the order of 3x). This leads to a higher interstitial air velocity in the 1st layer, which reduces the residence time for particles, and therefore also the diffusion efficiency, but increases the inertial impaction. Note also the crossover around 450 nm between $P_{1st\ layer}$ and P_0 of both filter grades, which seems to support this interpretation and points to an especially strong enhancement effect on the inertial side of the penetration curve. It is likely, that this further enhancement comes from a very non-uniform distribution of liquid in Layer 1 due to the formation of local accumulations of liquid, "pools" that have not yet found their way into the channel structure of subsequent layers. Not unlike films discussed earlier, these accumulations of oil cause further, very significant local accelerations of the air flow, and thus a strongly enhanced inertial deposition. In fact, the small cusp in the Δp curve at the boundary from Layer 1 to Layer 2 (Fig. 8.3) is evidence for the transition from very heterogeneous liquid pools to a channeled oil transport taking place in the 1st layer. We shall return to this point later in this paper in conjunction with Fig. 8.10.

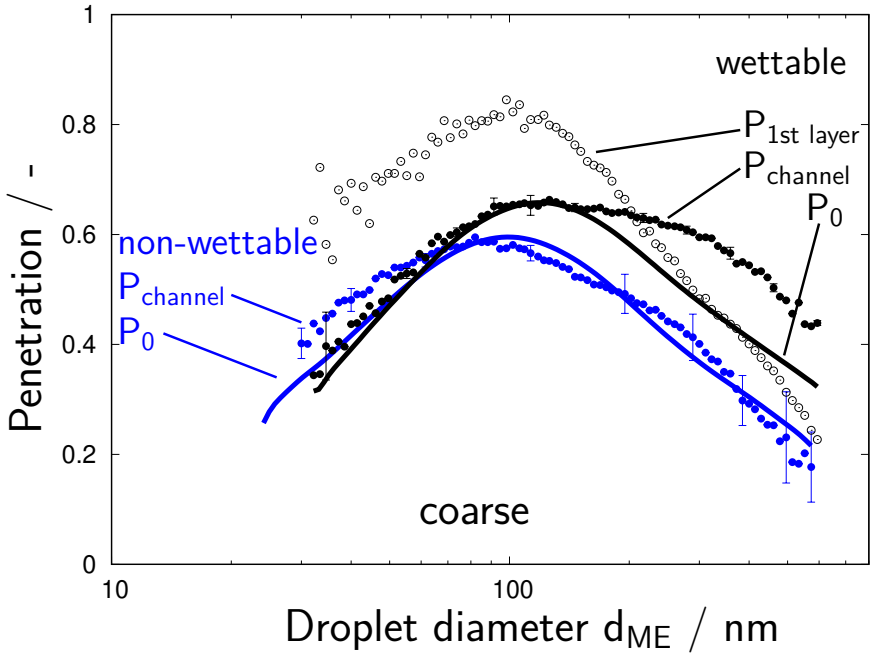

(a)

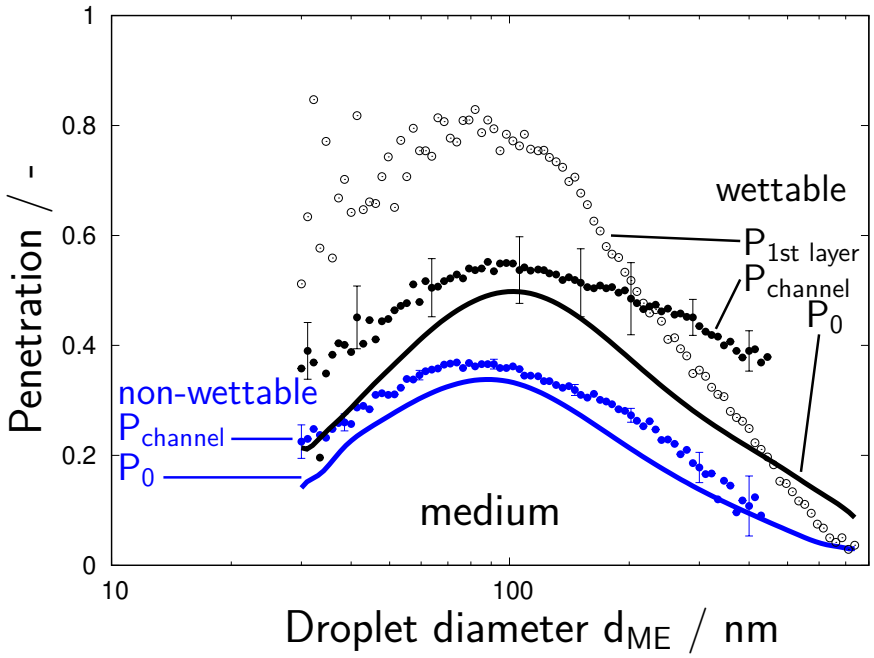

(b)

Figure 8.6: Steady-state penetration curves for a single (average) channel layer of a filter sandwich composed of coarse (top) or medium grade (bottom) media. Also included are penetration curves for the dry filter (P_0) and – in case of wettable media – for the 1st layer. Error bars represent the standard deviation of multiple measurements with different numbers of layers.

The same reasoning – namely a flow velocity effect – can be applied qualitatively to the channel region of the wettable media, where one would expect to find similar trends as in Layer 1, although somewhat weaker because the channel saturation is a fraction of that of Layer 1. Unfortunately however, the loss in efficiency observed in Fig. 8.6 for the channel layers is noticeable for all particle sizes. Moreover, the gap between P_0 and $P_{channel}$ seems to widen toward larger particles, where there is no crossover and no enhancement effect due to the flow velocity.

Such an unexpected behavior on both sides of the MPPS was reported already by Payet et al. (1992), who attributed it mostly to the loss of "efficient" fibers due to oil accumulation, not to a flow velocity derived effect. However, such a loss of fiber occurs just as well in non-wettable media, where we find almost no changes in efficiency. One therefore has to develop more refined explanations for the observed changes in penetration in the channel region of wettable and non-wettable media, possibly including also the microstructure of oil accumulation on fibers. Due to a higher contact angle, oil on non-wettable fibers occupies less fiber space than on wettable fibers (Mead-Hunter et al., 2014; Conder and Liew, 1989). A uniform oil film along the fiber – which does not exist according to Mullins and Kasper (2006) – actually represents the worst case in terms of efficiency loss. Single fiber theory also suggests that the more non-uniformly oil is distributed along a fiber, the more efficient the fiber becomes. Following the reasoning of Payet et al., with regard to effective fiber loss as an important and perhaps predominant reason, these subtler effects of oil distribution on the microscale could provide a basis for future, more quantitative theoretical analyses of efficiency loss in wettable and non-wettable filter media.

8.4.2 Predicting the efficiency of a multi-layer filter sandwich from the "regional" penetrations

In Section 8.3 we have developed a meso-scale efficiency model for wet oil mist filters that breaks down the global filter penetration into the contributions by specific filter regions, namely channels and films (plus that of the 1st layer, in case of wettable media). These "regional" contributions P_{film}, $P_{channel}$ and (where applicable) $P_{1st\ layer}$ were each calculated from a data set consisting of 2 (or 3) measurements of the global filter penetration curve with sandwiches of different thickness. We now proceed to test the accuracy of that model in predicting the global efficiency for arbitrarily many identical filter layers.

These tests were performed with a wettable and a non-wettable coarse filter medium, for which the respective regional penetration values had been measured

according to the method described in Section 8.3.2. Only the coarse media were selected because otherwise it would be impossible to obtain reliable downstream concentration data for more than a few layers. The results are shown in Fig. 8.7 for up to 8 layers. Evidently, the agreement is generally very good. In fact it is much better than the alternative of treating all layers as functionally equal (Fig. 8.7c). In that case, the penetration per unit layer P_1 would be calculated simply by taking the appropriate root of the measured overall penetration P, for example $P_1 = S^{1/m}$ in case of an m-layer sandwich, and then scaling up for arbitrary layer numbers n by powers of $(P_1)^n$. Of course, the difference shrinks with increasing number of layers, because the relative contributions of film and 1st layer diminish for thick sandwiches.

A side effect of increasing channel number seen in Fig. 8.7b is the formation of a "shoulder" in the efficiency curve of wettable media. The shoulder is due to the loss of efficiency to the right of the MPPS already noted in Fig. 8.6, and the dominating effect of the channel region with increasing n.

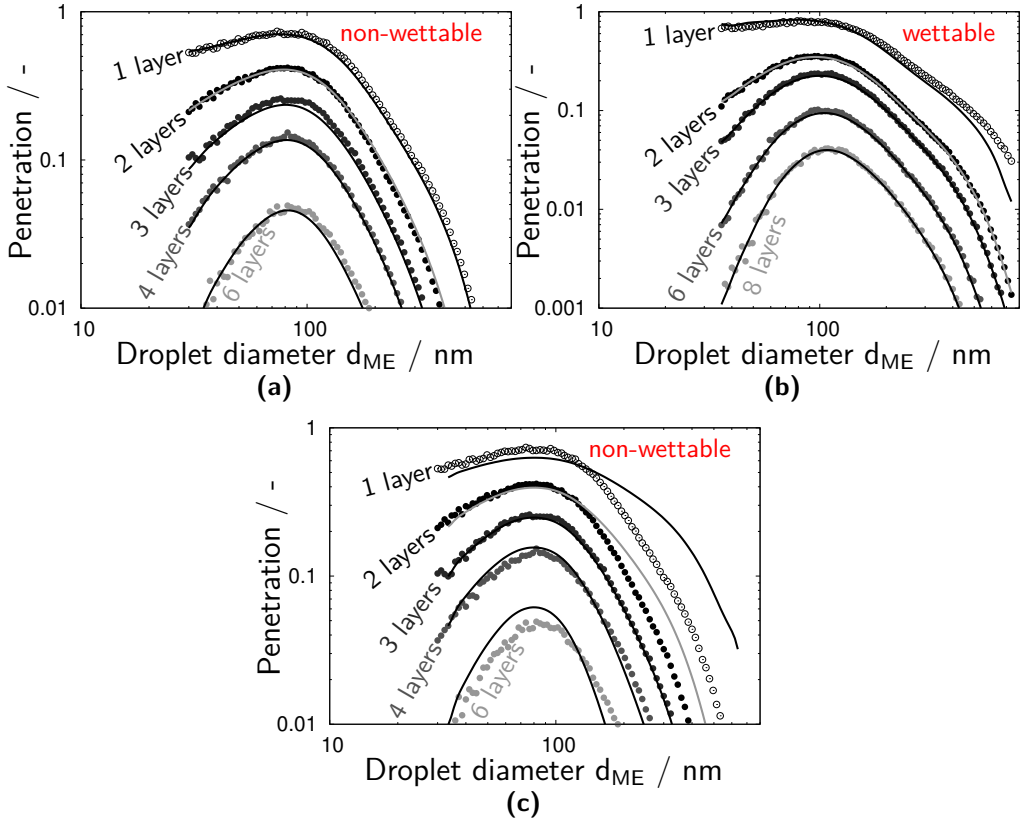

Figure 8.7: Measured (data points) and calculated (solid lines) penetration of non-wettable (a, c) and wettable (b) filter sandwiches. The calculation for (a) and (b) is based on the fractional efficiencies given in Figs. 8.5 and 8.6. The calculation of (c) is based on measurements of the 3 layer sandwich.

8.4.3 Shift in MPPS between dry and wet media

Efficiency measurements for oil mist filters (including also glass fiber media) are readily available in the literature. Many such data show a shift in MPPS toward smaller particles as the filter transitions from dry state to oil loaded in steady state (Raynor and Leith, 2000; Agranovski et al., 2001, 2002; Charvet et al., 2010; Mead-Hunter et al., 2014). Such a shift in MPPS "to the left" is commonly associated with a decrease in the diffusion efficiency and an increase in inertial efficiency. This can indeed be caused by an increase in flow velocity and this explanation is usually also offered in the case of oil loaded mist filters. (Note our discussion of this issue in the context of Fig. 8.6.)

We also see such an MPPS shift in our experiments, provided the media are not too efficient (in which case accurate penetration curves become rather difficult to obtain). Insight into the underlying causes can be obtained from Fig. 8.8, which shows penetration curves for both a wettable and a non-wettable filter in three consecutive stages of filter loading: dry (blue) – an intermediate state (black) – and finally in steady state (red).

Specifically, the figure intends to highlight the change in penetration between immediately before and after film formation. Note that for a non-wettable filter, the film forms up front, i.e. between dry and intermediate state measurement; for a wettable filter at the rear between intermediate and steady state. And the *shift in MPPS to the left* coincides with the film formation (which is essentially an inertial separator), either at the beginning or the end of the loading process, depending on the media. It is not the direct consequence of an increased flow velocity, because the flow velocity has already increased before (in case of wettable media) or has not yet occurred (non-wettable media). On the other hand, *the vertical shift in the MPPS efficiency* occurs due to channel formation which causes a loss of fibers.

8.4.4 Downstream total number concentration during oil loading

The evolution of the total downstream number concentration from the dry to the steady state (i.e. the absolute penetration) has repeatedly been used as a criterion for the deterioration of filter efficiency with increased liquid loading and provides valuable information about this process (Contal et al., 2004; Frising et al., 2005; Patel et al., 2012). Such measurements are relatively easy to do and avoid problems with SMPS measurements due to rapidly changing

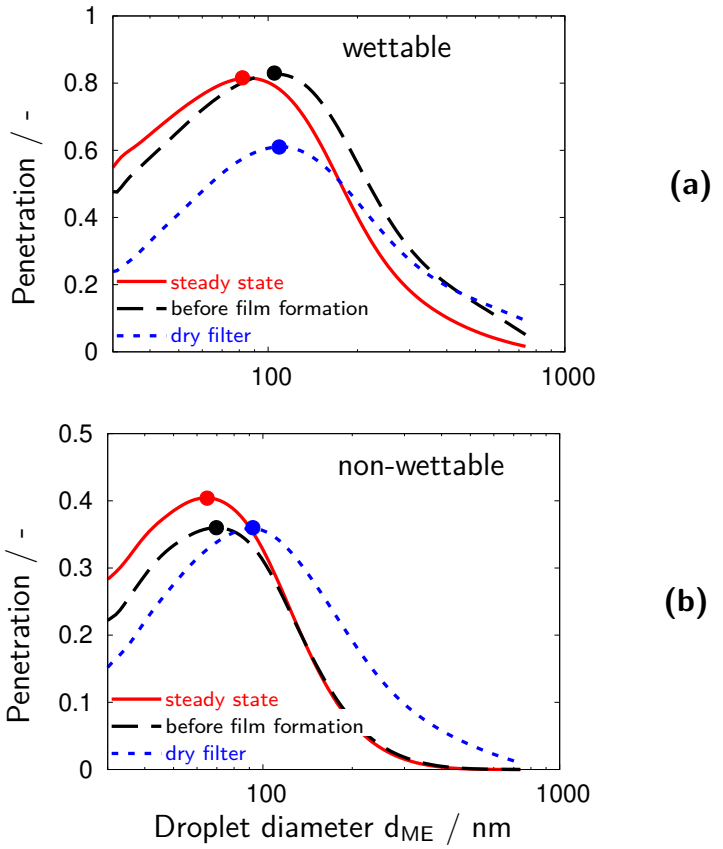

Figure 8.8: Penetration at different stages of loading of 3 layers of medium grade wettable and non-wettable media. For better visibility, the colored dots mark the MPPS and its shift.

efficiencies. The only assumption required is a constant inlet size distribution and concentration.

In essence, the evolution of the downstream aerosol concentration during filter start-up should mirror the changes in penetration related to the various stages of channel and film formation that were discussed in the preceding parts of this paper. Fig. 8.9 presents measurements of the absolute downstream concentration as a function of time for a medium and a fine grade *wettable* filter. They were made by CPC at very constant inlet concentrations and stopped shortly after reaching steady state. For the sake of clarity, only the curves for 1 and 5 layers are included in the figure.

In discussing the data, it should again be kept in mind that (for any wettable filter medium) the channel formation precedes the film formation, which occurs at the very end of the loading process, immediately before reaching the steady state. In Fig. 8.9 the penetration therefore increases from the very start as channels proceed further and further into the filter, until the onset of film formation (marked as such in the figure), where the concentration decreases

markedly due to the added inertial deposition effects in the film. This is best visible in the curves for 1 layer, and of course more pronounced for the lower grade medium. The formation of this small cusp was first observed by Contal et al. (for wettable media). Our data confirm and explain the phenomenon.

With increasing thickness of the sandwich, the absolute penetration decreases and the cusp becomes weaker because less and less aerosol arrives at the film on the downstream side of the filter. It has practically disappeared for 5 layers of the media used here. It is therefore surprising at first, to see the strong up-turn in penetration for the most efficient filter (red curve; note that it has a separate y-axis) around the time of reaching steady state. However, this increase is not due to some unexpected changes in droplet separation, but rather to the re-entrainment of liquid into the air flow. This re-entrainment is caused by bursting bubbles in the liquid film of the filter. A detachment of droplets from fibers is unlikely because it requires air velocities several magnitudes above those used in our experiments (Wurster et al., 2015). Re-entrainment at face velocities below 1 m/s generates a broad spectrum of secondary aerosol including also droplets in the micron and submicron range (Wurster et al., 2015). By limiting the experiments in the previous sections to less efficient media of coarse and medium grade, the primary penetration outweighs the generation of droplets due to bursting bubbles. However, re-entrainment occurs for all media, but becomes visible only for more efficient filters where the direct aerosol penetration is not too high.

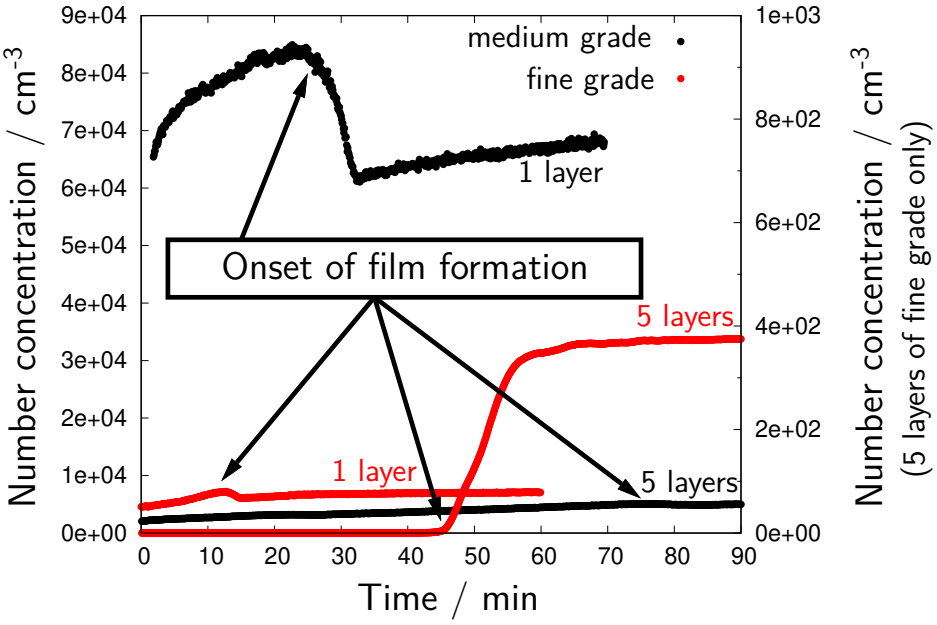

Figure 8.9: Downstream number concentration as a function of time during the various stages of loading for medium and fine grade wettable filters with 1 and 5 layers respectively.

The interpretation of total penetration data obviously requires prior knowledge of the inlet size distribution. This is true also for Fig. 8.9, where the formation of a cusp during film formation is predicated on the presence of particles large enough to be collected by inertial deposition. According to Fig. 8.5 this requires particles larger than about 100 nm. Fig. 8.10 illustrates how the penetration depends on particle size. For these measurements with coarse media, mobility-sized fractions of 40, 100 and 300 nm were selected from the downstream aerosol by DMA. The Δp (averaged for the three experiments) is also included in the figure. Note that Fig. 8.10 shows the relative penetration, i.e. the change of penetration relative to the start of each experiment, because this makes it easier to analyze changes in the shape of the curves.

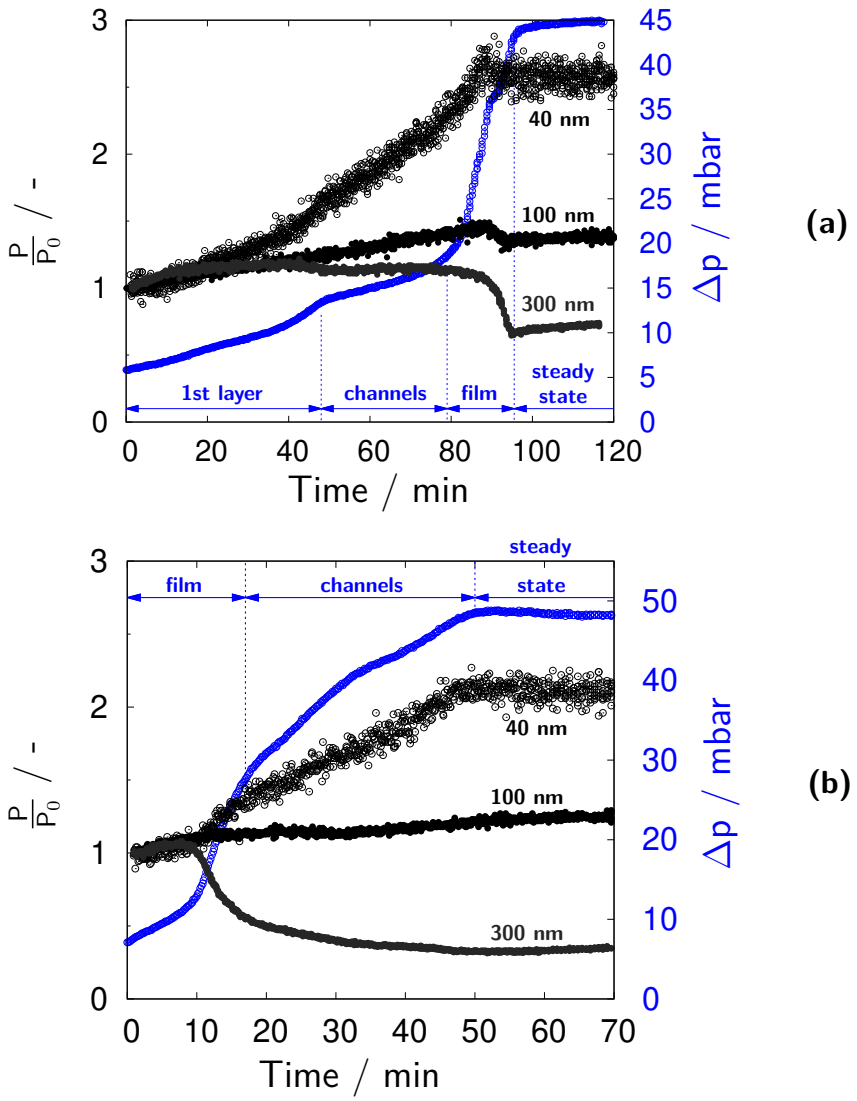

Figure 8.10: Penetration of 40, 100 and 300 nm droplets through 3 layers of wettable (a) and non-wettable (b) coarse filter media.

For 300 nm particles, the penetration shows a pronounced decrease during film formation, both for wettable and non-wettable media. However, this decrease becomes weaker for smaller particles and has completely disappeared at 40 nm. Droplets in the MPPS size range around 100 nm are generally less affected by oil loading, as we had already seen from Fig. 8.6.

In conclusion, the total number concentrations can yield contradicting – but nevertheless accurate – results, depending on whether the aerosol upstream of the filter is situated predominantly on the right-hand or the left-hand side of the MPPS.

8.5 Summary and conclusions

Kampa et al. (2014) modeled the differential pressure Δp of an oil loaded mist filter by separating it into regions where the liquid is organized either in the form of a thin film, or in the form of parallel liquid channels, and by identifying the individual contributions of each region, termed Δp_{jump} and $\Delta p_{channel}$, to the total Δp on the basis of experiment. As a very useful practical consequence of this Jump-and-Channel-Model, the total Δp of a multi-layer filter sandwich can be described by the sum of the individual contributions by Δp jumps and channel layers.

This mesoscale model is now applied to the efficiency, or rather the filter penetration, which is modeled as the product of the penetrations associated with the various characteristic regions of the internal liquid distribution. Based on measurements of the internal saturation it is shown that non-wettable filter sandwiches can be subdivided into two characteristic regions, a very thin film on the upstream filter face and a channel region that extends through the remainder of the layers. Wettable filters are composed of three characteristic regions, a first layer (which acts primarily as coalescence and feeder layer with a rather high saturation), an extended channel region, and a thin film on the downstream filter face. Accordingly, the unit penetrations are P_{film}, $P_{channel}$, and (in case of wettable media), $P_{1st\ layer}$.

A method is described to derive these unit penetrations from a set of measurements. Experiments are then carried out with filters composed of multiple layers of conventional glass microfiber media, both wettable and non-wettable to compressor oil, in which the fractional penetration of the entire sandwich was measured by SMPS between about 30 and 700 nm.

It is shown that the film functions essentially as an inertial separator that reduces the penetration for particles larger than about 100 nm substantially, in comparison to that of the dry media. The channel penetration is generally higher compared to a dry filter, both on the left and right side of the MPPS, probably because of a loss of active fibers in the partially saturated media. There are slight differences with regard to wettable and non-wettable media in this regard, probably due to the way oil accumulates around wettable and non-wettable fibers. Interpreting such detail will however require further studies, perhaps along the lines of single fiber theory.

It is shown furthermore, that the proposed decomposition of the total fractional penetration into the respective "building blocks" P_{film}, $P_{channel}$ etc. permits an accurate prediction of the behavior for filters with arbitrary layer number.

As a further practical consequence, our efficiency model can explain earlier observations related to the efficiency of mist filters, such as a shift in MPPS during loading, as well as characteristic variations in downstream aerosol concentration while the filter transitions into steady state. Some authors (Kampa et al., 2014; Mead-Hunter et al., 2014; Agranovski et al., 2001) investigated composite filters of wettable and non-wettable media which might result in the presence of several liquid films on a single filter. However, a detailed study is needed in order to investigate the impact of multiple combinations on the efficiency of such filters.

Additional measurements of the total downstream concentration as a function of time are presented, which show that these changes coincide with the formation of the film and its function as an inertial separator. Moreover, it is shown to depend on the upstream size distribution, whether such a change becomes visible in the downstream aerosol spectrum.

For high-efficiency sandwiches it was also possible to identify the onset of re-entrainment.

Acknowledgement

The authors would like to thank Atlas Copco Airpower n.v. for funding and continued interest in this work, as well as BinNova GmbH for providing us with wettable glass fiber media investigated in this paper.

9

Transitional phenomena during continuous long-term loading and discontinuous filtration[1]

Abstract

This paper addresses the phenomenon of a slow Δp increase ("creep") sometimes observed in mist filters during their so-called steady-state operation, especially at relatively high flow rates and aerosol loads (Kolb et al., 2017). This creep phenomenon draws into question the concept of steady state and awaits a physical explanation on the basis of more systematic data. The present study was performed with conventional glass microfiber filter media at filter face velocities in the range of 1 to 70 cm/s, using submicron oil aerosol at loading rates up to 1.1 g/(m^{2}s). Experiments started either with a dry filter (designated as S_0=0, where S stands for the liquid saturation level), or with a completely pre-saturated filter (designated as S_0=1). The S_0=0 runs reached "steady state" (defined here as the onset of drainage) after approximately 0.3 hours and were then loaded continually for another 100 h. Runs starting at S_0=1 reached a steady state very quickly.

[1]This article was published as: Kolb, H. E. and G. Kasper (2019). *Mist filters: How steady is their "steady state"?*, Chemical Engineering Science 204, 118–127.

With regard to Δp, all filters featured Δp creep when starting from S_0=0. For coarse filter grades, Δp creep effectively ended in less than 40 hours at moderate flow velocities; finer grades crept further and did not stop creeping within any reasonable loading time. When starting from S_0=1, a steady Δp endpoint was reached rapidly, but was considerably higher than the level attained by creep. It was further shown that creep is associated with a slow increase in the saturation level and that S approached the (higher) level of pre-saturated filters. The increase in S during creep was associated with the formation of additional fine oil channels. Conversely, oil channels were completely absent in pre-saturated filters and the liquid was uniformly dispersed. Using simple theoretical considerations for flow in porous media, the observed differences in Δp are explained in part by the difference in S between S_0=0 and S_0=1 filters, and in additionally also by taking into account the different liquid distribution patterns.

We conclude that the onset of drainage under steady external conditions – the stage conventionally viewed as the beginning of steady-state operation – does not automatically represent an internal steady state with regard to saturation levels or pressure drop; and presumably also not for the oil distribution pattern. The internal saturation reaches a stable endpoint sooner than the pressure drop, which may continue to creep for the lifetime of the filter. If and when a transition from channel patterns to homogeneous oil distribution occurs during steady operation is not known. However, the transition can be forced rather quickly by operating the filter intermittently at a very low flow velocity.

Keywords: Filtration, oil mist, coalescence filter, pressure drop, steady state

9.1 Introduction

Filtration of oil droplets ("mist") from gases by fibrous media is a common practice for many industrial applications such as metals cutting, the exploitation of natural gas, crankcase ventilation or oil-lubricated screw compressors. As opposed to dust filters, which show a continuous increase in differential pressure, Δp, with dust load, mist filters are widely accepted to reach a steady state, wherein the liquid loading rate equals the liquid removal rate (by drainage and/or re-entrainment) so that Δp as well as filter efficiency, E, become constant over time (Liew and Conder, 1985; Agranovski and Braddock, 1998; Frising et al., 2005; Charvet et al., 2010). These steady-state filter properties are related to the oil distribution inside the filter as best described by the so-called Film-and-Channel-Model (Kampa et al., 2014; Kolb et al., 2018).

Exceptions to the concept of steady-state operation have been reported in the scientific literature, notably when the oil aerosol is mixed with solid particles that tend to accumulate in the filter and lead to a further rise in differential pressure (Bredin and Mullins, 2012; Frising et al., 2004). Also, a temporary interruption of the air flow is known to increase the steady-state Δp after flow resumes, but without increasing the saturation (Frising et al., 2005; Callé-Chazelet et al., 1996). During a flow interruption the liquid apparently re-arranges itself due to capillary forces inside the media, provided it is given enough time. Bredin and Mullins (2012) also studied on-off operation, although with a pre-saturated stainless-steel filter (see also further down), and found that repeated flow interruptions lead to a steady Δp and apparently also an increase in saturation.

Leaving aside solid contaminants or on-off operation, the bulk of experimental literature on mist filtration relies on *continuously and steadily operated* filters to study the evolution of Δp with time. Unfortunately, this literature is far from unequivocal with regard to the existence of a constant steady-state Δp under unvarying (i.e. steady) operating conditions, in this case primarily the conditions of flow and filter loading. Published data for all kinds of filter grades and types of wettability often show that the so-called steady-state Δp curves are not really flat, even for clean oils, but exhibit a slight upward tendency called "creep" (e.g. Contal et al., 2004; Frising et al., 2005; Mead-Hunter et al., 2013; Kolb et al., 2017; Chang et al., 2018a). Possible explanations for such a Δp creep include changes in media properties (such as wettability) with time, a gradual rearrangement of the internal liquid distribution, a change in saturation, operating conditions that are not truly steady, or even a combination of these effects.

Oil mist filtration experiments typically start out with dry media. Since dry filters may take an excessive amount of time to reach steady state under typical steady operating conditions, the filters are occasionally pre-saturated and then blown out at the beginning of a test. Bredin and Mullins (2012) report that the Δp for blown-out filters converges readily to the steady-state Δp obtained when starting with dry media. On the other hand, Kampa (2015) in his experiments (see Fig. 2.13 therein) found no convergence between the two operating modes. The main difference between the two experiments was the grade of the filter media. It is not clear at present, whether such accelerated testing protocols generally lead to identical endpoints for Δp. In the context of Δp creep a further question arises, as to whether on-off operation or pre-saturation represent effective short-cuts for the creep phase.

In sum, the various phenomena surrounding Δp creep are currently not well researched, let alone understood with regard to the underlying mechanisms.

As a side effect, the terminology found in the literature to characterize the susceptibility of mist filters to changes in Δp during nominally steady operation is not consistent either. Common terms are "quasi-steady" (Wurster et al., 2015; Chang et al., 2018a), "pseudo-stationary" or "pseudo-steady" (Contal et al., 2004; Callé-Chazelet et al., 1996; Mead-Hunter et al., 2013, 2014), with some authors using both prefixes interchangeably (Chang et al., 2017, 2018a). Authors seldom communicate the reasoning behind a given choice and may in fact wish to designate different phenomena. Wurster et al. (2015) introduced the term "quasi"-steady for pressure drop measurements fluctuating around their mean value. Mead-Hunter et al. (2014) use "pseudo"-steady to characterize the case of liquid re-arrangement during non-steady operating conditions. On the other hand, Frising et al. (2005) apply the same term to a slow increase in Δp and efficiency when operating parameters are unvarying, in other words to the concept of Δp creep in the narrower sense of this paper. Since none of these terms are without ambiguity, and rather than introducing yet another variant, we shall in the following retain the traditional designation of "steady" for the state of a filter when its differential pressure levels off just after the onset of drainage, even if Δp does not become exactly constant but continues to "creep". We do assume however, that the external filter operating conditions such as flow and loading rate, temperature, etc. are sufficiently constant so as not to affect the ensuing observations.

Kolb et al. (2017) first reported (for a single type of glass microfiber filter medium) that Δp creep can be intensified by higher flow rates and aerosol loads. Fig. 9.1 reproduces key data from that paper in a slightly different representation to illustrate this point: Fig. 9.1a shows the wet pressure drop (in other words the increase in Δp above and beyond the Δp_0 of the dry filter) as a function of filter face velocity v at constant loading rate R; Fig. 9.1b as a function of loading rate R at constant v. While the pressure drop appears to level off sharply with the onset of drainage – the point commonly interpreted as the beginning of steady state – it does not really remain constant with continued operation. Apparently the Δp creep is more pronounced at the highest technically achievable v and R. Although Δp shows signs of leveling off even at the highest velocities and loading rates, an asymptotic level for the creep phase was not found after 1100 hours of continuous loading.

Since we are not aware of any systematic investigations of creep beyond the exploratory work by Kolb et al. (2017), that paper can be seen as a starting point for the present work. Their experiments generated considerable experience in operating oil mist filters under very constant loading conditions during many hours and days. However, they were limited to a single type of wettable filter media and left many open questions. For example, simple reasoning would

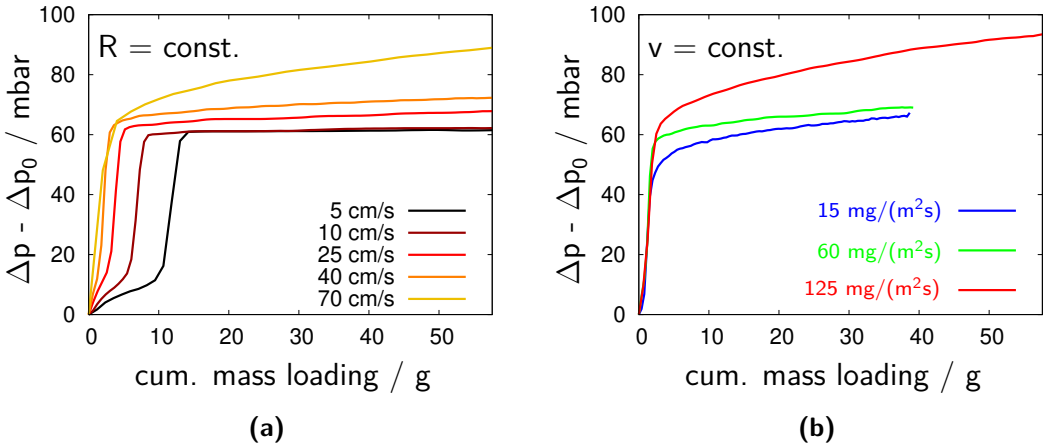

Figure 9.1: (a): (a): Illustration of Δp creep for different filter face velocities at a constant loading rate R = 125 mg/(m^{2}s). (b): Δp creep for different loading rates at a constant face velocity v = 70 cm/s. (Data adopted from Figs. 3a and 9a of Kolb et al. (2017) and replotted vs. cumulative mass loading instead of absolute time)

suggest the existence of an asymptotic level for Δp creep. It remained unclear where it would lie under conditions of continuous steady loading, how it could be predicted, or how it might depend on the media structure. It was not even clear whether creep was a universal phenomenon or somehow related to a certain, yet unknown structural property of certain types of filter media.

The work described in this paper was designed first of all to expand the phenomenological picture, by experiments with filter media of different types (both wettable and non-wettable to compressor oil) and degrees of fineness (coarse – medium – fine), and loading them with oil aerosol for fixed periods of time of 100 hours each, which is far beyond reaching steady state = the onset of drainage. This is several hundred times longer than the time required for the filter to reach steady state (about 0.25 h), but still represents a compromise with experimental economy. Aside from measuring changes in Δp during this steady state, the concurrent evolution of the layer-by-layer saturation S as well as the re-arrangement of oil within individual layers were investigated as possible causes for creep. Additional experiments were conducted with pre-saturated media to identify a possible asymptotic endpoint of the creep. The experiments cover a range of face velocities up to 70 cm/s and loading rates between 60 and 1100 mg/(m^{2}s).

9.2 Experimental materials and methods

Filter media and filter assembly:
Wettable glass microfiber media were selected across a broad range of grades ranging from coarse, open pore structures to fine media with relatively thin fibers and small pores (Table 9.1). The media were relatively uniform in terms of thickness and porosity. Porosity and thicknesses were measured by means of a balance and a caliper, whereas pore sizes were analyzed by a capillary flow porometer and silicone oils as a wetting liquid (Kolb et al., 2018). Fiber diameters were calculated according to the Davies (1973) formula.

The media were cut into uniform squares of 8 x 8 cm each and assembled into multi-layer filter sandwiches. The number of layers depended on the overall thickness of the resulting sandwiches and is indicated for individual experiments as needed. Filter sandwiches were clamped in a filter holder and mounted vertically.

Medium	Fiber diameter / µm	Largest pore/ µm	Mean pore/ µm	Porosity/ -	Thickness/ mm
wettable					
coarse 1	4.0	37.2	13.4	0.939	0.64
coarse 2	3.7	47.1	16.5	0.950	0.42
medium	2.9	32.9	8.5	0.934	0.51
fine	2.2	28.3	6.8	0.938	0.51
non-wettable					
coarse	3.0	34.8	11.4	0.950	0.79
fine	1.9	22.3	5.1	0.943	0.51

Table 9.1: Capillary and structural properties of the filter media. The wettable fine medium is of the same grade (although from another batch) as the medium investigated by Kolb et al. (2017).

Filter test rig and aerosol generation:
As seen in Fig. 9.2, a horizontal test rig was used to load the filter sandwiches with oil aerosol. The system was regulated to maintain a constant filter face velocity within the filter holder. Pressure drop, temperature, and cumulative drained oil mass were recorded every 5 seconds or more frequently when needed. Most of the hardware features were already described repeatedly, e.g. by Kampa et al. (2014) and Kolb et al. (2017) and the reader is referred to those publications for further technical details.

Submicron oil aerosol was generated with a Collison type nebulizer (May, 1973). In contrast to previous publications, this work required higher loading rates over a longer period of time. This was achieved by operating up to 18 parallel nozzles, which allows oil loading rates up to 35 g/h. In order to prevent the

system from running out of oil during long-term experiments, the liquid level within the nebulizer was kept constant by means of an electronic level indicator and an external pump. The aerosol was generated from typical compressor oil with a viscosity of 122 mPa s and a surface tension of 31 mN/m at 20°C. The aerosol had a number-mean diameter of about 640 nm and a roughly log-normal size distribution with a geometric standard deviation around 1.9.

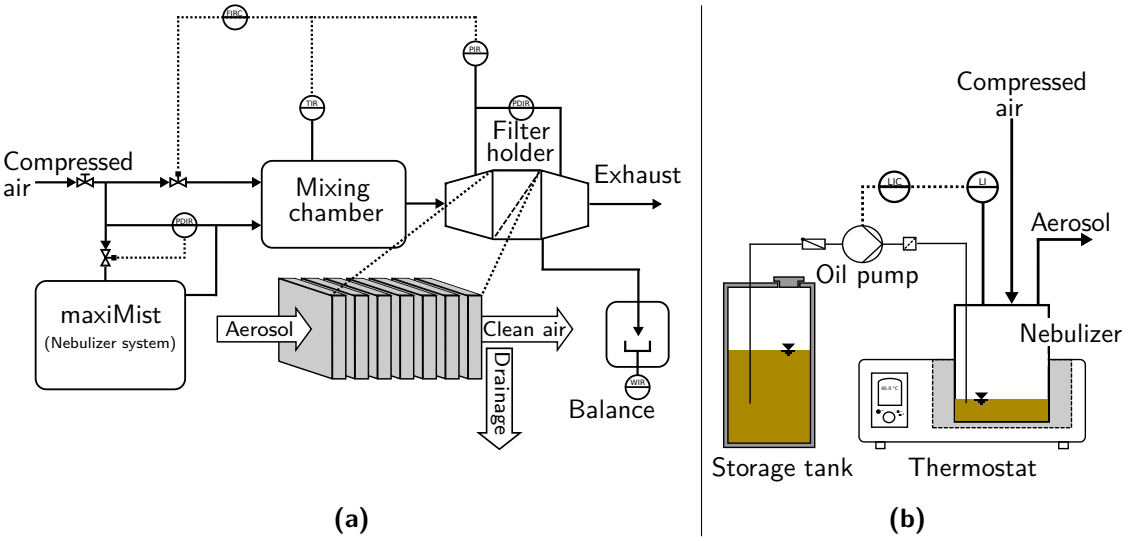

Figure 9.2: Schematic diagram of the experimental set-up for the long-term loading of stacks of flat filter media layers (a). Nebulizer system with controllable oil level for long-term experiments at oil loading rates ranging from 1 to 35 g/h (b).

Procedures for a typical experiment:
Experiments were conducted in one of two ways, starting either with a new and dry filter sandwich, or a completely pre-saturated filter sandwich. The former experiments are designated in short as S_0=0, the latter as S_0=1 where S_0 stands for the saturation level at t=0.

Filter loading starting from S_0=0: Layers were weighed individually before stacking and clamping them into the filter holder. Before starting to load the *initially dry* media, the face velocity was adjusted and the dry Δp was measured. Subsequently, the aerosol generation was switched on and loading took place at a constant, predetermined rate of 1.1 g/(m^{2}s) for 100 hours. The saturation of each layer was calculated at the end of an experiment, after dismounting and disassembling the sandwich promptly and re-weighing each layer. Also, photographs were taken at that stage, to enable investigations of the liquid distribution within each layer.

Filter loading after complete pre-saturation (S_0=1): Dry layers were immersed individually in compressor oil and saturated completely under a vacuum for at least 2 hours to remove all air bubbles. They were then

assembled carefully into sandwiches without air gaps between the layers. Experiments began by switching on the aerosol flow at its final value while increasing the air flow in pre-determined steps until the nominal face velocity was achieved. This results in a "soft" decline of saturation from 100 % initial to some lower level without raising the maximum value of Δp significantly above the steady-state Δp. By using this procedure steady values of Δp are attained very quickly, whereas abruptly blowing out the filter ensues a creep phase or may even result in bursting the filter media or parts of the equipment. The experiments ended when Δp did not change noticeably within 10 hours.

9.3 Results and discussion

9.3.1 Pressure drop: long-term evolution (S_0=0) vs. pre-saturation (S_0=1)

Long-term experiments for Δp are shown in Fig. 9.3. For practical reasons they were limited to 100 hours of continuous operation at a face velocity of 25 cm/s and a loading rate of 1.1 g/(m^{2}s). Curves for S_0=0 are designated as coarse 1 and 2, medium and fine, according to the media shown in Table 9.1. The time axis is logarithmic, which creates some distortion of the curve shape, but reveals both the short-term and the long-term behavior. Note also, that Fig. 9.3a shows total pressure drop of the filter, while Fig. 9.3b shows pressure drop Δp^* as defined below.

At the loading rate of 1.1 g/(m^{2}s) film formation on the downstream side of the sandwich (the steep increase in Δp) is evidently completed within the first 0.3 hours for all filters. This coincides with the point in time when the filter transitions into steady state and is marked by a circle on each curve. This circle represents the origin of a new coordinate system for Fig. 9.3b. Δp^* thus represents the creep-Δp and – since the time axis is now linear – its evolution now resembles more closely that of the Δp-creep of Fig. 9.1.

A common trait of all media is the gradual slowing down of the Δp-creep with loading time. The loading curves for coarse media become effectively level between 20 and 40 hours of operation and with a very modest increase in Δp^* of a few mbar, whereas finer media do not only creep further in absolute terms but also continue to creep noticably beyond the time limit of 100 hours. Aside from giving a first indication of the relationship between magnitude of creep and media structure, Fig. 9.3 raises the question of the asymptotic level of

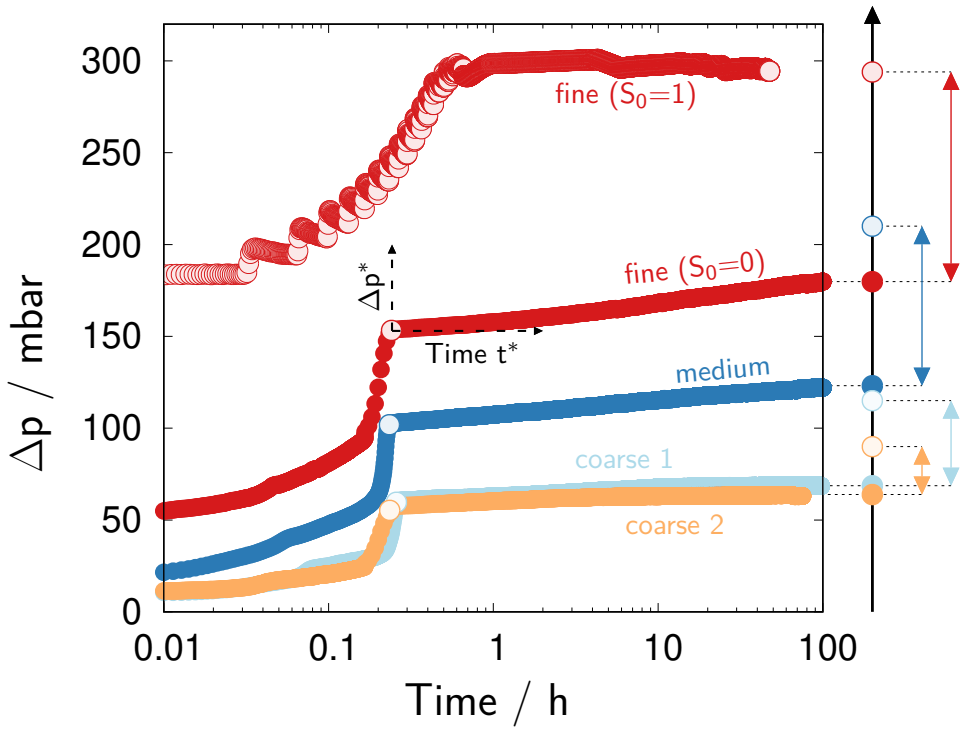

(a) Loading curves of initially dry media (S_0=0) at constant face velocity of 25 cm/s and oil loading rate of 1.1 g/(m^2s). Δp values for pre-saturated media (S_0=1) are included on the right-hand margin, along with final Δp after 100 h.

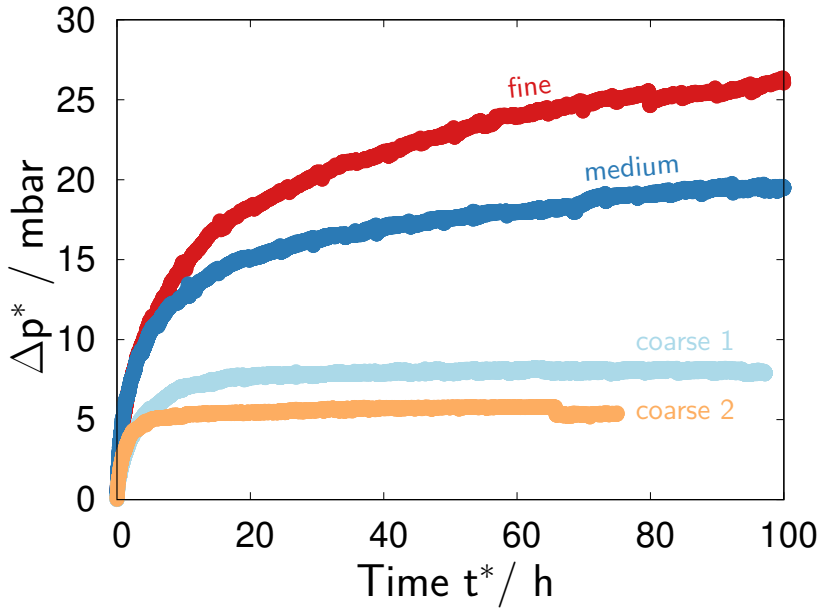

(b) Δp creep represented by Δp^* vs. time t^* as defined in the top graph.

Figure 9.3: Evolution of Δp creep and comparison with pre-saturated media.

Δp for S_0=0, which we will from now on call Δp_{end}. Could it be that Δp_{end} coincides with the steady value of Δp attained for pre-saturated filters, i.e.

experiments with S_0=1?

The evolution of Δp for a pre-saturated medium (S_0=1) is also included in Fig. 9.3a, but only for the fine medium. The multiple small steps in the graph within the first hour are due to the step-wise blowing out the excess oil. Endpoints for the steady Δp for all media obtained for S_0=1 are included on the right-hand margin of Fig. 9.3a. They are shown as circles color-coded to the respective media types. (Since these values are attained very quickly, it would not be useful to show the entire curve.) The colored arrows reflect the gap in Δp between S_0=1 and S_0=0 after 100 hours of continuous loading. Evidently, these arrows are rather short (but not negligible in terms of percentage!) for the two coarse media but become increasingly longer as the media get finer. If the endpoint for S_0=1 is representative of asymptotic Δp for creep, then the widening gap leaves little hope of a possible convergence of the two points within a feasible experimental time as discussed in detail later in this work.

Earlier observations of convergence in Δp between pre-saturation and steady state or creep (Bredin and Mullins, 2012 vs. Kampa, 2015) may have to do with the type of media investigated. Pre-saturation is a viable short-cut for long-term creep only in case of relatively coarse media.

9.3.2 Saturation and oil distribution (steady state – 100 hours – pre-saturated)

The evolution of the saturation profile corresponding to these Δp data is discussed next. Fig. 9.4 shows profiles that were obtained for 6-layer sandwiches composed of the medium "coarse 1", a medium which came reasonably close to reaching Δp_{end} during 100 hours of operation. Each data point represents the average saturation S in a given layer (and each profile requires a new experiment because runs cannot be interrupted to disassemble the sandwich!). Note that the profiles have a U-shape, of which the central layers (without the first and the last layer, which are functionally different) represent the channel region. The core region of the profiles becomes more and more flat with time. It is the region we are most interested in.

The first thing to note in Fig. 9.4 is that the saturation level in the core-region (Layers 2 to 5) is always significantly higher for the pre-saturated medium (about 40%) than for media loaded from the dry state. For the latter, S increases with loading time from about 20% just after reaching steady state to an apparently constant level of about 35% after very long times. The step changes in S become gradually smaller; average saturation levels for 15, 43

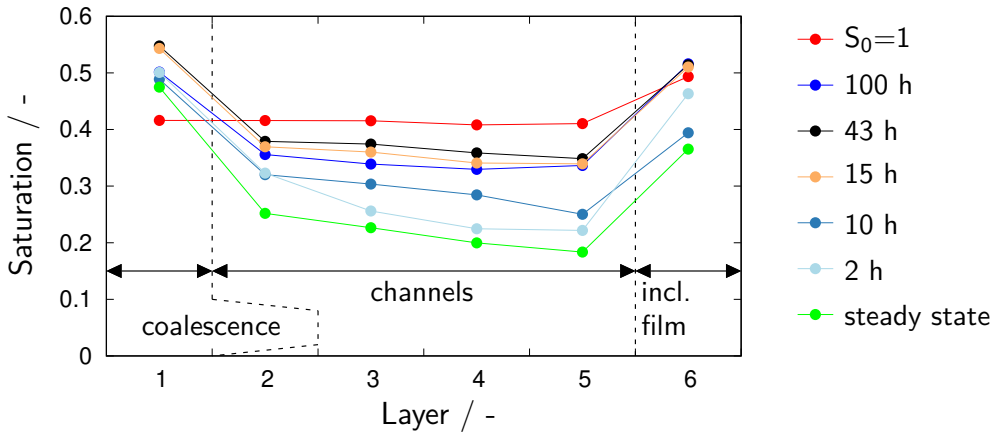

Figure 9.4: Evolution of saturation profiles for the coarse 1 medium at a constant face velocity of 25 cm/s and oil loading rate of 1.1 g/(m^{2}s). Each data point represents the average saturation of one filter layer.

and 100 hours that are practically indistinguishable when taking into account the variability in saturation between sandwiches, which is on the order of 5%. (Refer to Section 9.2 for details of the experimental procedure.)

This indicates clearly that the Δp creep is not (or not only) a rearrangement phenomenon, but due to an increase in oil content. Reasonable explanations for the continued accumulation of oil are newly-formed channels or – in the case of low-efficiency media – the continued deposition of aerosol droplets between the already existing channels in the depth of the filter. The next question to address is therefore, how the observed increase in oil content plays out in terms of oil distribution within filter layers.

Fig. 9.5 shows photographs of the **liquid distribution within a typical layer of the channel region**, (in this case of Layer 3 of the coarse 1 medium) obtained immediately after reaching steady state, after 100 hours of loading, and for a pre-saturated filter (S_0=1). Large white spots are the channels that have formed in the filter while reaching steady state.

Two features are of main interest in Fig. 9.5: Between steady state and 100 h of operation, there appear numerous small white dots between the larger and older channels, which might indeed be indicators of fresh oil transport paths. More striking however is the difference to the liquid distribution for S_0=1, where oil channels seem to be completely absent. Instead the oil must now be distributed homogeneously within the filter media, probably along the fibers. These differences in oil distribution at relatively similar saturation are obviously responsible for differences in pressure drop seen in Fig. 9.3 between 100 h and pre-saturated media: The more uniform the distribution the higher the Δp. Model calculations by Kolb et al. (2017) indicate that such variations in

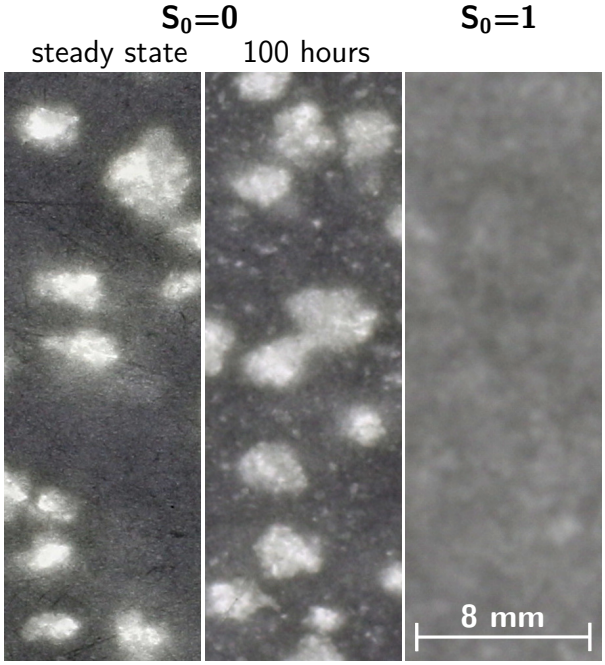

Figure 9.5: Liquid channels (bright spots) at different loading stages for initially dry media (left and center) vs. homogeneous liquid distribution of pre-saturated media (right). Reference was the 3rd layer of the coarse 1 media operated at a constant face velocity of 25 cm/s and oil loading rate of 1.1 g/(m^{2}s).

distribution may lead to a factor of roughly 2 in Δp.

Both the gradual accumulation of more liquid after the onset of steady state as well as the homogeneous liquid distribution for S_0=1 appear to be inherent characteristics of all investigated media. To support this, Fig. 9.6 shows ***separate saturation profiles for each of the four media*** investigated, both for S_0=0 (steady state and 100 h) and for S_0=1. We are again interested in the core region of the profiles which are unbiased by coalescence effects in the first layer, or the liquid film in the rear-most layer. In all four figures, the saturation levels at 100 h have approached those of the pre-saturated media and are unlikely to rise much further after that. It is thus reasonable to assume that the saturation level for S_0=1 is representative of the asymptotic saturation level for S_0=0.

A minor detail to address in Fig. 9.6 is the saturation in Layer 1, which is actually a little lower for S_0=1 than for S_0=0. This can be explained by an effectively better and faster oil transport inside a filter medium, once it has been pre-saturated completely. Presumably, the surface of pre-wetted fibers contains enough finely dispersed liquid that acts as a "flowing agent" for the movement of oil drops. Coalescing drops will therefore be transported sooner out of Layer 1 (i.e. as smaller drops) under the influence of the air flow than for S_0=0 conditions, where such oil drops have to grow larger. The net effect of this effectively enhanced wettability is a lower average saturation in the coalescence region of pre-saturation media. – Note however that this enhanced (apparent)

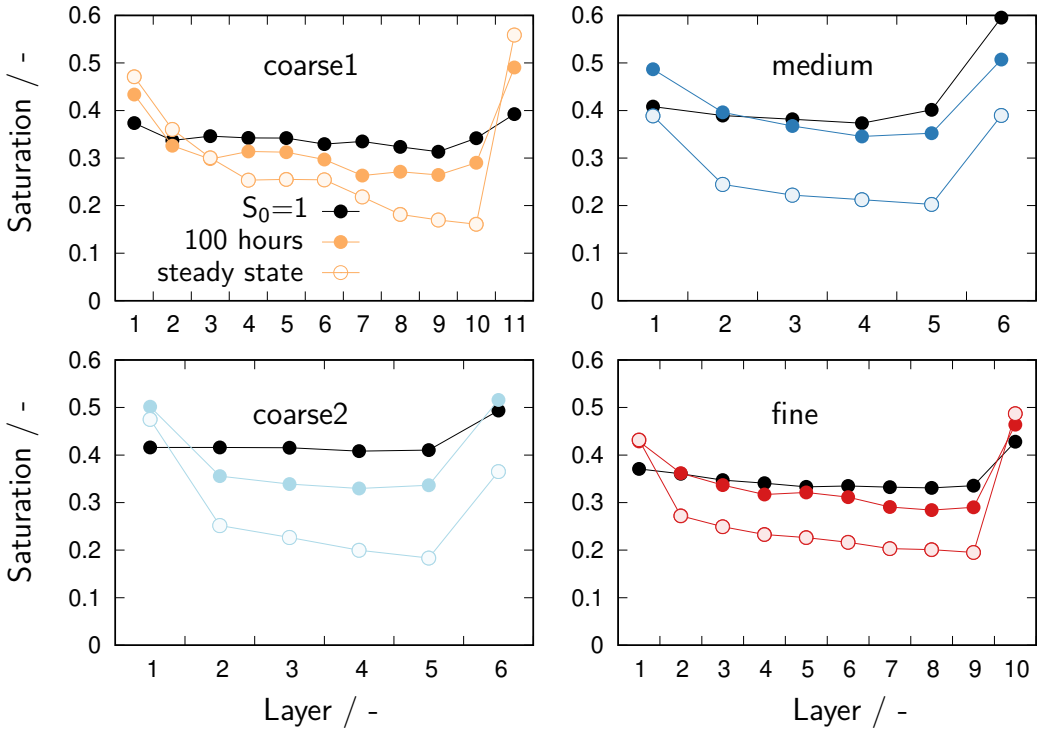

Figure 9.6: Saturation profiles of all four investigated media: Comparison between steady state, after 100 h of loading, and for pre-saturated media.

wettability of pre-saturated media disappears, if the filter is subsequently operated with dry air over long periods of time. The saturation also declines very slowly under such dry flow conditions. Additional experiments (not shown here) indicated furthermore that the channel structure reappears if loading with oil aerosol resumes later on. One may thus conclude that the homogeneous liquid distribution in pre-saturated filters is a dynamic phenomenon. Finely dispersed liquid has to be replenished constantly in S_0=1 filters in order to maintain the performance typical of pre-saturation filters. How exactly the effective wettability is subject to (at least) some reversibility is not clear, but may hold the answer as to why the channel structure in a steady S_0=0 mode of operation is so resistance to transitioning into the homogenous distribution.

9.3.3 On the mechanisms behind the continued Δp creep

Based on the observations discussed so far, two separate processes appear to contribute to the phenomenon we have loosely termed Δp creep, one related to the continued increase in S associated with the formation of new oil channels, the other due to a "reorganization" of the oil distribution pattern in the channel region (at constant S).

The slow but continued increase in S drives the Δp creep for a very long time after a filter reaches "steady state"; according to our data at least for the first 100 hours or about 400 times the time required to reach steady state (compare Fig. 9.3). This saturation creep has been observed for all media investigated. It occurs solely *within* the channel section and contributes only to the "internal" $\Delta p_{channel}$. The "external" Δp_{jump} due to formation of a thin liquid film (in case of wettable media at the downstream filter face) is not involved in this process. Δp_{jump} remains constant during creep and depends only on the pore structure of the media (Kampa et al., 2014; Kolb et al., 2017), not on filter operating conditions.

However, the increase in Δp during that phase does not suffice to reach the observed pre-saturation Δp (compare the data on the right-hand margin of Fig. 9.3a). That gap can only be closed by an additional mechanism such as the dissolution of oil channels during loading times well beyond 100 h, or perhaps by variable air flows as shown later in the paper.

The effect of a dissolution of the oil channels on $\Delta p_{channel}$ can be estimated on the basis of a model derived by Kolb et al. (2017) for the two limiting scenarios, namely a completely heterogeneous and a perfectly homogeneous oil distribution within a mist filter

$$\Delta p_{channel} = \frac{\Delta p_0}{(1 - S)^n} \tag{9.1}$$

wherein Δp_0 is the initial (dry) pressure drop of the filter. The exponent n is 1 for a *heterogeneous* oil distribution (i.e. when all the oil is accumulated in one or a few large regions) and 4.55 for a *randomly homogeneous* distribution. In reality, the oil distribution pattern will lie somewhere between the extremes and the value of the exponent thus becomes an indicator for its uniformity. Of course, the model Eq. 9.1 is based on certain assumptions, but suffices to analyze the behavior of multi-layer filters.

Fig. 9.7 shows a set of curves for $\Delta p_{channel}/\Delta p_0$ vs. S calculated according to Eq. 9.1 assuming values of n between 1 and 4.55. Superposed on these curves are actually measured values of the relative channel pressure drop at different loading stages for the four oleophilic media used in our experiments. The experimental pressure drops were extracted from Fig. 9.3 on the basis of the Film-and-Channel Model Kampa et al. (2014), in other words

$$\frac{\Delta p_{channel}}{\Delta p_0} = \frac{\Delta p_{total} - \Delta p_{jump}}{\Delta p_0} \tag{9.2}$$

and plotted against the average saturation of all layers except the last (which contains the film).

When reaching "steady state" (circles in Fig. 9.7), all filters exhibit a well-developed channel pattern corresponding to an exponent n in the range of about 2 to 3.5. The ensuing saturation creep shifts the data points to the right and slightly upward, although not consistently (squares); neither the channel pattern nor n have not changed fundamentally after 100 hours. On the other hand, the pre-saturation pressure data show a sharp increase in n to values near the theoretical limit which clearly corresponds to the homogenization of the oil distribution, but without much further change in S.

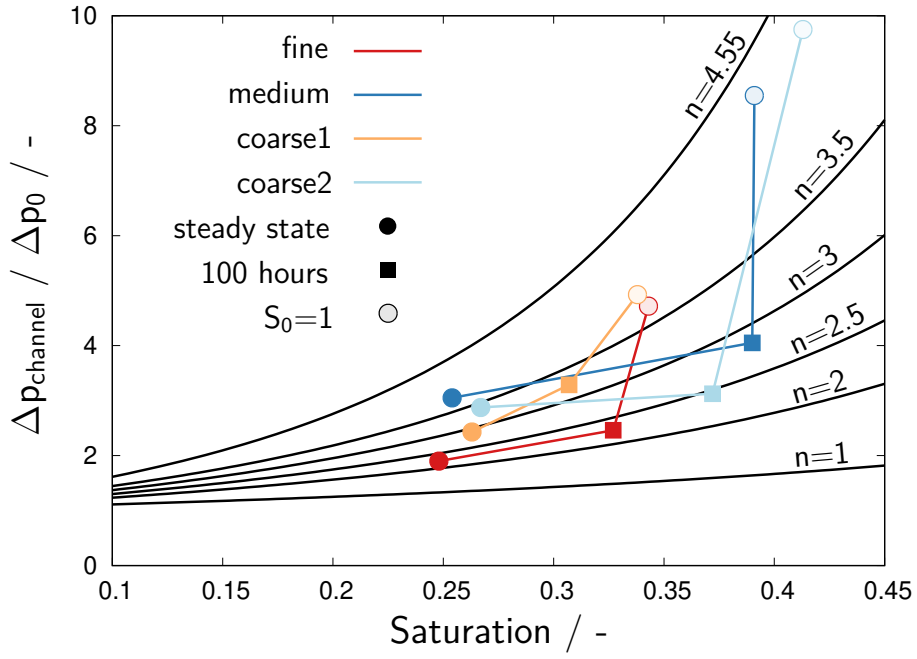

Figure 9.7: Experimental Δp data of wettable media at different stages of filter loading (according to Eq. 9.2) plotted over an array of pressure drop curves for different values of n (according to Eq. 9.1).

While it is thus possible to explain and even quantify large differences in wet pressure drop by different oil patterns, it remains unclear, when and how such a dissolution of oil channels (i.e. a transition of the exponent n from about 2.4 to around 4) might actually happen; or even if it happens at all during steady operation. Neither photographic images of the channel patterns such as in Fig. 9.5, nor the differences of pressure drop seen in Fig. 9.3, hint at a progressive or imminent dissolution. In fact, even when the pressure drop has leveled off within 100 h, as was the case for the coarse media, it remains well below the S_0=1 endpoint. For the fine media, an extrapolation of the Δp slope beyond 100 hours suggests convergence after about one century of continuous loading. Liquid channels in fibrous media are extraordinarily stable under continuous operation. It thus becomes clear that – despite small and seemingly insignificant differences in average saturation between 100 h and the pre-saturated S_0=1 state – the liquid distributions of pre-saturated filters actually have very little in common with those of their initially dry counterparts.

9.3.4 Relationship between face velocity and saturation (for S_0=1 and S_0=0)

The channel saturation was shown in previous work to decrease with face velocity, both for pre-saturated filters (Mead-Hunter et al., 2013) and for initially dry filters (Kolb et al., 2017). For initially dry filters, the Film-and-Channel-Model provides an (at least intuitive) explanation based on oil transport considerations: $\Delta p_{channel}$ represents the supplementary pressure drop required to "pump" oil through the channels at the rate determined by the filter loading rate. If this supplementary pressure is achieved via a higher air flow velocity, then the saturation required to build up the necessary $\Delta p_{channel}$ becomes lower. For pre-saturated filters the oil transport no longer occurs in channels (which have disappeared) but somehow from fiber to fiber, possibly as drops (Dawar and Chase, 2008, 2010; Mullins et al., 2006) but models linking saturation and filter operating parameters have yet to be developed for this scenario. Regardless of physical explanation, one may assume that higher air flow velocities (at constant loading rate) will always contribute to a faster oil transport, and thus lead to an inverse relationship between filter face velocity and saturation in the channel region.

The dependence of S on v is investigated in Fig. 9.8 for the cases S_0=0 (steady state immediately after the onset of drainage) and S_0=1 (i.e. pre-saturated filters). For the sake of legibility, the figure includes data sets for only two of our wettable media and one non-wettable medium: The wettable media

represent the two available extremes in terms of fineness ("coarse 1" and "fine" according to Table 9.1); the non-wettable medium corresponds in fineness to the coarse wettable medium. These data a coded by symbol and color according to the legend in Fig. 9.8.

Beside our own new data, the figure also includes saturation data extracted from Mead-Hunter et al. (2013) for wettable glassfiber media GF1 to GF4, which roughly correspond in fineness to our media. The Mead-Hunter data are offset systematically to higher values of saturation, probably because the film-containing layer was included in the averaging, and possibly also the saturated edges of the media where they are clamped into the filter holder. They appear to converge to S=1 for v=0 as one would expect, but do not follow a defined function at higher velocities. In the absence of a model for pre-saturated filters, a power law function of the type $S \sim v^a$ with $a \approx -0.23$ was fitted to the data.

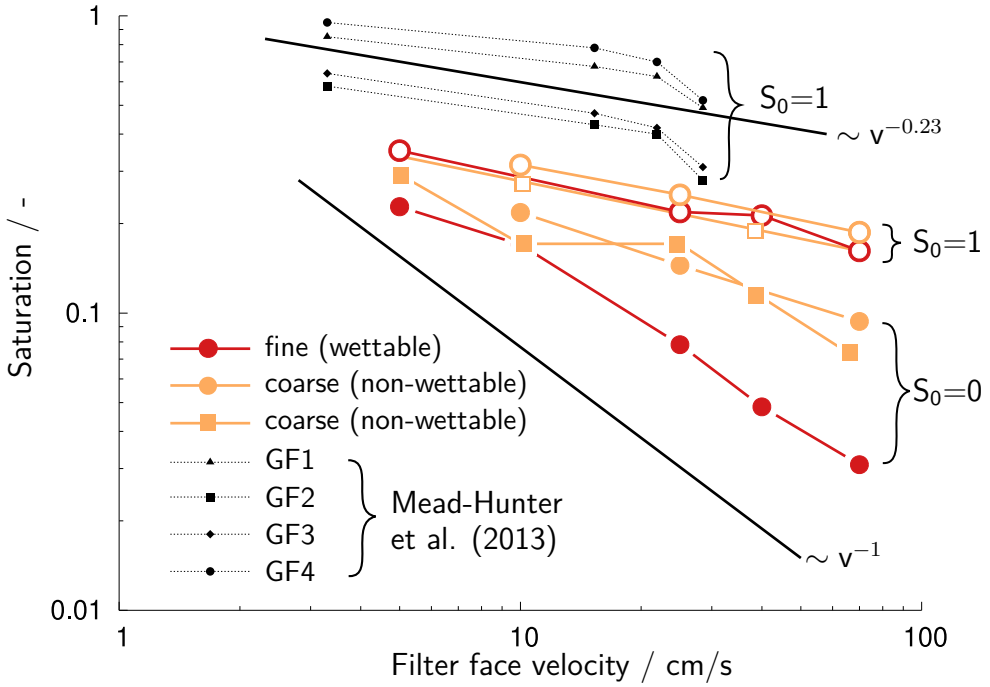

Figure 9.8: Average saturation vs. filter face velocity for various filter sandwiches loaded at a rate of 60 mg/(m^{2}s). Wettable media have 10 and 11 layers, respectively; non-wettable medium has 6 layers. Saturation is averaged over all layers except-film containing layer. Saturation data for pre-saturated GF1 – GF4 from Mead-Hunter et al. (2013) are averaged over all layers and fitted to a power law function ($S \sim v^{-0.23}$)

Beginning the discussion of Fig. 9.8 with the pre-saturation data (S_0=1), one notices that the three curves for our wettable and non-wettable media lie very closely together. Given the usual variability between media samples of about 5% (roughly the size of the data points), they practically coincide with regard to saturation. It is also worth noting that the slope of our pre-saturation data

(≈0.27) is very close to that of the regression line for the Mead-Hunter data (solid black line).

The saturation levels in steady state (i.e. for the S_0=0 case) are generally lower than for pre-saturated media (S_0=1), and the gap widens as the media become finer. The saturation data for the coarse non-wettable medium are indistinguishable from that of the coarse wettable medium. (The non-wettable medium also shows creep, similar to the wettable one, but we have fewer and less complete data on non-wettable media and for that reason did not included them in this paper.)

Saturation levels in steady state are generally lower for finer media (for all the media we have studied), probably because the lower pressure drop of the filter matrix slows down the oil transport, and therefore requires more saturation to reach the necessary Δp for pumping. Also the slopes are steeper for finer media, confirming the trend observed in earlier work, that the saturation decreases more rapidly toward higher flow velocities and appears to approach the $S \sim v^{-1}$ dependence (solid black line) proposed by Kolb et al. (2017) for the same grade of fine medium.

9.3.5 The saturation gap and the kinetics of Δp creep

According to Fig. 9.8, the saturation levels for S_0=1 are generally higher than for S_0=0 and this "saturation gap" between S_0=1 and S_0=0 widens with increasing flow velocity and also with increasing fineness of the media. Most interestingly, the magnitude of the saturation gap correlates qualitatively with the magnitude and rate of Δp creep.

The saturation gap provides a kinetic argument why both creep is faster at high flow velocities (compare Fig. 9.1) and for fine media (compare Fig. 9.3). The amount of liquid required to close the "saturation gap" between the two curves can be interpreted as a driving force behind creep during continuous loading and gives a relative prediction of the creep behavior to be expected. Furthermore, one can surmise that creep will not be over until the saturation gap has been closed. Note however that this is first of all a useful kinetic argument. The dynamics of the process may have something to do with capillarity, but remain to be elucidated. (Simple explanations using capillary rise models based on the Washburn Equation and its derivatives have not given satisfactory results and are therefore not pursued in the context of this paper. What further complicates dynamic models is the fact that both wettable and non-wettable media exhibit creep.)

In addition to estimates of creep for media during steady loading, Fig. 9.8 allows predictions of how the saturation level will change when the filtration velocity varies *during* operation. In particular, a significant reduction in v will lead to a corresponding increase in S. And since the saturation gap between the S_0=0 and S_0=1 states narrows, this can be used to approach the latter state dynamically, as shown in the following experiment:

A fine, initially dry filter was operated at constant v=25 cm/s in S_0=0 mode until it reached steady state (preceded by the characteristic Δp_{jump}), with some subsequent creep (① in Fig. 9.9). Under these conditions S was measured in a separate experiment to be 8% (inset of Fig. 9.9). Then, for the next 50 h the flow velocity was reduced to less than 1 cm/s. This entailed a reduction of the oil loading rate and a barely measurable pressure drop across the filter. During this period the saturation increased from 8% to about 70% without detectable drainage from the rear side – an indicator that the filter was indeed accumulating oil internally. Drainage re-appeared around t=33 h and coincided with the characteristic Δp_{jump} normally seen when drainage starts[2]. Thereafter the filter remained in this steady state mode of operation at v=1 cm/s until about t=50 h (② in Fig. 9.9).

Note that the filter was now operating at an elevated saturation, in a state close to those of pre-saturated filters. When the face velocity was subsequently raised to its previous value of 25 cm/s, the excessive oil had to be blown out (which causes the brief peak at 140 mbar) until the filter swung into a "second steady state" at a saturation of 25% (③).

This new state 3 corresponds in Δp and saturation to the levels measured in a separate experiment starting at S_0=1. Also, the channel structure disappeared and liquid distribution has become homogeneous in this state 3. We conclude that the disappearance of the channel structure and a homogeneous liquid distribution can also be achieved dynamically, and are (again) related to a complete or at least very significant (S = 70%) flooding of the filter.

Note that the filter apparently has two steady modes of operation (① and ③) at the same flow velocity. State ① corresponds to the conventional steady state, the other to the pre-saturated mode, which is associated with a relatively constant Δp.

[2]The re-appearance of a Δp_{jump} is an indicator that the film may collapse when the flow is significantly reduced and then requires more liquid to re-build. Also note the similarity of the two jumps at t=1 h and t=33 h which are both approximately 38 mbar and independent of flow velocity.

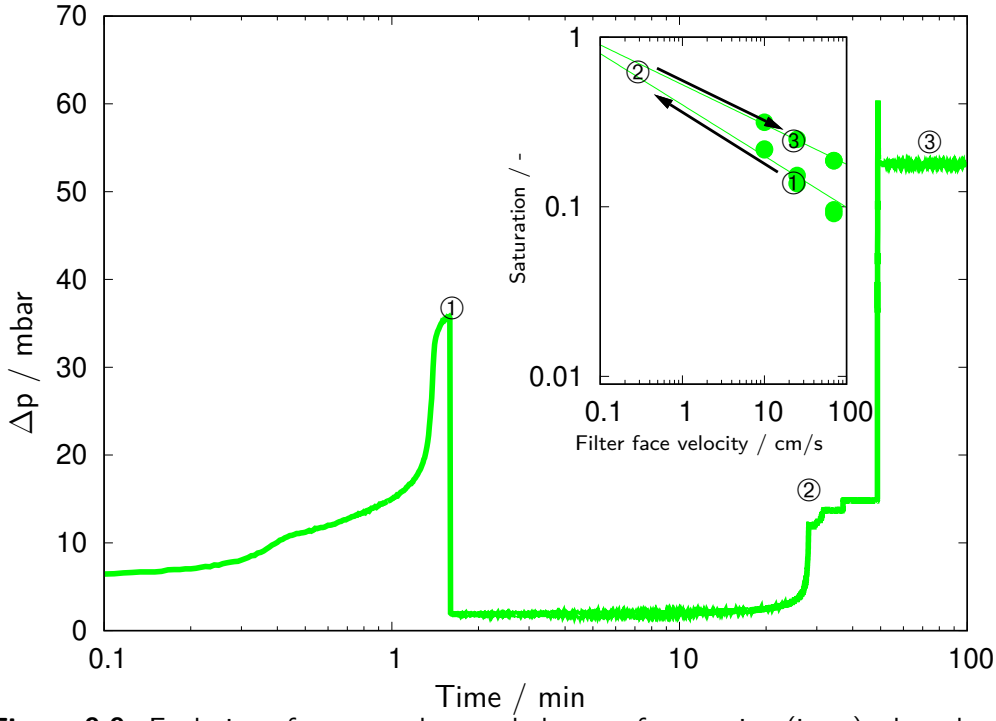

Figure 9.9: Evolution of pressure drop and change of saturation (inset) when the filter face velocity is reduced from 25 cm/s (①) to less than 1 cm/s (②) and raised to its initial value again (③). Experiment were conducted with a 5-layer sandwich of the fine medium.

9.3.6 Pre-saturation vs. on-off operation: do they have the same endpoints?

We have seen in the preceding section that pre-saturated media represent the likely endpoint for discontinuous operation between high and low air flows. Achieving such a "pre-saturation during operation" from S_0=0 requires two processes: A sufficient and continued supply of oil to fill the saturation gap; and capillary mechanisms to hold the oil within the filter and to convert the channel structure into a diffuse distribution of oil. Temporary operation of the filter at a very low but non-zero velocity is presumably a prerequisite to fulfill both tasks.

The question remains whether a simpler method of acceleration such as on-off operation would accomplish the same objective. As mentioned in the introductory literature review, on-off operation (starting from S_0=0) has been used repeatedly in the past and does lead to spontaneously higher Δp when the flow resumes. We thus repeated a loading experiment with our fine media (wettable and non-wettable), where we switched off the flow repeatedly for 3 h periods as shown in Fig. 9.10. (3 hours were deemed sufficient for capillary rearrangement of liquid to occur during the off phase.) Beside recording Δp, the

saturation was also measured in separate experiments. After each resumption of flow, Δp evidently reached a new plateau that was slightly higher than the one before and looks like a steady state because the drainage continues with a constant rate during the on phase.

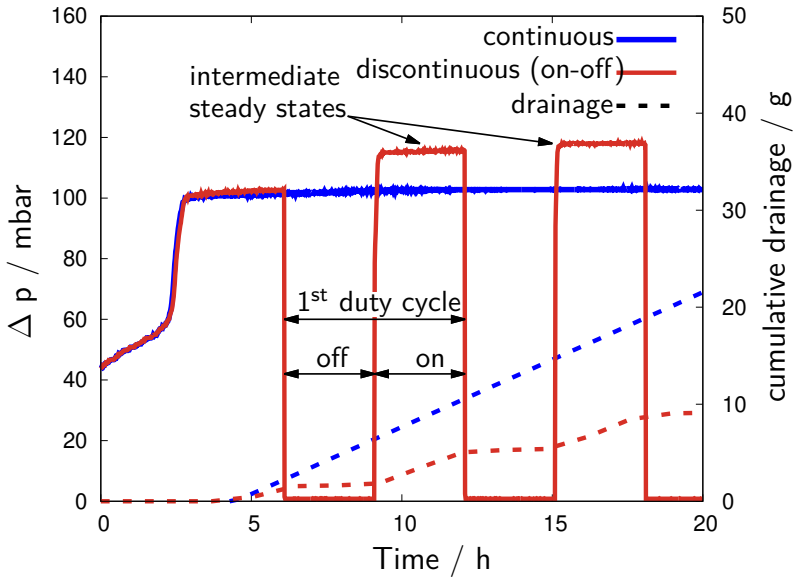

Figure 9.10: Evolution of Δp and cumulative drainage during on-off operation compared to steady filter operation (fine media, v = 25 cm/s during on cycles, oil loading rate R = 60 mg/(m^{2}s))

Fig. 9.11 shows the evolution of Δp for up to 21 such duty cycles. Both fine media (wettable and non-wettable) reach a more or less constant Δp level after about 6 cycles. This is similar to the findings of Bredin and Mullins (2012) for coarser wettable and pre-saturated media. The saturation on the other hand does not change appreciably during the entire experiment, for either medium. One may therefore conclude that the gradual increase in Δp with successive duty cycles must be due entirely to capillary rearrangement of the oil during the off-cycles. And this seems to be the case regardless of wettability.

A comparison of channel patterns (based on photographic images similar to Fig. 9.5) between continuously and intermittently operated filters revealed neither a significant change of the original channel pattern nor any signs for newly formed channels with increasing number of duty cycles as was the case for creep (Section 9.3.1). The pressure drop thus seems to be very sensitive to slight changes in oil pattern which are not visible to the eye (compare also Fig. 9.7).

According to Fig. 9.11, neither medium approaches the pre-saturation Δp sufficiently during on-off operation to suggest convergence. (Δp endpoints for pre-saturation are stated in the figure caption because they are off scale.) The

lack of convergence probably has to do with the lack of oil supply during the off phases. On the other hand, the re-organization of oil must be accelerated during such off-phases, thereby causing the step increase in Δp.

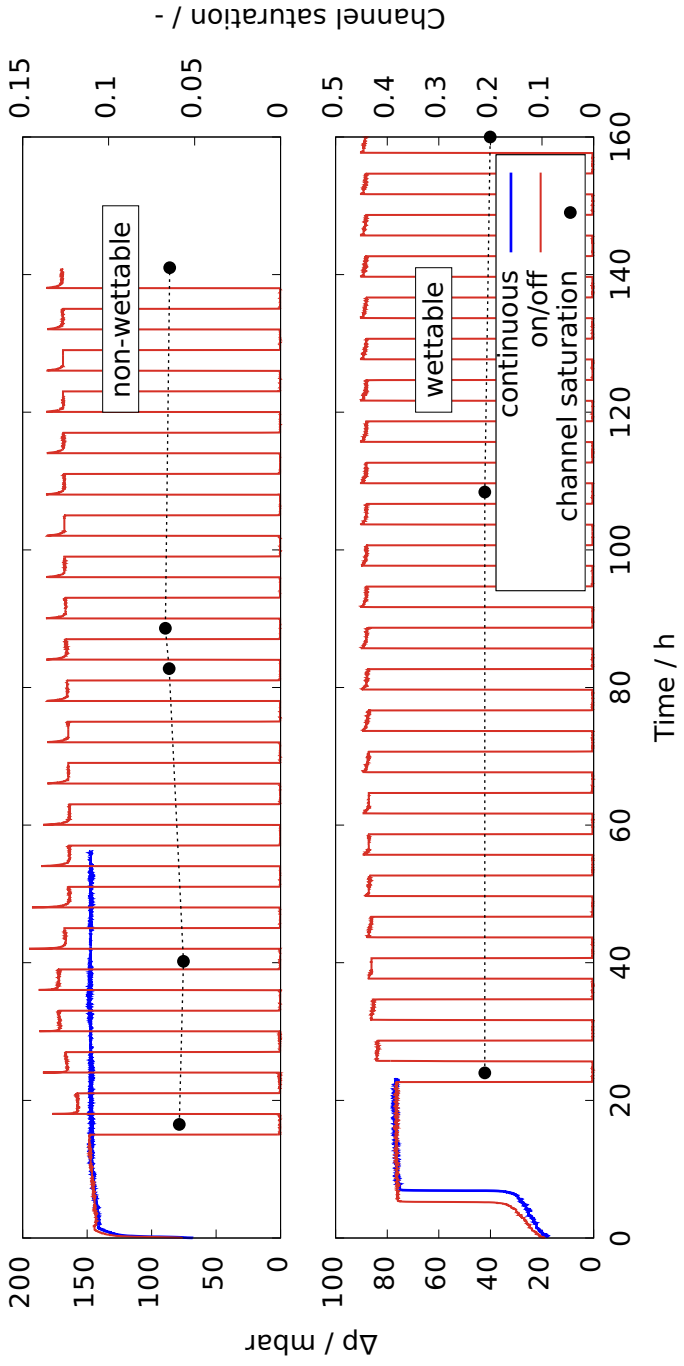

Figure 9.11: Evolution of Δp and S during long-term operation with flow interruptions compared to steady filter operation. Respective Δp endpoints of pre-saturated filters were 122 mbar (wettable) and 255 mbar (non-wettable). Operation of non-wettable media at v = 25 cm/s , R = 60 mg/m^{2}s and the wettable media at v = 10 cm/s at the same R.

One may speculate that the remarkable stability of oil channels during normal steady filter operation has something to do with the continued air flow: while the flow is on, it drives the oil along the channels in the direction of flow, so that the supply needed for sideways transport by capillary effects is very small. In other words, oil prefers to move along the channels rather than sideways.

For that reason, filters in *stable* operation show a relatively rapid onset of drainage (the beginning of the "steady state") via channel formation and retain the channel pattern for extremely long times. In stable operation the number of channels may increase very slowly with time (due to additional aerosol deposition and coalescence into channels), and so will the saturation. This Δp contribution causes the observed creep during 100 h, but it alone is not sufficient for convergence with the pre-saturation Δp. That would require a diffuse oil distribution, which can be accelerated only by shutting of the air flow. But temporarily shutting off the air prevents the supply of new oil to close the saturation gap. Convergence can thus only be accelerated via the experiment described in Section 9.3.5.

A final detail to discuss in Fig. 9.11 is the difference in shape of the Δp curve between the non-wettable and the wettable media. The non-wettable medium has a pronounced pressure spike at the beginning of each duty cycle, which probably results from the need of the air to force open the liquid film on the filter face that closes completely during the off-cycle. (This closing and reopening of the film happens during each cycle.) The film on the rear face of the wettable media is also closed but apparently requires much less excess Δp when the flow resumes. Also, Fig. 9.11 shows a small maximum in Δp around the 4^{th} duty cycle that appears only for the non-wettable medium and is associated with a slight dip in saturation. We think that this is an indication for changes in effective wettability due to the presence of oil. (A similar kind of observation is discussed in Section 9.3.2 for pre-saturated media).

9.4 Summary and conclusions

The phenomenon of Δp-creep was investigated experimentally with several different glass microfiber filter media, 4 of which were wettable and labelled coarse 1, coarse 2, medium, and fine based on pore size and fiber diameter data (Table 9.1). Data for two non-wettable medium were also included. The experiments were conducted with flat sandwiches, each composed of 6 to 11 identical coupons of the same media, at a rather high aerosol loading rate of 1.1 g/(m^2s). Flow velocities were varied up to 70 cm/s. Experiments started either with a dry filter (designated as S_0=0), or with a completely pre-saturated

filter (designated as S_0=1). The S_0=0 runs reached "steady state" (defined as the onset of drainage) after approximately 0.3 hours and were then continued for another 100 h.

As expected, the filter pressure drop during the creep phase continued to increase, and more so for filter media with higher dry pressure drop Δp_0 (as predicted by Eq. 9.1). In other words, finer media creep further than coarser media. On the other hand, the differential pressure drop of the coarse media levelled off sooner, to become constant in less than 40 hours, whereas finer media did not reach an asymptotic value of Δp within the duration of the experiments, i.e. 100 h. Extrapolation of these Δp curves to some hypothetically stable value would lead to creep times on the order of a century. It thus remains questionable if a steady Δp is feasible at all by continuous oil loading.

It was further found that the Δp creep observed during 100 h of operation was associated with an increase of the internal saturation S (moving from front to rear), that approached or reached the level of pre-saturated filters (i.e. S_0=1) by the end of the experiment. The increase in internal saturation was accompanied by the formation of additional (very fine) oil channels, but overall the channel structure was persevered throughout the 100-h experiments.

Under steady loading conditions from S_0=0, the channel structure was thus retained throughout the experiments, and despite the observed leveling-off of the internal saturation level. On the other hand, no channel structure was visible for initially pre-saturated media and the oil must therefore have been very uniformly and finely distributed on the fibers.

On the basis of the increase in S observed during the creep phase we are able to explain part of the measured Δp creep, but not all of it. In order to explain the "missing Δp", one needs to assume additionally, that the liquid distribution changes from a channel structure to become very homogenous. However, this reorganization process appears to be much slower than the levelling-off of the average layer saturation and did not happen within the time of our experiment.

Intermittently shutting off the air flow (on-off operation) permits a step function increase in Δp, probably due to an acceleration of liquid reorganization during off-phases, but does not supply enough oil to close the saturation gap. Therefore successive Δp plateaus in on-off operation do not converge to the p endpoint achieved by presaturation.

With regard to saturation levels as well as pressure drop, our experiments therefore show clearly that the on-et of drainage under steady external conditions does not automatically represent an internal steady state. Moreover, since the internal oil accumulation reaches a steady endpoint sooner than the Δp (which

may not reach a steady endpoint within the filter lifetime), even a constant value for S is thus no guarantee for a constant value in Δp.

The concept of a steady state is perhaps a useful operational term for relatively coarse filter media and for experimental times of more than one day of operation after the onset of drainage. For highly efficient mist filters it remains a moot point and is strictly speaking inappropriate to most states achieved in experiments of less than a day. Here, the onset of drainage (associated with a steep increase of Δp) should be used as a comparison reference point.

Acknowledgements

The authors would like to thank Atlas Copco Airpower n.v. for partial support of this work as well as Ann-Kathrin Müller who conducted experiments with air flow interruptions.

10

Characterization of filter media based on capillary flow porometry[1]

Abstract

The application of capillary flow porometry by gas-liquid displacement to the measurement of pore size distributions in (identical) glass microfiber filter media can lead to rather divergent results. The causes for these differences as well as the factors that influence the over-all reliability of data obtained by this widely used technique have been investigated.

Among the key factors studied were the volatility and viscosity of four commonly used wetting liquids, the scan rate (i.e. the holding time interval between increments of differential pressure Δp or volumetric flowrate $\dot{V}$), and the scan sequence (i.e. dry before wet, or wet before dry scan). Measurements were mostly made with a porometer designed in house, in order to have complete control over all aspects of operation. Data obtained with commercial porometers are also reported. For best comparability, all measurements were made with the same batch of standard glass microfiber media.

The largest error source by far was the volatility of fluorinated compounds

[1] This article was published as: Kolb, H. E., R. Schmitt, A. Dittler and G. Kasper (2018). *On the Accuracy of Capillary Flow Porometry for Fibrous Filter Media*, Separation and Purification 199, 198–205.

commonly used as wetting liquids. While the vapor pressures of such compounds may be relatively low, their use in combination with a flow of air through the porous matrix can have an enormous effect on the evaporation rate during a scan. Neglecting this effect (which obviously depends on the scan rate) may ultimately result in an error of almost arbitrary magnitude in the pore size distribution. Silicone oil on the other hand has a negligible volatility and provides reliable results for a wide range of operating conditions. The liquid viscosity in the tested range of about 1:20 played a comparatively insignificant role. These and other factors of uncertainty are discussed on the basis of experimental data.

Keywords: Fibrous media, characterization, porometry, volatility, wetting liquid

10.1 Introduction

Capillary flow porometry is a well-established technique for measuring pore size distributions in polymer membranes and fibrous media within a useful range of typically about 1 to 50 µm. Its operating principle, as suggested by Erbe (1933), is based on saturating small samples of the media completely with a wetting liquid, and then progressively "discharging" pores with a second fluid by increasing the differential pressure Δp across the sample. From the attendant increase in volumetric flow rate (or flow velocity) through the sample one can then derive a cumulative pore size distribution. The displacing fluid can be either air, as in most commercial porometers, or another liquid (Morison, 2008).

Assuming the pores have an ideally circular cross-section, the relationship between the differential pressure Δp and the smallest empty pore d_{pore} is given by classical capillary theory, as

$$d_{pore} = 4\frac{\gamma\, cos(\Theta)}{\Delta p} \tag{10.1}$$

with corrections required for a non-ideal pore morphology (Yu et al., 2010; Agarwal et al., 2012). Assuming further that the surface tension γ and the wetting angle Θ are constant for the entire internal surface of the media, the pore size distribution can be calculated from the ratio of the volumetric air flow rates through the dry and the wet media at the same Δp:

$$Q(\Delta p) = 1 - \frac{\dot{V}_{wet}}{\dot{V}_{dry}} \tag{10.2}$$

$Q(\Delta p)$ is the cumulative number distribution of (equivalent) pore diameters

d_{pore} as given by Eq. 10.1. The largest pore diameter (at Q=1) corresponds to the bubble point (as defined e.g. by ASTM F316-3) and is relatively easy to establish. On the other hand, the smallest pore diameter (at Q=0) depends on the maximum Δp sustainable by the media and possibly other external factors. A method of extending the lower limit of detectable pores is discussed by Hernández et al. (1996). This technique will not be used here, however.

Capillary flow porometry is quite attractive to characterize porous media for applications such as filtration (Qin and Wang, 2006; Li et al., 2006; Calvo et al., 1996), catalysis (Madhugiri et al., 2004) or chromatography (Aggarwal et al., 2012). Being a flow-based method, it is often preferable to purely geometric or tomographic techniques such as described by Lehmann et al. (2005) or Hoferer et al. (2006), and also less cumbersome. Porometers are thus available commercially, and ASTM F316-3 describes their use for "non-fibrous membranes". Despite such widespread use, the scientific literature contains few critical analyses of the methods fundamental reliability. The ASTM guideline F316-3 is vague with regard to details of applying the method.

Yunoki et al. (2004) investigated the influence of three wetting fluids (alcohol, Porofil™and ethylene glycol) on the pore size distribution of fibrous media. The authors observed a tendency of the distribution to become narrower and shift towards larger pores, which they correlated with the viscosity of the fluid and attributed to kinetic effects during the blow-out of wetting liquid. The same paper also shows the effect of scanning rate, as will be discussed later.

Dixon (1998) also discusses the impact of a broad range of wetting fluids on capillary flow porometry as applied to filter media. This hard-to-access conference paper also describes a "scatter" among the wet curves for more volatile liquids such as alcohol, and a relative independence of the bubble point. On the other hand, a "reduced effect of volatility for smaller pores" was observed.

Due to our interest in obtaining reliable pore size data for glass fiber filter media, we have in the past conducted comparative tests with several commercial porometers. The results (presented in the next section of this chapter) showed very good reproducibility when repeated on the same machine and with the same sample material, but varied considerably between porometers. The reasons for these variances were not immediately clear, but may have been due to a number of reasons, including differences in the properties of the wetting liquids recommended by the respective porometer manufacturers, in scanning times of Δp or $\dot{V}$, in sample area, and perhaps also unknown details of the proprietary software routines to convert raw data into pore size distributions.

Consequently, we conducted a more thorough study on the reliability and comparability of this important technique, focusing on the influence of wetting fluids and the way a porometer is operated. In order to make the influence of these parameters fully transparent and independent of any specific commercial device, the measurements reported here are based on a laboratory prototype device designed specifically for that purpose. On the other hand, the experiments reported hereunder were limited to a single type of glass microfiber media, which can be considered representative of an entire class of such media.

10.2 Preliminary comparison tests with commercial porometers

The evaluation included three porometers, a *CFP-1500-AFX* (PMI Inc.), a *3GzH* (Quantachrome GmbH), and a *PSM 165* (Topas GmbH). Of these, the PMI device is available in house, the other measurements are courtesy of the respective instrument manufacturers with samples of glass microfiber of the same media investigated later in this chapter.

Sample results for one typical filter medium are shown in Fig. 10.1 to characterize the differences in resulting pore size distribution. Evidently, the differences are substantial in various aspects of the distribution. Values for the largest pore corresponding to the "bubble point" – normally very easy and reliable to determine – range from 16 µm (Topas) to 20 µm (PMI), with the value for Quantachrome (red curve) in between. The d_{50} values agree for two of the three instruments (around 7 µm), while the third instrument gives a larger value of about 10 µm. Both the upper and the lower ranges of the respective distributions differ substantially with regard to shape and contribution to the distribution. Especially the red curve (labeled Quantachrome) appears to be multimodal on the upper end, while the others are mono-modal. In fact, the only thing all three porometers seem to agree on is the minimal pore size around 5 µm.

Data for other tested media show a similar spread of values, but are not presented here, because more data would add nothing further to the description of the problem. Despite the observed deviations *between* instruments, repeated measurements on the *same* device produced nearly identical pore size distributions. (To some extent, this eliminates differences in sample size from the list of candidate causes.)

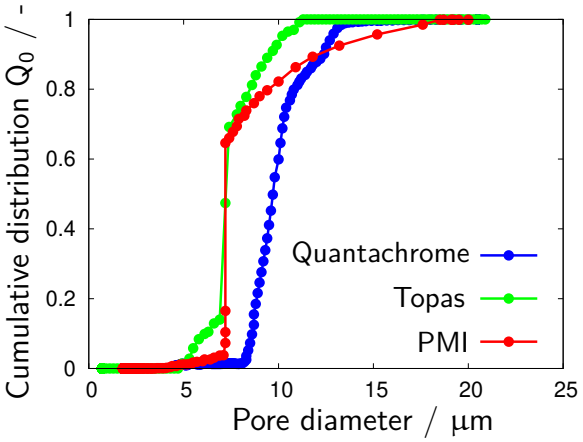

Figure 10.1: Pore size distributions obtained by 3 different porometers for the identical type of glass fiber filter media. Working fluids used and scan procedures are those recommended/implemented by the instrument manufacturers.

In sum, the differences between the respective curves are substantial and far too big to make these data useful for inter-comparisons of media, or the interpretation of filter behavior. Considering furthermore that the operation of a porometer involves only standard measurements of flow and pressure, these results are hard to explain. They cannot simply result from a translational shift due to some kind of calibration offset. Even though some deviations may be due to differences in instrument design and/or operation (e.g. sample area or scan time), other, major questions remain regarding the influence of the wetting fluids, the scan mode (Δp-scan vs. $\dot{V}$-scan), or the software.

10.3 Experimental materials and methods

A porometer consists of only three essential components, an open-face sample holder, a differential pressure gauge, and a device (such as a mass flow controller) to measure and control the airflow, as shown in Fig. 10.2. We therefore chose to build our own, in order to have all factors under our control.

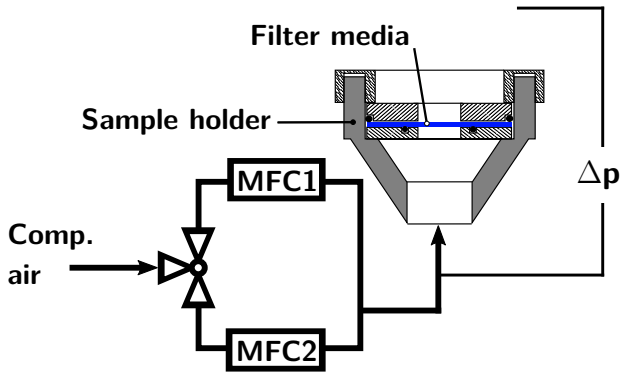

Figure 10.2: Schematic diagram of the prototype porometer operating at differential pressures of 0-1000 mbar and volume flows of 0-200 L/min (by one of two mass flow controllers, MFC).

The circular filter sample had an effective diameter of 14 mm, which constituted a compromise between mechanical strength and a representative sample area with sufficient pores. Also, the area was large enough compared to the clamped fringes. The sample holder was checked for leak-tightness.

For the sake of better comparison, all measurements reported hereunder were performed on the same type and batch of glass microfiber filter media, a standard commercial product (Hollingsworth & Vose) with a mean fiber diameter of 1.6 µm, a porosity of 95%, and a thickness of about 0.5 mm. These media show spontaneous liquid wicking and may be considered fully wettable to all the liquids used in this work. The filter material was chosen because of its relatively good uniformity, which eliminates one potential error source from the measurements.

A flow of clean and dry compressed air was fed to the sample holder via one of two mass flow controllers having different operating ranges (MKS 1179A for 0-4.7 L/min, MKS 1579A for 4.7-200 L/min). A pressure transducer (Omega PD-23, 0-1000 mbar) measured the pressure drop across the sample. Both airflow and pressure drop were recorded continuously by a computer.

The system could be operated either by setting Δp in predetermined increments and measuring the resulting flow rates, or vice versa. Both possibilities were realized as discussed later on. Experiments were always conducted in constant increments of scanning time, during each of which the controlling process variable was held constant while the dependent variable was recorded. These time increments were chosen as 1, 2, 10, 20, 60 or 120 minutes.

Unless noted otherwise, each measurement sequence consisted of two separate runs (Fig. 10.3). First a "dry" curve of Δp vs. $\dot{V}$ was recorded. Immediately following the dry measurement, the sample was saturated completely with a constant amount (200 µl) of one of the recommended wetting liquids (Table 10.1), without dismounting it from the sample holder. With this amount of liquid, the level of fluid above the sample is less than 1 mm and therefore negligible for the differential pressure drop. Finally, a "wet" measurement was performed by raising Δp across the sample at a rate of less than 1 mbar/min via the lower-range MFC. The onset of bubble formation, i.e. the bubble point, was determined visually. Before starting, each sample was blown out with dry compressed air in order to remove any remaining humidity from its pores.

The pore size distribution was then calculated point by point according to Eq. 10.2 from the respective airflow rates of the wet and dry curves. In order to obtain exactly corresponding values of the flow for a given Δp, the dry curve was fitted by a 2nd-order polynomial. This then permitted interpolation to the

same Δp. For the subsequent graphs and discussion we have chosen to replace volumetric flow rates by the corresponding sample face velocity, because this is more general and eliminates the dependency on the sample diameter.

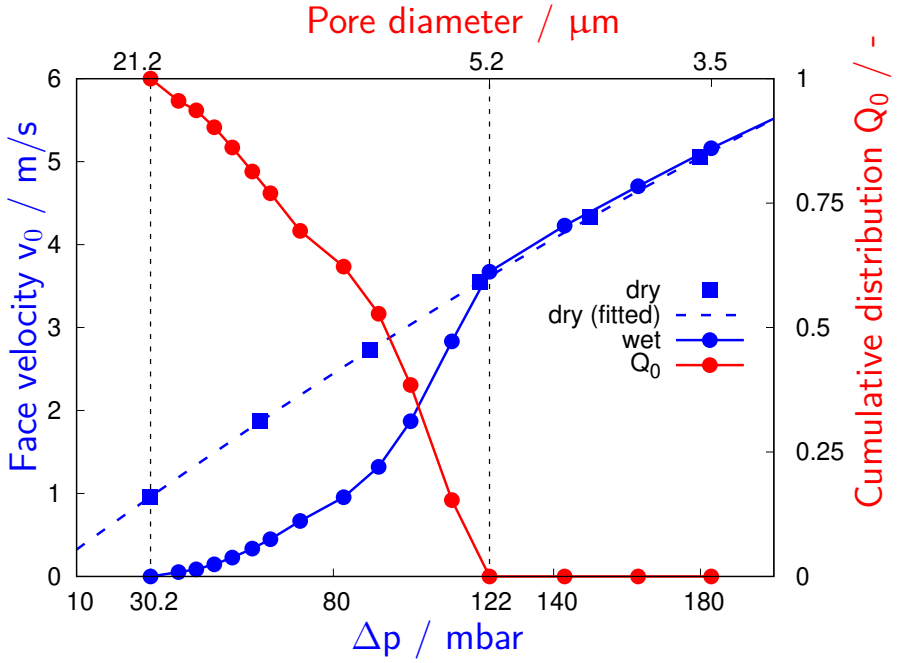

Figure 10.3: "Wet" and "dry" curves (blue) of flow vs. Δp. The "dry" curve is fitted with a second-order polynomial for interpolation purposes (dashed line). The resulting pore size distribution (red) lies between 5.2 and 21.2 µm for a scan time interval of 1 min in a pressure controlled run. The wetting liquid is Galwick™.

	Brand name	Surface tension γ mN/m	Kinematic viscosity ν mm^2/s	Vapor pressure Pa
Fluoro-carbons	Galwick™	15.9	NA	1-20
	Porofil™	16.0	NA	NA
	Topor™	16.0	2	approx. 400
Silicone oils	Wacker™AK 5	19.0	5	NA
	Wacker™AK 10	20.0	10	NA
	Wacker™AK 100	21.0	100	< 10

Table 10.1: Wetting liquids per recommendation of the respective instrument supplier with properties at STP conditions, if available.

10.4 Results and discussion

This section addresses and discusses the influence of various experimental factors and potential error sources on the porometry measurement, starting with the most important one, namely the properties of the wetting fluid.

10.4.1 Influence of the volatility of the wetting liquid

Fig. 10.4 shows the wet and dry scans (Fig. 10.4a), as well as the resulting pore size distributions (Fig. 10.4b) for each of the four working liquids, including the non-volatile silicone oil (Wacker™AK 10) and the more or less volatile fluorocarbons Galwick™, Topor™ and Porofil™. Note that only the mean dry curve is shown (black dashed line going through the origin) because the individual ones overlap almost perfectly. The Δp-controlled scan was stopped at 400 mbar.

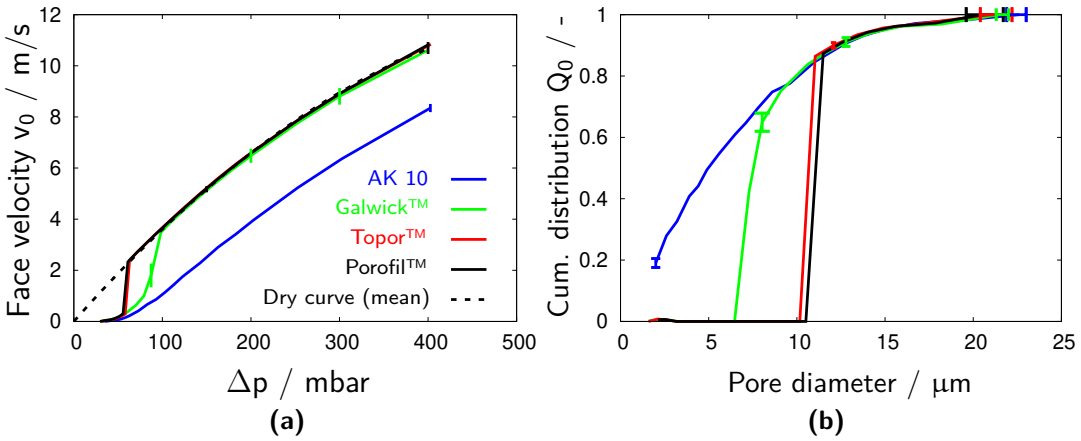

Figure 10.4: Wet and dry curves (a) and resulting pore size distributions (b) for 4 different wetting fluids. Measurements were Δp controlled with constant scanning time intervals of 2 min each.

The resulting pore size distributions in Fig. 10.4b are each the average of three separate runs. Error bars indicating the respective standard deviation have been inserted where feasible, because errors where mostly negligible on the scale of the graphs. Repeatability was generally very good, indicating that the filter material was indeed acceptably homogeneous in pore structure and that the sample diameter was sufficient for a reliable measurement.

In Fig. 10.4 one notices that the onset of flow (at the bubble point) occurs relatively consistently at 30.3±1.5 mbar for Galwick™, Porofil™ and Topor™, and at 35.7 mbar for silicone oil, corresponding to largest pores of 21.1 and

22.4 µm, respectively. The differences between the "wet" curves become more striking however toward smaller pores: while the silicone oil based curve (blue) continues smoothly toward the predetermined endpoint at 400 mbar, the other three curves break off abruptly and prematurely and then join their dry curves. Note also, that the pore size distribution for silicone oil ends around 1 µm, with about 25% of the pores not yet opened at the maximum pressure. (The influence of maximum Δp will be discussed later.)

Interpreted on face value, the above results simply mean that the percentage of fine pores in the media depends on the liquid chosen. Another, more coherent explanation for the observed differences is the likely volatility of three of the working fluids. Volatility effects become apparent when observing the liquid film on the exposed surface of the media during a Δp-scan, as shown in Fig. 10.5 for the case of Porofil™. The inserted photos show the liquid film at different stages of the scan, while the red and blue curves show the raw data for Δp and flow rate vs. scan time.

The sooner this evaporation (transition of the wet surface to dry media) took place during a scan, the narrower the resulting pore size distribution became. In case of Porofil™, this resulted in a cut-off around 9 µm, for Galwick™around 7 µm, while for silicone oil one obtains pore size information down to 1 µm, where the scan ended at Δp_{max}. The discharging of silicone oil filled pores prior to Δp_{max} is also visible from a transition of the wetted media: the glossy surface, immediately after the disappearance of foam, is followed by a decreasing humidity without returning to the completely dry media surface as for Galwick™and Porofil™.

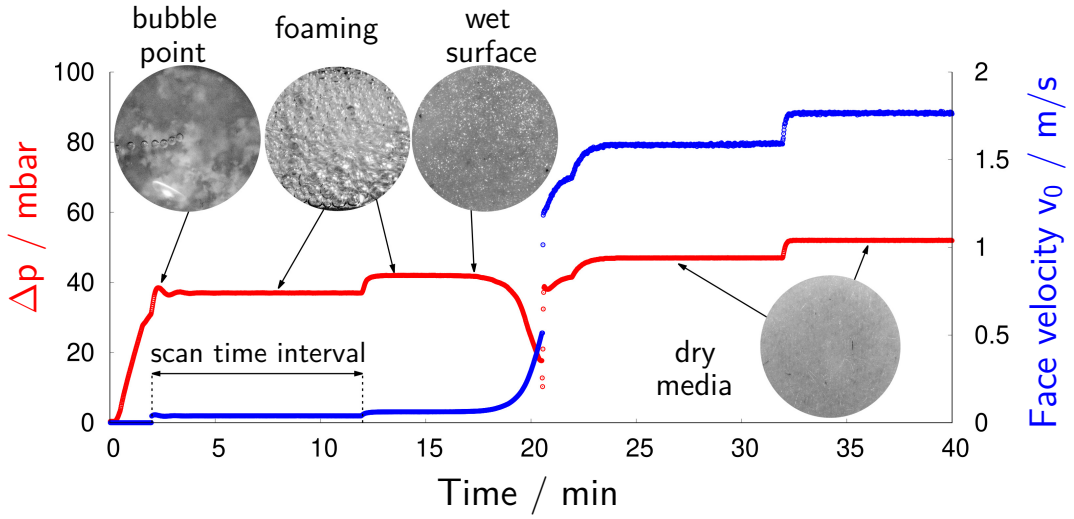

Figure 10.5: Temporal evolution of Δp and face velocity during a Δp-controlled scan. Insets show a top view of the sample surfaces at different stages. Data are for Porofil™, the most volatile liquid.

At the beginning of a wet scan, the media surface was covered by a thin film of liquid. As Δp approaches the bubble point, several thin threads of rising bubbles became visible in the thin liquid layer. A further small increase in flow induced foaming, at first weakly, then more vigorously. With increasing intensity, the foam soon disappeared (due to wall flow and bursting bubbles), leaving behind a humid media surface. A further small increase in Δp and flow caused the remaining liquid in the pores to evaporate completely, leaving behind an apparently dry surface (around t=21 min). This point in time coincided with the steep increase in flow through the media seen in Fig. 10.4b, and the convergence of the wet and the dry curves. The rate of disappearance of the foam was highest for Porofil™(around 40 mbar, as seen in Fig. 10.5) and lowest for the silicone oil, where the foam remained up to about 100 mbar; Galwick™ lay in between at 70 mbar. The abrupt drop in wet Δp down to the level of the dry Δp observed for both Porofil™ and Galwick™, and the resulting sharp increase in air flow through the media are due to the complete evaporation of the liquid at that point in time. The rate of evaporation obviously depends on the volatility, which explains why this phenomenon happens more quickly for Porofil™ but was never observed for silicone oils; and it is dramatically accelerated by the increasing air flow, which explains the sharpness of the transition, in spite of the rather low vapor pressures of these liquids.

As a further consequence of the premature and complete convergence of wet and dry curves in the cases of a volatile liquid, the calculated pore size distribution appears to go down to Q=0. One is thus lead to believe – erroneously – that the complete pore size distribution has been obtained. In fact, some 18 to 20% of pores have been missed at Δp_{max}=400 mbar, as indicated by the blue curve for silicone oil in Fig. 10.4.

More direct evidence for the volatility of the various wetting liquids was collected in a separate experiment, where the weight loss by evaporation of an initially saturated filter sample was measured over a time period of a few hours. To emulate the situation in a porometer more closely, a constant airflow through the filter sample was maintained during the test. The airflow of 5 cm/s resulted in an initial Δp of approximately 50 mbar, which enables flow only in pores >15 μm.

Fig. 10.6 shows the resulting change in saturation with time due to evaporation of liquid from initially fully saturated samples. While the change over several hours was negligible for AK 10 as expected, the other two fluorocarbons behaved according to their volatility, and in accordance with the observations described in Fig. 10.4. Even though the fluorocarbons may have a relatively low vapor pressure at room temperature, the airflow through the samples accelerates the kinetics of the evaporation greatly.

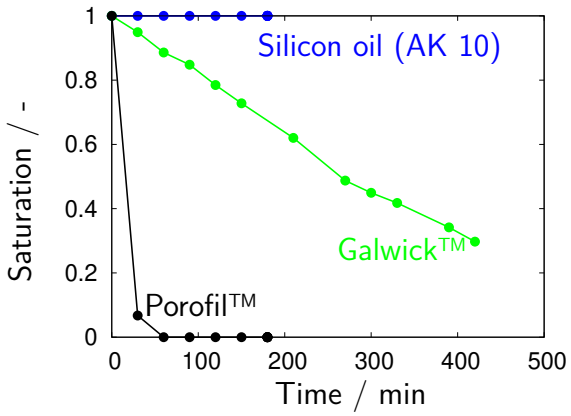

Figure 10.6: Decrease in liquid saturation of filter samples with time due to evaporation. Samples were saturated fully at t=0 with one of the 4 wetting liquids. A flow was maintained through the sample at 5 cm/s face velocity at an initial Δp of 45 mbar corresponding to pore sizes >15 µm.

Based on the gravimetric measurements of Fig. 10.6, the evaporation rates of the three liquids are calculated and compared with corresponding characteristic pore sizes (extracted from Fig. 10.4). The diameter of the largest pores are located within their error bars, while the mean pore sizes (Q=0.5) move towards the largest pores for an increase in the evaporation rate. The slight decrease of the largest pores with the evaporation rate might be an indicator for a better wettability. This minor advantage, however, puts the reliability of the remaining pore size distribution at risk, as the systematic error due to volatility of the wetting liquid increases.

Wetting liquid	Evaporation rate (@ v_0 =0.05 m/s) g/(m^{2}s)	Largest pore µm	Mean pore µm
Wacker™AK 10	< 0.0000	22.6±0.62	5.09±0.11
Galwick™	0.0138	21.51±0.4	7.59±0.08
Porofil™	0.2936	20.48±1.09	11.12±0.07

Table 10.2: Evaporation rates and characteristic pore sizes measured with different wetting liquids. The error of largest/mean pore sizes is based on the standard deviation of 3 measurements.

10.4.2 Influence of the viscosity of the wetting liquid

As mentioned earlier, Yunoki et al. (2004) had already noticed discrepancies between pore size distributions obtained by a porometer when using different wetting fluids, which were attributed to differences in viscosity. We therefore made measurements under identical conditions with three silicone oils having kinematic viscosities between 5 mm^2/s and 100 mm^2/s. Besides their negligible volatility, silicone oils have the added advantage that their viscosity is variable over a wide range via the chain length of the polymer without much change in surface tension (cf. Tab. 10.1).

Fig. 10.7 shows that the resulting pore size distributions differ very little indeed for such a wide range of viscosities. Largest pores for AK 5 and AK 100 were measured at 21.8 µm and 22.5 µm and mean pores range from 4.9 to 5.1 µm. These values do not significantly differ from those of AK 10 given in Tab. 10.2. In fact the differences are hardly visible at the scale of the graphs and certainly much smaller than those caused by volatility effects of some of the working fluids in Fig. 10.2. We therefore think that the discrepancies observed by Yunoki et al. between alcohol, Porofil™ and ethylene glycol (which lie in a much narrower range of viscosities than our silicone oils) may have also been due mostly to volatility effects.

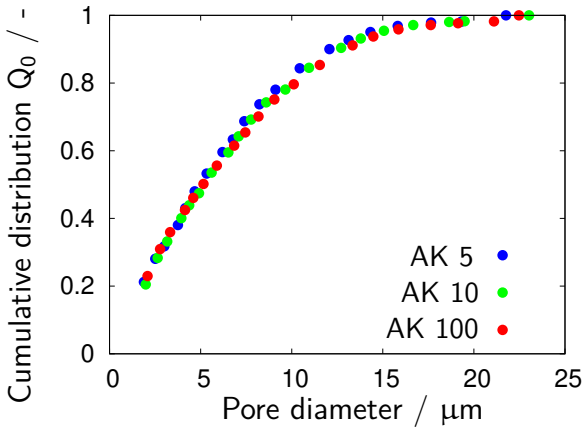

Figure 10.7: Pore size distributions obtained with different viscosity grades of silicone oil (scan time intervals 2 min).

10.4.3 Influence of a variation of scan speed using wetting fluids of different volatility

Due to the evaporation kinetics of a wetting fluid, the scan time is expected to have a significant and non-linear effect on the resulting pore size distribution. This is illustrated in Fig. 10.8 for the two extremes, namely Porofil™ and silicone oil (AK 10), by varying scan time increments between 1 min and 120 min. The resulting total scan times thus range from 25 min to 38 hours!

In case of a volatile liquid such as Porofil™ (blue curves in Fig. 10.8), decreasing the scan time shifts the point of rapid evaporation noticeably toward higher pressures. Although the accessible range of pore sizes is thus extended toward smaller pores, a significant cut-off cannot be avoided even with very rapid scans. For extremely long scanning times, one may even obtain monodisperse pores in the range of the bubble point. (Another indication that the airflow through the media is a major factor in the evaporation rate.)

For a non-volatile wetting fluid such as silicone oil, on the other hand, the effect of scan time on the pore size distribution is comparatively insignificant (green curves in Fig. 10.8). Only a side-by-side comparison between the three

measurements reveals small differences which are reflected more clearly in the raw data of flowrate vs. Δp (Fig. 10.8a). Between about 150 and 250 mbar, the wet curves for scan time intervals of 10 min and 120 min each show a small step-like increase, which is more pronounced for the slowest scan rate. We think this may result from a tiny loss of liquid, which is induced by bubbles that form and burst occasionally on the surface of the media, thereby carrying away a few micro-droplets. This process, called liquid entrainment is known to occur on the surface of wetted fibrous filters *subject to an air flow* (Wurster et al., 2017). In our case it causes a tiny reduction of liquid, which corresponds to a small but noticeable reduction in Δp. The step effect appears in a certain Δp range, which marks the transition of foaming and a wet surface and is therefore also most pronounced (i.e. over a narrower Δp range) for the longest scan time interval. It is understood however, that such extremely slow scans (total scan time > 1 day) are unrealistic in practice.

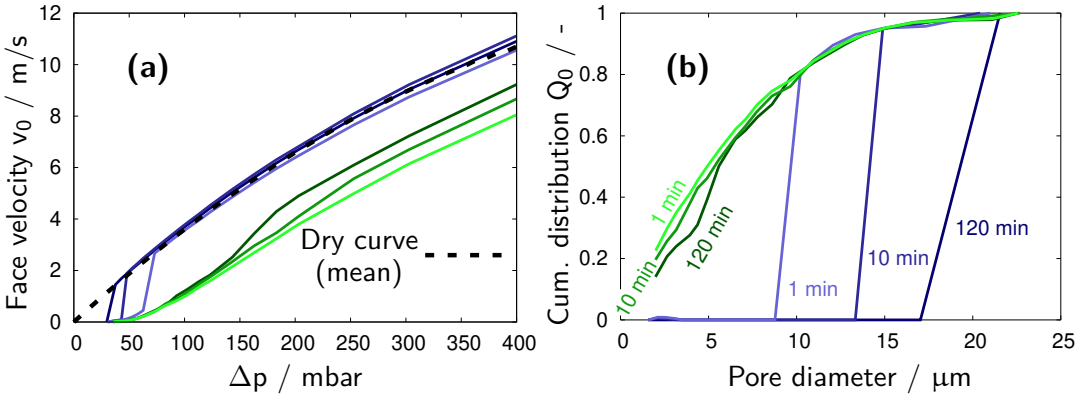

Figure 10.8: Effect of scan time interval (1, 10, 120 min) on the pore size distribution for Porofil™and silicone oil (AK 10). Fig. 10.8a shows the corresponding wet and dry curves.

10.4.4 Influence of the order of the dry and wet scan (only for a non-volatile wetting fluid)

Most commercial porometer software allows a user to choose the order in which the wet and dry measurements are made. Unless otherwise noted, our experiments always start with the "true" dry curve, after which the media are saturated for the wet run. It is indeed tempting to accelerate a pore size distribution measurement by starting with the wet media, blowing them out up to the maximum Δp (which does not necessarily mean completely), and then measuring the "dry" curve on the way down. In the case of a volatile wetting liquid, this may actually work because the liquid has evaporated during the

scan. We will not consider volatile liquids any further however, due to the problems discussed in the preceding sections. Instead we will concentrate on a non-volatile liquid, where this convenient procedure still leads to a systematic error in the resulting pore size distribution, as shown below.

Fig. 10.9a compares a "true" dry curve (in black) to three "wet-before-dry" curves in blue, green and red. The difference between the latter is in the Δp_{max}, which was set to 150, 300 and 400 Pa, respectively. Note first of all that, of necessity, the upper ends of a pair of curves always meet in cases of a "wet-before-dry" run. Consequently, the calculated value of Q automatically becomes zero at the endpoint (the smallest pore). This suggests, erroneously, that one has captured the entire pore size distribution. Secondly, the slopes of these false "dry curves" depend on the chosen Δp_{max}. As a result, the calculated size distributions for different Δp endpoints do not overlap (Fig. 10.9b), as they should, and as they correctly do when using the "true" dry curve (Fig. 10.9b).

Instrument manufacturers are apparently aware of this fact. Occasionally, the argument is made nevertheless, that a wet-before-dry sequence would actually represent the "relevant pore size distribution". Of course, a decision about what part of a pore size distribution is relevant should be made *after* a measurement, and not beforehand. And it should not be preempted by the measurement itself.

10.4.5 Δp controlled scan vs. $\dot{V}$ controlled scan

Porometers are operated either with a pressure controlled or a flow controlled scan sequence. During a scan, the controlling variable is typically changed in small increments at regular time intervals, while the dependent variable "follows". Scan time intervals tend to be as short as possible, in order to speed up the measurement. For that reason, some commercial systems prefer to increase the airflow continually rather than in steps.

Investigations related to the filtration of droplet aerosols and liquid transport of coalesced liquid in fibrous filter media have shown that step changes in airflow rate do not only lead to an opening up of additional pores – a fundamental premise of flow porometry – but also to an internal rearrangement of the liquid, due to the interconnectivity of pore regions. Depending on the viscosity of the liquid and the structure of the media, the rearrangement can take a considerable amount of time, during which the pressure drop asymptotically approaches its new, stable value (Frising et al., 2005; Bredin and Mullins, 2012). The influence of scan sequence and scan rate on porometer measurements was therefore

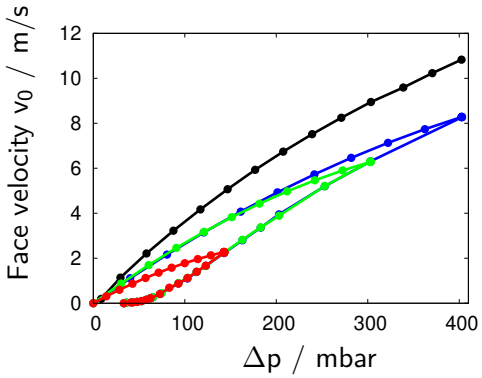

(a) "True" dry curve (black) compared wet-followed-by-dry scans, measured for Δp end-points of 150 mbar (red), 300 mbar (green), and 400 mbar (blue).

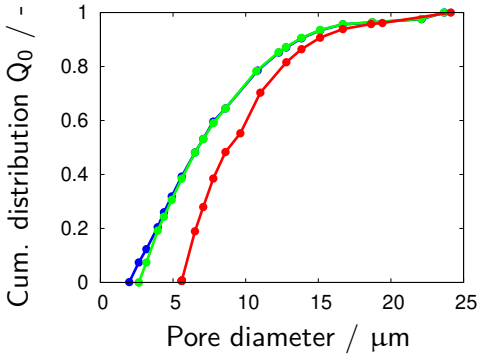

(b) Pore size distributions obtained from wet-followed-by-dry scans resulting in mean pore sizes of 6.7 µm (green, blue) and 8.9 µm (red).

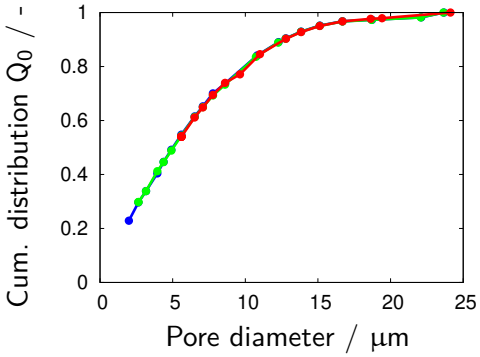

(c) Pore size distributions obtained from the "true" dry curve of Fig. 10.9a resulting in a constant mean pore size of 5 µm

Figure 10.9: Wet-before-dry vs. dry-before-wet sequences for a non-volatile silicone oil

addressed.

Fig. 10.10a shows representative step changes for both $\dot{V}$ controlled (red) and Δp-controlled (blue) measurements and the resulting adjustment of the dependent variable. In each case, the dependent variable takes some time to stabilize. In case of a step change in $\dot{V}$ the pressure drop tends to overshoot due to the way mass flow controllers work, while for a step change in Δp the volumetric flow rate approaches its new value from below. An overshooting Δp will in principle empty out smaller pores than corresponds to the momentary value of $\dot{V}$, and this effect could shift the pore size distribution towards smaller pores. Fig. 10.10 shows however, that the effect is not visible in the pore size distribution, at least not for the glass fiber media used for the test, possibly because the open structure of the media permits these smaller pores to be refilled quickly with liquid from neighboring pores or from above the sample.

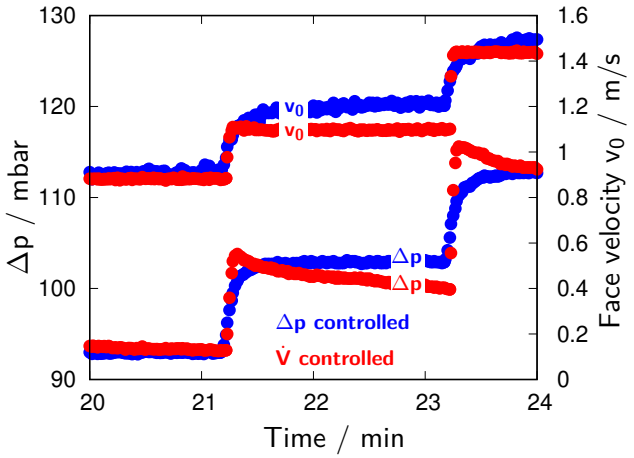

(a) Enlarged sections of raw data for a pressure controlled (blue) and a flow controlled scan (red) using silicone oil AK 10 and a scan time interval of 2 min.

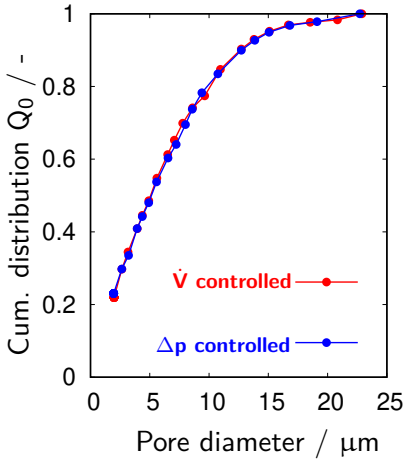

(b) Pore size distributions corresponding to a pressure controlled (blue) and a flow controlled scan (red).

Figure 10.10: Wet-before-dry vs. dry-before-wet sequences for a non-volatile silicone oil

10.5 Summary and conclusions

Error sources in capillary flow porometry applied to microfibrous media were investigated experimentally. This well-established method is based on the gradual displacement of a saturating liquid from inside the media by gradually increasing the differential pressure of an air flow. The pore size distribution is obtained on the basis of classical capillary theory from the corresponding flow rates through the dry and partially "blown out" media.

Among the factors (i.e. potential error sources) investigated were

- the volatility and viscosity of various wetting liquids,
- the scan speed,
- the order of the wet and dry scans (i.e. dry before wet, or wet before dry),
- Δp controlled scans vs. $\dot{V}$ controlled scans.

Experiments were done with a porometer of in-house design (cf. Fig. 10.2), in order to be able to access and control all process variables. Four different wetting fluids were investigated (cf. Table 10.1). For better comparison, all measurements were made with the identical batch of glass microfiber media.

The by far largest source of errors was due to the volatility of the fluorocarbon wetting fluids used in the study. The vapor pressures of these liquids are generally quite low (exact data are difficult to obtain). Nevertheless, even the slightest air flow through the media – beginning with the biggest pores – causes these fluorocarbons to evaporate more or less quickly and completely

during a scan. The implications for the resulting pore size distribution are enormous, not only with regard to a variation of scan speed and the order of the scans, but also for a several other parameters not investigated in this chapter, such as the initial amount of supernatant liquid (which has to evaporate), or ambient pressure and temperature. Evaporation during the measurement of the wet curve results in a complete and premature convergence of the wet and dry-curves, and thus in a substantial narrowing of the pore size distributions. Pore sizes below about 5 μm are typically not detected. These volatility effects provided a sufficient explanation for differences in pore size data observed between various commercial porometers.

Evaporation effects were not observed in the case of silicone oil based wetting liquids. For these non-volatile liquids, the influence of viscosity on the pore size distribution was investigated in a range of 1:20. This influence was found to be very small, and the remaining differences were presumably due mainly to a gradual loss of liquid from fine, not yet emptied pores. This loss may be caused by some splattering of liquid drops at higher air flows and therefore seems to depend on the length of the scan time interval. The effect deserves a more detailed investigation in future work. However, intervals of 2 minutes had no appreciable influence on the accuracy.

It was shown that dry-before-wet sequences deliver consistent pore size distributions that are independent of the maximum Δp of the scan. Furthermore, there was no appreciable influence on the pore size distribution, whether a scan was Δp controlled or flowrate controlled.

In final conclusion, volatile wetting liquids may have the advantage of a better wettability for investigations of the largest pores in fibrous media. This small advantage is outweighed however, by the errors introduced with regard to the almost arbitrary shape of the pore size distribution. The consistent use of non-volatile silicone oils is therefore recommended and will make it easier to compare published data.

Acknowledgements

The authors would like to thank Atlas Copco Airpower n.v. for funding and support of this work as well as Topas GmbH for lending us their equipment for measurements cited in this paper.

11

Summarizing conclusions

The present thesis builds on the recently developed "Film-and-Channel-Model", a semi-empirical model that provides mechanistic explanations for key functional aspects of mist filters, especially its pressure drop during oil loading. It extends that model to additional important aspects of their functioning, such as the influence of flow velocity variations on filter operation, and the relationship between filter loading and filter efficiency. It investigates the so-called (and generally assumed) steady-state mode of filter operation and elucidates a new phenomenon termed "creep" in steady state. Also, it establishes relationships between these mechanisms and filter structure and, for that purpose, improves a classical technique called capillary flow porometry often used for the characterization of porous media.

The investigated phenomena are *transitional* in the sense that changes in the filter performance occur during initial filter loading, under intermittent flow, and (involuntarily) during operation beyond the so-called steady state. Moreover, they are common to all mist filters and relevant for their practical performance, and up to now poorly understood.

The Film-and-Channel-Model for the evolution of Δp

The thesis validates the Film-and-Channel-Model not only for a wider range of working conditions and filter media than earlier work, but also provides answers and guidelines for its applicability in light of transitional phenomena. Hithereto unknown dependencies between the pressure drop components, Δp_{jump} and

$\Delta p_{channel}$, and parameters such as face velocity, loading rate, and loading time have been revealed and explained. Their underlying causes are discussed in detail.

For wettable filter media, the most common of media used in mist filtration, it is shown that the film contribution to the pressure drop, Δp_{jump}, is independent of filter operating conditions and solely caused by the capillary exit pressure of the largest pores. Therefore, Δp_{jump} can be predicted via the bubble point. Furthermore, it can be concluded for all media investigated, that the number of largest pores suffices to cope with the range of air flows common to most mist filter applications. Explanations advanced by other studies (Chang et al., 2016, 2017) suggesting a dependence of Δp_{jump} on the film thickness were not confirmed, but linked to erroneous assumptions for the film thickness and a misinterpretation of experiments related to the use of drainage layers.

The other key component of the wet pressure drop, the so-called excess channel Δp, i.e. $\Delta p_{channel}$ - Δp_0, is shown to be equally independent of the filter face velocity, but to increase with the oil loading rate because the filter requires more Δp to transport more liquid through the medium. The independence of the excess channel Δp on the face velocity (for a constant oil loading rate) – a most unusual phenomenon for flow through porous media – is due to the observed, concurrent decrease in internal saturation with the air flow. One may assume that the saturation adjusts itself according to flow rate in order to provide the Δp necessary for the liquid transport. Image analyses revealed that this adjustment in saturation takes place via the channel size and not with the number of channels per area. The number of channels remains constant probably because the deposition of oil aerosol occurs uniformly across the filter surface, and the transport of liquid requires a minimum number of channels per area. This illustrates very well that the coalescence of channels does not play a significant role in the respective filter region.

The thesis also elucidates fundamental differences in the operating behavior between filters that are initially dry and those that are initially pre-saturated (i.e. totally filled with oil). Pre-saturated filters do not show the oil channel structure typical for filters that are initially dry, and the absence of visible oil channels results in a more homogeneous liquid distribution (and hence a higher Δp). Based on the classical model relating Δp to the structure of random porous media, a simple expression is presented in Chapter 9 to relate the internal saturation, $\Delta p_{channel}$, to the homogeneity of deposited/transported oil. It provides a reasoned upper and lower limit for Δp related to a totally heterogeneous vs. a perfectly homogeneous liquid distribution. The expression is therefore a useful tool for the development and optimization of mist filters.

Furthermore, it is shown that the internal saturations of both, pre-saturated and initially dry, filters converge to become nearly identical at low velocities, but diverge toward higher velocities, thereby leaving an increasing saturation gap between the two starting conditions. Pre-saturated media retain some of the liquid in their smallest pores during the initial discharge of bulk liquid as well as in the subsequent steady state. This mostly static liquid is finely dispersed and leads to a better wettability on the meso-scale which prevents the formation of oil channels. Therefore, the oil transport in pre-saturated filters takes place across the complete cross-section and not only in the wet channel regions as in initially dry filters.

The applicability of the Film-and-Channel-Model to the long-term operation of mist wettable and non-wettable filters, and in particular the origin of certain "instabilities" observed during their steady state were investigated in experiments exceeding by far the time required to reach a steady operation. It is found that pre-saturated filters reach their steady operation typically relatively rapidly and then maintain a very constant and stable Δp during continued loading. Initially dry media on the other hand are subject to a further, slow increase ("creep") of both saturation and Δp, that goes far beyond the formation of films and channels marking the onset of the initial steady state. The underlying cause for this transitional phenomenon is a gradual accumulation of very fine droplets of coalesced oil in the depth of the filter between the oil channels. As a result of this continued accumulation, the saturation level of initially dry filters approaches that of their pre-saturated counterparts asymptotically in time, however without showing complete convergence in terms of Δp, because the channels remain preserved. The accumulation of additional liquid during the creep can occur either very fast but with little impact on the overall Δp (as in case of coarse media), or with a huge impact on Δp but over quasi-infinite loading times beyond the feasibility of any laboratory experiment, as is typical for fine and highly efficient media grades. Therefore, it is recommendable to use the onset of drainage (i.e. the "classical" definition) as a common reference point for the steady state.

These findings of fundamental differences between the creep behavior in coarse and fine media help to reconcile apparent contradictions among earlier observations related to the steady state of pre-saturated vs. initially dry media: For example Kampa et al. (2015) did not see a convergence in Δp for fine filter media, whereas Mead-Hunter et al. (2013) found a convergence for coarser media.

Besides the investigation of transitional phenomena during continuous experiments under steady operating conditions, this thesis also studied changes of saturation and Δp during discontinuous filtration. It is shown for both wettable and non-wettable media that a step increase in Δp after one or more flow interruptions (already observed in previous work) is due to a mere redistribution of oil at a constant saturation. Another type of experiment was able to demonstrate for that initially dry filters can also reach a steady state very similar to that of pre-saturated media (i.e. at a significantly higher Δp and S), by temporarily lowering the face velocity to a very low level. Mist filters therefore have three different steady states, depending on how they are operated and how long one is willing to wait: a "pre-saturated steady state", a first "dry steady state" (the conventional one), and an asymptotic steady state at least with regard to saturation. Among these, the pre-saturated steady state is not purely academic because it represents the worst and very possible scenario for mist filters in terms of S and Δp.

The Film-and-Channel-Model for efficiency

This thesis extends the Film-and-Channel-Model beyond issues of S and Δp, to include the efficiency of a mist filter, thereby proving the universal usefulness of this model for the behavior of such filters. It is shown that both the oil channel region and the oil film make individual and very specific contributions to the overall filter efficiency. These contributions can be quantified separately by a newly developed experimental technique and used to predict the total filter efficiency as a function of filter construction. This work also casts light on fundamental differences between wettable and non-wettable, as well as low vs. high-efficient mist filters.

In particular, the oil film has proven for all investigated filter media to be a remarkably good inertial separator for aerosol particles with 50% cut-off values down to 125 nm. This finding explains earlier observations of a gradual decrease in efficiency during filter loading followed by a significant efficiency increase coinciding with film formation, and therefore also differences between wettable and non-wettable media.

The efficiency loss due to oil accumulation in the channel section is shown to occur on both sides of the MPPS for wettable and non-wettable media. A major impact of the interstitial velocity increase on the deposition, as commonly assumed in the literature (e.g. Payet et al., 1992; Conder and Liew, 1989; Raynor and Leith, 2000), can thus be ruled out as an explanation for the changes in efficiency. Rather, such an assumption was probably linked to neglecting the film efficiency as a separate contributor.

Moreover, the extended Film-and-Channel-Model is now able to reconcile seeming contradictions between published fractional efficiency data of low and high efficient filters. A crossover between the efficiency curves of dry and wet filters is characteristic only for filters of a low efficiency, i.e. for coarse media and/or filters with few layers where the film contributes appreciably to the overall efficiency and an enhanced deposition of larger droplets. For more efficient (multi-layered) filters, the film contribution becomes relatively insignificant while the channel section dominates the overall efficiency. The result is an absence of the crossover between dry and wet fractional efficiencies and a reduced efficiency for both smaller and larger droplets.

Finally, measurements of the total downstream number concentration revealed that re-entrainment gradually gains significance with operating time. It is in fact the re-entrainment – and not primarily the efficiency of the filter medium – that poses the lower limit for particle concentration on the downstream side of a high-end filter.

Media characterization

The last part of this thesis is dedicated to the accuracy of capillary flow porometry as a tool for the characterization of glass microfiber filter media. This technique models a porous structure (such as a filter medium) as a system of parallel pores and derives the pore size distribution by scanning Δp vs. volumetric flow rate for the dry and fully saturated ("pre-saturated") media. Capillary flow porometers are widely commercialized and typically use fluorocarbons as a wetting liquid. Additional measurements with other, not perfectly wetting, liquids allow an evaluation of parameters such as contact angles or capillary exit pressures.

Despite the low vapor pressure of fluorocarbons, it is shown that these wetting liquids evaporate appreciably during a scan due to the added air flow through the fibrous structure. This leads to uncontrolled artifacts with regard to the effectively measured pore size distribution and a characteristic cut-off of the distribution at the lower end. Through a variation of porometer operation one can easily obtain arbitrary pore size distributions at some point downward from the largest pore.

Reliable pore size distributions, on the other hand, were achieved with non-volatile silicone oils. Measurements with this type of wetting liquid are more advantageous thanks to their independence from operation parameters and viscosity. Since silicone oils cannot be completely displaced from fibrous media during the scan of a wet sample, it becomes crucial to perform the dry scan before the wet scan.

12

Outlook

The growing usefulness of the Film-and-Channel-Model for mist filtration, including several contributions made to it in the course of this thesis project, underlines the fact that we are now able to explain macroscale filter behavior (notably Δp and efficiency) by *structural attributes on the mesoscale*, such as the distribution of liquid (film and channels) and pore sizes of the filter medium. Moreover, the arguments connecting these mesoscale attributes to filter operation and structure (and hence to Δp and efficiency) are physically satisfactory – although semi-quantitative – and consistent with each other. This fairly complete picture tends to gloss over the fact that certain, perhaps more subtle but nevertheless important questions remain unanswered with regard to how exactly internal structure and macroscopic performance interact at different scales to produce the filter behavior observed.

A perfect case in point is the efficiency of mist filters which was modeled in Chapter 8 on the basis of the mesoscale Film-and-Channel-Model. Instead, it would have appeared natural to follow in the footsteps of earlier work (notably by Charvet et al., 2010) and try an approach based on the single-fiber concept, a time-honored microscale model that has been applied with much success in the past to predict the behavior of fibrous filters during particle loading. Unfortunately, the microscale has so far not been accessible experimentally and representative structural data related to oil loaded single fibers are not available for either wettable or non-wettable filter media. On the other hand the Film-and-Channel-Model for the efficiency not only demonstrated its predictive

value for technical applications, but also provided access to the required and readily available validation data. Bringing the single-fiber theory and the validated Film-and-Channel-Model together would be an important milestone in moving the state of oil mist filtration modeling forward.

Another area where our physical picture is now plausible and consistent, although somewhat hazy in detail, are the interactions between the liquid film (especially on the upstream face of oleophobic media), the air flow, and the fibrous structures of the media. There have been considerable efforts and some success – the success of the Film-and-Channel-Model – by Kampa, Wurster, and in the context of this thesis, to describe the role of the film and its pores to the filter pressure drop and the re-entrainment of droplets. But it is still not entirely clear how the air flow is distributed across the open pores and how those pores are actually activated. Understanding this may help to refine the filter structure in ways that might allow a reduction of Δp_{jump} and re-entrainment of liquid into the air flow.

And finally, there are indications as well as possible physical reasons summarized below, why the behavior of oil films formed on wettable and non-wettable media (and hence Δp_{jump}) is not exactly symmetric. Thus, an important tenet of the basic Film-and-Channel-Model, namely the independence of Δp_{jump} of operating conditions needs to be revised in case of non-wettable media.

It was not always possible to discuss these issues in the preceding chapters, without losing focus. They will be briefly taken up in to following, by gathering some arguments and pointing out certain ideas, but without attempting to give any definitive answers.

The impact of (non-)wettability on the channel efficiency

In Chapter 8, an experimental method was presented to determine and study the "internal" efficiency of an oil mist filter (i.e. the efficiency of a typical channel layer) without the bias and interference of external factors such as the film efficiency. As part of this study it was found that in the size range above 100 nm the efficiency of non-wettable media was considerably higher than in wettable media of about the same grade (cf. Fig. 8.6). Chapter 8 provided two possible explanations for this significant and consistently observed phenomenon. Both are fully capable of explaining the data, but it is neither clear if the underlying mechanisms can co-exist in real filter media nor which one prevails over the other. The two hypotheses, one on the scale of a single fiber and the other on the mesoscale of the Film-and-Channel-Model, were too complex to be discussed in the course of Chapter 8 and are therefore outlined in more detail in the following.

On the ***mesoscale*** of the oil channels, the observed differences in efficiency between wettable and non-wettable media can be linked to the inhomogeneity inherent to wet laid filter media and its influence on the channel formation. This inhomogeneity, commonly referred to as "cloudiness" (e.g. in Lehmann et al., 2013), is readily visible due to local variations of transmitted light, as illustrated below in Fig. 12.1 for a wettable media layer. Brighter regions are due to a lower content of fibers whereas darker regions represent areas of high fiber density and thus also of higher capillary forces to attract the oil. The superposed green outlines in this figure are the result of a separate evaluation by image analysis of the exact same piece of filter medium, and represent the boundaries of the oil channels. A comparison of the green channel contours and the greyscale picture in the background of Fig. 12.1 shows that the oil channels form mainly in the dark regions, i.e. regions of a higher fiber density. In other words, channels in a wettable medium form in the most densely packed regions of higher capillarity. For non-wettable media on the other hand, it seems reasonable that the channels would occupy regions in the least dense regions because this helps to minimize the filter surface energy during loading. Applied to the issue of efficiency loss with oil loading, non-wettable media would lose fewer fibers (or less effective fiber length) than wettable media and consequently retain more of their initial efficiency.

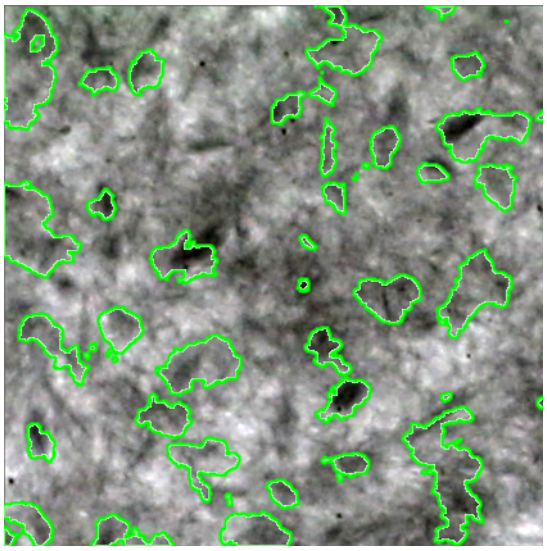

Figure 12.1: Image of a dry and wettable media layer with enhanced contrast on a grey scale ranging from black (high weight density of fibers) to white (low density). Green contours indicate the occurrence of channels when the same media layer is loaded with oil mist.

On the ***microscale*** of individual fibers, it is the morphology of liquid deposits which is expected to differ for wettable and non-wettable fiber surfaces, and must be taken into account as another reason to explain differences in efficiency. Oil on wettable fibers is known to spread and form barrel-shaped drops (Mead-Hunter et al., 2014) which cause more effective fiber loss than clam-shell shaped drops (of same volume) on non-wettable fibers. The barrel shape might furthermore lead to less inertial deposition of droplets because the oil progressively increases

the fiber diameter beginning from the contact line with the fiber. In conclusion, such effects should entail significant differences between wettable and non-wettable media in effective Stokes numbers, the most important parameter for the droplet sizes in question.

New data are needed to quantify the respective efficiency contributions and help to decide which of the two aforementioned explanations is primarily behind the efficiency gap of non-wettable and wettable filters. One promising starting point for new experiments is to prepare thin arrays of homogeneously and heterogeneously distributed fibers of different wettability. These arrays should then be dipped briefly into a suitable liquid to create a liquid morphology characteristic of the respective structure. The mobility of these liquid structures could be suppressed by "freezing" them by the polymerization technique invented by Kampa et al. (2014). Such "frozen arrays" could not only be used for a better characterization of the liquid morphology and channel formation but also to measure the resulting efficiencies of those structures.

The dynamic Δp_{jump} of non-wettable filters

Chapters 6 and 7 have shown for a wide range of *wettable* filter media, that Δp_{jump} is independent of the most important operating conditions; moreover it is independent of the thickness of the (downstream) oil film, which increases from top to bottom because it also functions as the principal path of oil drainage. For *non-wettable* filter media on the other hand, the contribution of Δp_{jump} does not seem to be entirely independent of the operating conditions. In fact, Δp_{jump} has been found to decrease with face velocity (Kolb et al., 2015) and to increase with oil loading rate (Chang et al., 2018a). The exact reason for this dynamic behavior remains unclear but may have to do with differences in the kinetics of film formation on the upstream vs. downstream filter face.

In case of non-wettable filters, the film thickness – and hence Δp_{jump} – results from the balance between oil accumulation (i.e. loading rate) and depletion of "film oil" under the influence of the air stream. Both face velocity and oil loading rate seem to determine the point in time when the phase of film build-up ends and the transport of "film" oil into the filter begins. More precisely, the loading rate contributes to the film build-up while the face velocity governs the oil transport away from the film. As a consequence, the film on the face of a non-wettable filter probably becomes thicker for higher loading rates or lower face velocities and, more interestingly, Δp_{jump} of such filters would correlate with the film thickness. An important and interesting starting point for future work therefore would be to clarify, whether the dynamic Δp_{jump} of non-wettable media is linked to a variation in film thickness and how the capillary entry pressure fits into this picture.

The air flow through the liquid film

Even though the extent to which the liquid film contributes to Δp and efficiency has been clarified in this thesis, important details about the underlying physics are still missing. Specifically, the number of activated and open pores in the film and consequently the mean velocity through a single pore have not been identified yet. Knowledge of the flow field in and around the pores would greatly contribute to a better understanding of droplet deposition and possible frictional losses of the air flow in the film region.

An lower limit for the number of open pores can be estimated from the rate of bursting bubbles. Wurster et al. (2017) report bubble rates of about 5000 $cm^{-2}s^{-1}$ with a mean bubbling frequency of about 50 Hz. This amounts to about 100 bubbles (and thus intermittently open pores) per square centimeter of filter surface. The actual number of open pores is probably much higher though, because this estimate would lead to a higher than critical flow velocity through the pores, which is highly unlikely. Also the number of permanently open pores is not accounted for.

Here as well, an experimental approach based on the aforementioned polymerization technique could be helpful. “Freezing” the film would permit counting and analyzing its open pores. Quantitative analyses of several films, frozen at variable face velocities, could also answer a simple but yet unanswered question: Does the film react to higher air flows by adjusting the number of open pores or with a higher air flow within the pores?

References

Abishek, S., A. J. C. King, J. Schuler, G. Kasper, H.-J. Schmid, and B. J. Mullins (2018). Representative Domain Size for the Simulation of Coalescence Filtration in Nonwoven and Foam Media. *Separation and Purification Technology 207*, 344–352.
(Cited on page 23)

Agarwal, C., A. K. Pandey, S. Das, M. K. Sharma, D. Pattyn, P. Ares, and G. A. (2012). Neck-size distributions of through-pores in polymer membranes. *Journal of Membrane Science 415*, 608–615.
(Cited on page 120)

Aggarwal, P., H. D. Tolley, and M. L. Lee (2012). Characterizing Organic Monolithic Columns Using Capillary Flow Porometry and Scanning Electron Microscopy. *Analytical Chemistry 84*, 247–254.
(Cited on pages 15 and 121)

Agranovski, I., T. Myojo, R. Braddock, and D. Jarvis (2002). Inclined wettable filter for mist purification. *Chemical Engineering Journal 89*, 229–238.
(Cited on pages 25 and 86)

Agranovski, I. E. and R. D. Braddock (1998). Filtration of liquid aerosols on wettable fibrous filters. *AIChE Journal 44*, 2775–2783.
(Cited on pages 27, 71 and 94)

Agranovski, I. E., R. D. Braddock, N. P. Kristensen, S. Crozier, and T. Myojo (2001). Model for Gas-Liquid Flow through Wet Porous Medium. *Chemical Engineering & Technology 24*, 1151–1155.
(Cited on pages 25 and 86)

Agranovski, I. E., T. Myojo, R. D. Braddock, and D. Jarvis (2001). Combined wettable/non-wettable filter for mist purification. *Chemical Engineering &*

Technology 24(3), 287–292.
(Cited on pages 18 and 91)

Andan, S., S. I. Hariharan, and G. G. Chase (2008). Modeling of saturation in coalescence filtration. In *American Filtration and Separations Society, 22th annual conference, Valley Forge (PA), USA*.
(Cited on page 22)

Bach, B. and E. Schmidt (2007). Influence of leaks in surface filters on particulate emissions. *Journal of Hazardous Materials 144*, 673–676.
(Cited on page 81)

Barry, D. A., L. Wissmeier, J.-Y. Parlange, G. C. Sander, and D. A. Lockington (2009). Comment on "An analytic solution of capillary rise restrained by gravity" by N. Fries and M. Dreyer. *Journal of Colloid and Interface Science 338*, 293–295.
(Cited on page 12)

Bitten, J. F. and E. G. Fochtman (1971). Water Distribution in Fiber-Bed Coalescers. *Journal of Colloid and Interface Science 37*(2), 312–317.
(Cited on page 22)

Bredin, A. and B. J. Mullins (2012). Influence of flow-interruption on filter performance during the filtration of liquid aerosols by fibrous filters. *Separation and Purification Technology 90*, 53–63.
(Cited on pages 4, 22, 29, 30, 95, 102, 113 and 132)

Briscoe, B. J., K. P. Galvin, P. F. Luckham, and A. M. Saeid (1991). Droplet coalescence on fibres. *Colloids and Surfaces 56*, 301–312.
(Cited on page 71)

Brown, R. C. (1993). *Air filtration: An integrated approach to the theory and applications of fibrous filters*. Pergamon.
(Cited on page 64)

Callé-Chazelet, S., T. Frising, D. Thomas, and D. Bémer (1996). Filtration continue et discontinue d'un aérosol liquide et de mélanges d'aérosols solide et liquide par un filtre à fibres. In *1ères Journées Filtration des Aérosols*, Volume 176.
(Cited on pages 95 and 96)

Calvert, S., I. L. Jashnani, and S. Yung (1974). Entrainment separators for scrubbers. *Journal of the Air Pollution Control Association 24*(10), 971–975.
(Cited on page 28)

Calvo, J. I., A. Hernández, P. Prádanos, L. Martínez, and W. R. Bowen (1996). Pore Size Distributions in Microporous Membranes II. Bulk Characterization of Track-Etched Filters by Air Porometry and Mercury Porosimetry. *Journal of Colloid and Interface Science 176*, 467–478.
(Cited on pages 15, 65 and 121)

Carman, P. C. (1956). *Flow of gases through porous media*. Academic Press, New York.
(Cited on pages 11, 56 and 59)

Carroll, B. J. (1976). The Accurate Measurement of Contact Angle, Phase Contact Areas, Drop Volume, and Laplace Excess Pressure in Drop-on-Fiber Systems. *Journal of Colloid and Interface Science 57*(3), 488–495.
(Cited on pages 9 and 10)

Cassie, A. B. D. and S. Baxter (1944). Wettability of porous surfaces. *Transactions of the Faraday Society 40*, 546–551.
(Cited on page 9)

Chang, C. (2019). personal communication.
(Cited on page 65)

Chang, C., Z. Ji, and J. Liu (2017). The effect of a drainage layer on the saturation of coalescing filters in the filtration process. *Chemical Engineering Science 160*, 354–361.
(Cited on pages iii, xi, 4, 20, 35, 59, 96 and 138)

Chang, C., Z. Ji, and J. Liu (2018a). The effect of a drainage layer on saturation and liquid distribution of oleophobic coalescence filters. *Separation and Purification Technology 194*, 355–361.
(Cited on pages 4, 20, 22, 27, 95, 96 and 146)

Chang, C., Z. Ji, and J. Liu (2018b). Pressure drop and saturation of nonwettable coalescing filters at different loading rates. *AIChE Journal 64*, 180–185.
(Cited on page 19)

Chang, C., Z. Ji, and F. Zeng (2016). The effect of a drainage layer on filtration performance of coalescing filters. *Separation and Purification Technology 170*, 370–376.
(Cited on pages iii, xi, 4, 20, 22, 35, 59, 60, 64 and 138)

Charvet, A., Y. Gonthier, A. Bernis, and E. Gonze (2008). Filtration of liquid aerosols with a horizontal fibrous filter. *Chemical Engineering Research and Design 86*(6), 569–576.
(Cited on pages 18 and 29)

Charvet, A., Y. Gonthier, E. Gonze, and A. Bernis (2010). Experimental and modelled efficiencies during the filtration of a liquid aerosol with a fibrous medium. *Chemical Engineering Science 65*, 1875–1886.
(Cited on pages 25, 86, 94 and 143)

Chen, F., Z. Ji, and Q. Qi (2018). Effect of pore size and layers on filtration performance of coalescing filters with different wettabilities. *Separation and Purification Technology 201*, 71–78.
(Cited on pages 20 and 23)

Clarenburg, L. A. and H. W. Piekaar (1968). Aerosol filters – I Theory of the pressure drop across single component glass fibre filters. *Chemical Engineering Science 23*(7), 765–771.
(Cited on page 11)

Conder, J. R. and T. P. Liew (1989). Fine mist filtration by wet filters – II: Efficiency of fibrous filters. *Journal of Aerosol Science 20*, 45–57.
(Cited on pages 26, 27, 71, 84 and 140)

Contal, P., D. Simao, J. Thomas, T. Frising, S. Callé, J. Appert-Collin, and D. Bémer (2004). Clogging of fiber filters by submicron droplets. Phenomena and influence of operating conditions. *Journal of Aerosol Science 35*, 263–278.
(Cited on pages 4, 18, 19, 21, 22, 27, 86, 88, 95 and 96)

Darcy, H. P. G. (1856). *Les fontaines publiques de la ville de Dijon*. Victor Dalmont, Paris.
(Cited on page 59)

Davies, C. N. (1973). *Air filtration*. Academic Press, London.
(Cited on pages 8, 56, 74 and 98)

Dawar, S. and G. Chase (2008). Drag correlation for axial motion of drops on fibers. *Separation and Purification Technology 60*, 6–13.
(Cited on page 108)

Dawar, S. and G. Chase (2010). Correlations for transverse motion of liquid drops on fibers. *Separation and Purification Technology 72*, 282–287.
(Cited on page 108)

de Gennes, P.-G., F. Brochard-Wyart, and D. Quéré (2004). *Capillarity and Wetting Phenomena: Drops, Bubbles, Pearls, Waves*. Springer, New York.
(Cited on page 10)

Dettre, R. H. and R. E. Johnson (1969). Surface Tensions of Perfluoroalkanes and Polytetrafluoroethylene. *Journal of Colloid and Interface Science 31*,

568–569.
(Cited on page 9)

Dixon, J. S. (1998). The effects of wetting fluid vapor pressure on capillary flow porometry. In *Membrane Technology/Separations Planning Conference*, pp. 219–226.
(Cited on pages 16 and 121)

Dullien, F. A. L. (1992). *Porous Media: Fluid Transport and Pore Structure*. Academic Press, San Diego.
(Cited on page 13)

Dullien, F. A. L. and G. K. Dhawan (1974). Characterization of Pore Structure by a Combination of Quantitative Photomicrography and Mercury Porosimetry. *Journal of Colloid and Interface Science 47*(2), 337–349.
(Cited on page 14)

El-Dessouky, H. T., I. M. Alatiqi, H. M. Ettouney, and N. S. Al-Deffeeri (2000). Performance of wire mesh mist eliminator. *Chemical Engineering and Processing 39*(2), 129–139.
(Cited on page 28)

Endo, Y., D.-R. Chen, and D. Y. H. Pui (1998). Effects of particle polydispersity and shape factor during dust cake loading on air filters. *Powder Technology 98*(3), 241–249.
(Cited on page 11)

Erbe, F. (1933). Die Bestimmung der Porenverteilung nach ihrer Größe in Filtern und Ultrafiltern. *Kolloid-Zeitschrift 63*, 277–285.
(Cited on pages 14 and 120)

Fairs, G. L. (1958). High efficiency fibre filters for the treatment of fine mists. *Transactions of the Institution of Chemical Engineers 36*, 2476–485.
(Cited on page 71)

Frising, T., V. Gujisaite, D. Thomas, S. Callé, D. Bémer, P. Contal, and D. Leclerc (2004). Filtration of solid and liquid aerosol mixtures: pressure drop evolution and influence of solid/liquid ratio. *Filtration & Separation 41*(2), 37–39.
(Cited on page 95)

Frising, T., D. Thomas, J. C. Appert-Collin, S. Callé-Chazelet, and P. Contal (2005). Influence of liquid aerosol stop-and-go on the performance of fibrous filters. *Filtration 5*, 286–294.
(Cited on pages 18, 29 and 95)

Frising, T., D. Thomas, D. Bemer, and P. Contal (2005). Clogging of fibrous filters by liquid aerosol particles: Experimental and phenomenological modelling study. *Chemical Engineering Science 60*(10), 2751–2762.
(Cited on pages 4, 18, 20, 27, 46, 51, 54, 56, 71, 86, 94, 95, 96 and 132)

Gac, J. M. (2015). A Simple Numerical Model of Pressure Drop Dynamics During the Filtration of Liquid Aerosols on Fibrous Filters. *Separation Science and Technology 50*(13), 2015–2022.
(Cited on pages 18 and 51)

Golkarfard, V., B. J. Mullins, A. J. C. King, and S. Abishek (2016). Numerical Study of Liquid Transport in Realistic Filter Media. In *20th Australasian Fluid Mechanics Conference, Perth, Australia*.
(Cited on page 23)

Gong, J., M. L. Stewart, A. Zelenyuk, A. Strzelec, S. Viswanathan, D. A. Rothamer, D. E. Foster, and C. J. Rutland (2018). Importance of filter's microstructure in dynamic filtration modeling of gasoline particulate filters (GPFs): Inhomogeneous porosity and pore size distribution. *Chemical Engineering Journal 338*, 15–26.
(Cited on page 11)

Green, W. H. and G. A. Ampt (1911). Studies on soil phyics. *The Journal of Agricultural Science 4*(1), 1–24.
(Cited on page 12)

Gummerson, R. J., C. Hall, W. D. Hoff, R. Hawkes, G. N. Holland, and W. S. Moore (1979). Unsaturated water flow within porous materials observed by nmr imaging. *Nature 281*(5726), 56.
(Cited on page 13)

Hernández, A., J. I. Calvo, P. Prádanos, and F. Tejerina (1996). Pore size distributions in microporous membranes. A critical analysis of the bubble point extended method. *Journal of Membrane Science 112*, 1–12.
(Cited on pages 16 and 121)

Hoferer, J., M. J. Lehmann, E. H. Hardy, J. Meyer, and G. Kasper (2006). Highly Resolved Determination of Structure and Particle Deposition in Fibrous Filters by MRI. *Chemical Engineering & Technology 29*, 816–819.
(Cited on page 121)

Holm, C. E. (2001). Inertial gas-liquid separator having an inertial collector spaced from a nozzle strucure. US patent 6290738 B1.
(Cited on page 81)

Hotaling, N. (2015). Diameterj. `https://imagej.net/DiameterJ`. Accessed: 2018-10-21.
(Cited on page 7)

Hotaling, N. A., K. Bharti, H. Kriel, and C. G. Simon (2015). DiameterJ: A validated open source nanofiber diameter measurement tool. *Biomaterials 61*, 327–338.
(Cited on page 7)

Hotz, C. J., R. Mead-Hunter, T. Becker, A. J. C. King, S. Wurster, G. Kasper, and B. J. Mullins (2015). Detachment of droplets from cylinders in flow using an experimental analogue. *Journal of Fluid Mechanics 771*, 327–340.
(Cited on page 28)

Hussain, D. (2009). *Makroskopische Eigenschaften von elektrogesponnenen Nanofaser-Vliesen: Vergleich von theoretischen Vorhersagen und experimentellen Befunden*. Ph. D. thesis, Philipps-Universität Marburg.
(Cited on page 67)

Janakiraman, A., S. Feng, and P. K. Herman (2011). Inertial impactor with enhanced separation. US patent 0023429.
(Cited on page 81)

Joseph, A. F. (1984). Fiber Bed Mist Eliminators: Latest Developments. *Filtration & Separation 21*(1), 40–42.
(Cited on page 28)

Kampa, D. (2015). *Filtration von Ölnebel*. Ph. D. thesis, Karlsruhe Institute for Technology.
(Cited on pages x, 27, 95 and 102)

Kampa, D., J. Meyer, B. J. Mullins, and G. Kasper (2008). Methoden zum schnelleren Erreichen des stationären Zustandes von Ölnebelfiltern. In *Kolloquium Filtertechnik, Karlsruhe*.
(Cited on page 22)

Kampa, D., S. Wurster, J. Buzengeiger, J. Meyer, and G. Kasper (2014). Pressure drop and liquid transport through coalescence filter media used for oil mist filtration. *International Journal of Multiphase Flow 58*, 313–24.
(Cited on pages i, 4, 15, 18, 19, 21, 22, 27, 33, 40, 43, 55, 60, 61, 62, 64, 65, 69, 71, 75, 81, 90, 91, 94, 98, 106, 107 and 146)

Kampa, D., S. Wurster, J. Meyer, and G. Kasper (2015). Validation of a new phenomenological "jump-and-channel" model for the wet pressure drop of oil

mist filters. *Chemical Engineering Science 122*, 150–160.
(Cited on pages 4, 19, 20, 21, 22, 40, 46, 51, 65, 66, 71, 80 and 139)

Kanaoka, C., H. Emi, and T. Myojo (1980). Simulation of the growing process of a particle dendrite and evaluation of a single fiber collection efficiency with dust load. *Journal of Aerosol Science 11*, 377–389.
(Cited on page 70)

Kasper, G., S. Schollmeier, J. Meyer, and J. Hoferer (2009). The collection efficiency of a particle-loaded single filter fiber. *Journal of Aerosol Science 40*, 993–1009.
(Cited on page 70)

Kolb, H. E. and G. Kasper (2019a). Mist filters: How steady is their "steady state"? *Chemical Engineering Science 204*, 118–127.

Kolb, H. E. and G. Kasper (2019b). On the functioning of coalescence filters with a drainage layer – A comment on several papers by Chang et al. *Separation and Purification Technology 225*, 54–59.
(Cited on pages 22, 61 and 63)

Kolb, H. E., J. Meyer, and G. Kasper (2015). Fibrous oil mist filters: Impact of filtration velocity on pressure drop and internal liquid transport. In *Aerosol Technology Conference, Tampere, Finland*.
(Cited on pages 20 and 146)

Kolb, H. E., J. Meyer, and G. Kasper (2017). Flow velocity dependence of the pressure drop of oil mist filters. *Chemical Engineering Science 166*, 107–114.
(Cited on pages 71, 93, 95, 96, 97, 98, 103, 106, 108 and 110)

Kolb, H. E., R. Schmitt, A. Dittler, and G. Kasper (2018). On the Accuracy of Capillary Flow Porometry for Fibrous Filter Media. *Separation and Purification Technology 199*, 198–205.
(Cited on pages 74 and 98)

Kolb, H. E., A. K. Watzek, V. Zaghini Francesconi, J. Meyer, A. Dittler, and G. Kasper (2018). A mesoscale model for the relationship between efficiency and internal liquid distribution of droplet mist filters. *Journal of Aerosol Science 123*, 219–230.
(Cited on page 94)

Krantz, W. B., A. R. Greenberg, E. Kujundzic, A. Yeo, and S. S. Hosseini (2013). Evapoporometry: A novel technique for determining the pore-size distribution of membranes. *Journal of Membrane Science 438*, 153–166.
(Cited on page 14)

Kuwabara, S. (1959). The Forces experienced by Randomly Distributed Parallel Circular Cylinders or Spheres in a Viscous Flow at Small Reynolds Numbers. *Journal of the Physical Society of Japan 14*(4), 527–532.
(Cited on page 16)

Lee, K. W. and B. Y. H. Liu (1982). Theoretical Study of Aerosol Filtration by Fibrous Filters. *Aerosol Science and Technology 1*(2), 147–161.
(Cited on page 24)

Lehmann, M. J., J. Eisengräber-Pabst, J. Ohser, and A. Moghiseh (2013). Characterization of the formation of filter paper using the Bartlett spectrum of the fiber structure. *Image Analysis & Stereology 32*, 77–87.
(Cited on page 145)

Lehmann, M. J., E. H. Hardy, J. Meyer, and G. Kasper (2005). MRI as a key tool for understanding and modeling the filtration kinetics of fibrous media. *Magnetic Resonance Imaging 23*, 341–342.
(Cited on page 121)

Li, D., M. W. Frey, and Y. L. Joo (2006). Characterization of nanofibrous membranes with capillary flow porometry. *Journal of Membrane Science 286*, 104–114.
(Cited on pages 15, 65, 67 and 121)

Liew, T. P. and J. R. Conder (1985). Fine Mist Filtration by Wet Filters – I: Liquid Saturation and Flow Resistance of Fibrous Filters. *Journal of Aerosol Science 16*(6), 497–09.
(Cited on pages 17, 28, 46 and 94)

Liu, Z., Z. Ji, X. Wu, H. Ma, F. Zhao, and Y. Hao (2016). Experimental investigation on liquid distribution of filter cartridge during gas-liquid filtration. *Separation and Purification Technology 170*, 146–154.
(Cited on page 64)

Lockington, D. A. and J.-Y. Parlange (2004). A new equation for macroscopic description of capillary rise in porous media. *Journal of Colloid and Interface Science 278*(2), 404–409.
(Cited on page 12)

Lord Rayleigh, F. R. S. (1880). On the stability, or Instability, of certain Fluid Motions. *Proceedings of the London Mathematical Society 11*, 57–70.
(Cited on page 10)

Lucas, R. (1918). Über das Zeitgesetz des kapillaren Aufstiegs von Flüssigkeiten. *Kolloid-Zeitschrift 23*, 15–22.
(Cited on page 12)

Luckert, K. (2004). *Handbuch der mechanischen Fest-Flüssig-Trennung*. Vulkan-Verlag, Essen.
(Cited on page 11)

Madhugiri, S., B. Sun, P. Smirniotis, J. P. Ferraris, and K. J. Balkus (2004). Electrospun mesoporous titanium dioxide fibers. *Microporous and Mesoporous Materials 69*, 77–83.
(Cited on page 121)

Marmur, A. (2006). Soft contact: measurement and interpretation of contact angles. *Soft Matter 2*(1), 12–17.
(Cited on page 9)

Marmur, A. and R. Cohen (1997). Characterization of porous media by the kinetics of liquid penetration: the vertical capillaries model. *Journal of Colloid and Interface Science 189*, 299–304.
(Cited on page 11)

Martic, G., F. Gentner, D. Seveno, D. Coulon, J. De Coninck, and T. D. Blake (2002). A molecular dynamics simulation of capillary imbibition. *Langmuir 18*(21), 7971–7976.
(Cited on page 13)

May, K. R. (1973). The Collison nebulizer: Description, performance and application. *Journal of Aerosol Science 4*(3), 235–243.
(Cited on pages 41 and 98)

McHale, G., M. I. Newton, and B. J. Carroll (2001). The Shape and Stability of Small Liquid Drops on Fibers. *Oil & Gas Science and Technology 56*(1), 47–54.
(Cited on page 11)

Mead-Hunter, R., R. D. Braddock, D. Kampa, N. Merkel, G. Kasper, and B. J. Mullins (2013). The relationship between pressure drop and liquid saturation in oil-mist filters – predicting filter saturation using a capillary based model. *Separation and Purification Technology 104*, 121–129.
(Cited on pages 4, 20, 22, 46, 48, 51, 54, 95, 96, 108, 109 and 139)

Mead-Hunter, R., A. J. C. King, G. Kasper, and B. J. Mullins (2013). Computational fluid dynamics (CFD) simulation of liquid aerosol coalescing filters.

Journal of Aerosol Science 61, 36–49.
(Cited on page 23)

Mead-Hunter, R., A. J. C. King, and B. J. Mullins (2012). Plateau Rayleigh Instability Simulation. *Langmuir 28*(17), 6731–6735.
(Cited on page 11)

Mead-Hunter, R., A. J. C. King, and B. J. Mullins (2014). Aerosol-mist coalescing filters–a review. *Separation and Purification Technology 133*, 484–506.
(Cited on pages 10, 84, 96 and 145)

Mead-Hunter, R., B. J. Mullins, R. N. Pitta, G. Kasper, and W. Heikamp (2014). Comparative Performance of Philic and Phobic Oil-Mist Filters. *AIChE Journal 60*, 2976–2984.
(Cited on pages 25, 86 and 91)

Molerus, O., M. H. Pahl, and H. C. H. Rumpf (1971). Die Porositätsfunktion in empirischen Gleichungen für den Durchströmungswiderstand im Bereich $Re \leq 1$. *Chemie Ingenieur Technik 43*(6), 376–378.
(Cited on page 56)

Morison, K. R. (2008). A comparison of liquid-liquid porosimetry equations for evaluation of pore size distribution. *Journal of Membrane Science 325*, 301–310.
(Cited on pages 14 and 120)

Müller, T. K., J. Meyer, E. Thébault, and G. Kasper (2014). Impact of an oil coating on particle deposition and dust holding capacity of fibrous filters. *Powder Technology 253*, 247–255.
(Cited on pages 24 and 71)

Mullins, B. J., R. D. Braddock, I. E. Agranovski, and R. A. Cropp (2006). Observation and modelling of barrel droplets on vertical fibres subjected to gravitational and drag forces. *Journal of Colloid and Interface Science 300*, 704–712.
(Cited on pages 26, 27, 71 and 108)

Mullins, B. J., R. D. Braddock, I. E. Agranovski, R. A. Cropp, and R. A. O'Leary (2005). Observation and modelling of clamshell droplets on vertical fibres subjected to gravitational and drag forces. *Journal of Colloid and Interface Science 284*, 245–254.
(Cited on page 71)

Mullins, B. J., R. D. Braddock, and G. Kasper (2007). Capillarity in fibrous filter media: Relationship to filter properties. *Chemical Engineering Science 62*(22), 6191–6198.
(Cited on pages 11, 12 and 14)

Mullins, B. J. and G. Kasper (2006). Comment on: "clogging of fibrous filters by liquid aerosol particles: Experimental and phenomenological modelling study" by Frising et al. *Chemical Engineering Science 61*, 6223–6227.
(Cited on pages 18 and 84)

Patel, S. U., P. S. Kulkarni, S. U. Patel, and G. G. Chase (2012). The effect of surface energy woven drainage channels in coalescing filters. *Separation and Purification Technology 87*, 54–61.
(Cited on page 86)

Payet, S., D. Boulaud, G. Madelaine, and A. Renoux (1992). Penetration and pressure drop of a HEPA filter during loading with submicron liquid particles. *Journal of Aerosol Science 23*, 723–735.
(Cited on pages 26, 27, 71, 84 and 140)

Penner, T., J. Meyer, G. Kasper, and A. Dittler (2019). Impact of operating conditions on the evolution of droplet penetration in oil mist filters. *Separation and Purification Technology 211*, 697–703.
(Cited on page 19)

Pich, J. (1964). Impaction of aerosol particles in the neighbourhood of a circular hole. *Collection of Czechoslovak Chemical Communications 29*, 2223–2227.
(Cited on page 81)

Pich, J. (1966). Pressure drop of fibrous filters at small Knudsen numbers. *Annals of Occupational Hygiene 9*(1), 23–27.
(Cited on page 11)

Plateau, J. (1873). *Statique Expérimentale et Theorique des Liquids soumis aux seules Forces Moléculaires*. Gauthier-Villars, Paris.
(Cited on page 10)

Qin, X. H. and S. Y. Wang (2006). Filtration Properties of Electrospinning Nanofibers. *Applied Polymer Science 102*, 1285–1390.
(Cited on pages 65 and 121)

Quéré, D. (1999). Fluid coating on a fiber. *Annual Review of Fluid Mechanics 31*(1), 347–384.
(Cited on page 26)

Ranz, W. E. and E. J. Katz (1959). Determining Impaction Efficiencies of Mist Collection Equipment. *Journal of the Air Pollution Control Association 8*(4), 328–332.
(Cited on page 28)

Raynor, P. C. and D. Leith (2000). The Influence of Accumulated Liquid on Fibrous Filter Performance. *Journal of Aerosol Science 31*, 19–34.
(Cited on pages 17, 22, 25, 26, 71, 86 and 140)

Reed, C. M. and N. Wilson (1993). The fundamentals of absorbency of fibers, textile structures and polymers. I: The rate of rise of a liquid in glass capillaries. *Journal of Physics D: Applied Physics 26*(9), 1378–1381.
(Cited on page 12)

Rideal, E. K. (1922). CVIII. On the flow of liquids under capillary pressure. *Philosophical Magazine Series 6*(44), 1152–1159.
(Cited on page 13)

Ripperger, S., W. Gösele, C. Alt, and T. Loewe (2012). Ullmanns Encyclopedia of Industrial Chemistry – Filtration Fundamentals.
(Cited on page 11)

Rothman, D. H. (1990). Macroscopic Laws for Immiscible Two-Phase Flow in Porous Media: Results From Numerical Experiments. *Journal of Geophysical Research 95*(B6), 8663–8674.
(Cited on page 23)

Schubert, H. (1982). *Kapillarität in porösen Feststoffsystemen*. Springer, Berlin.
(Cited on pages 18 and 23)

Schweers, E. and F. Löffler (1994). Realistic modelling of the behaviour of fibrous filters through consideration of filter structure. *Powder Technology 80*(3), 191–206.
(Cited on page 24)

Shaw, D. T. (1978). *Fundamentals of aerosol science*. Wiley, New York.
(Cited on page 16)

Siebold, A., M. Nardin, J. Schultz, A. Walliser, and M. Oppliger (2000). Effect of dynamic contact angle on capillary rise phenomena. *Colloids and Surfaces A: Physicochemical and Engineering Aspects 161*(1), 81–87.
(Cited on page 13)

Sobolev, V. D., N. V. Churaev, M. G. Velarde, and Z. M. Zorin (2000). Surface Tension and Dynamic Contact Angle of Water in Thin Quartz Capillaries.

Journal of Colloid and Interface Science 222(1), 51–54.
(Cited on page 13)

Souders, M. and G. G. Brown (1934). Design of Fractionating Columns I. Entrainment and Capacity. *Industrial & Engineering Chemistry 26*(1), 98–103.
(Cited on page 28)

Spielman, L. and S. L. Goren (1968). Model for Predicting Pressure Drop and Filtration Efficiency in Fibrous Media. *Environmental Science & Technology 2*(4), 279–287.
(Cited on page 16)

Stechkina, I. B. and N. A. Fuchs (1966). Studies on fibrous aerosol filters–I. Calculation of diffusional deposition of aerosols in fibrous filters. *Annals of Occupational Hygiene 9*, 59–64.
(Cited on page 24)

Stieß, M. (2008). *Mechanische Verfahrenstechnik - Partikeltechnologie 1*. Springer.
(Cited on page 11)

Suneja, S. K. and C. H. Lee (1974). Aerosol filtration by fibrous filters at intermediate reynolds numbers (≤ 100). *Atmospheric Environment 8*(11), 1081–1094.
(Cited on page 24)

Venugopal, G., J. Moore, J. Howard, and S. Pendalwar (1999). Characterization of microporous separators for lithium-ion batteries. *Journal of Power Sources 77*(1), 34–41.
(Cited on page 15)

Walsh, D., J. I. T. Stenhouse, K. L. Scurrah, and A. Graef (1996). The effect of solid and liquid aerosol particle loading on fibrous filter material performance. *Journal of Aerosol Science 27*, 617–618.
(Cited on page 19)

Wang, H.-C. and G. Kasper (1990). Note on inertial deposition of particles on an orifice disc. *Journal of Aerosol Science 21*, 213–216.
(Cited on page 81)

Washburn, E. W. (1921). The dynamics of capillary flow. *Physical Review 17*(3), 273–283.
(Cited on page 12)

Wenzel, R. N. (1937). Resistance of solid surfaces to wetting by water. *Industrial and Engineering Chemistry 28*, 988–994.
(Cited on page 9)

Wurster, S. (2017). *Entrainment von Öltropfen an der Rückwand eines Faserfilters*. Ph. D. thesis, Karlsruhe Institute for Technology.
(Cited on page 28)

Wurster, S., D. Kampa, J. Meyer, T. Müller, B. J. Mullins, and G. Kasper (2015). Measurement of oil entrainment rates and drop size spectra from coalescence filter media. *Chemical Engineering Science 132*, 72–80.
(Cited on pages 4, 28, 41, 88 and 96)

Wurster, S., J. Meyer, and G. Kasper (2017). On the relationship of drop entrainment with bubble formation rates in oil mist filters. *Separation and Purification Technology 179*, 542–549.
(Cited on pages 28, 64, 131 and 147)

Wurster, S., J. Meyer, H. E. Kolb, and G. Kasper (2015). Bubbling vs. blow-off – On the relevant mechanism(s) of drop entrainment from oil mist filter media. *Separation and Purification Technology 152*, 70–79.
(Cited on pages 28 and 88)

Young, T. (1805). An Essay on the Cohesion of Fluids. *Philosophical Transactions of the Royal Society of London 95*, 65–87.
(Cited on page 9)

Yu, J., X. Hu, and Y. Huang (2010). A modification of the bubble-point method to determine the pore-mouth size distribution of porous materials. *Separation and Purification Technology 70*, 314–319.
(Cited on pages 15 and 120)

Yunoki, T., K. Matsumoto, and K. Nakamura (2004). Pore size distribution measurements of nonwoven fibrous filter by differential flow method. *Membrane 29*, 227–235.
(Cited on pages 16, 37, 121, 129 and 130)